

Evaluation of the $^4I_{11/2}$ Terminal Level Lifetime for Several Neodymium-Doped Laser Crystals and Glasses

Camille Bibeau
(Ph.D. Dissertation)

April 25, 1995

LAWRENCE LIVERMORE NATIONAL LABORATORY
University of California • Livermore, California • 94551



DISTRIBUTION OF THIS DOCUMENT IS UNLIMITED

WB

MASTER

DISCLAIMER

This report was prepared as an account of work sponsored by an agency of the United States Government. Neither the United States Government nor any agency thereof, nor any of their employees, make any warranty, express or implied, or assumes any legal liability or responsibility for the accuracy, completeness, or usefulness of any information, apparatus, product, or process disclosed, or represents that its use would not infringe privately owned rights. Reference herein to any specific commercial product, process, or service by trade name, trademark, manufacturer, or otherwise does not necessarily constitute or imply its endorsement, recommendation, or favoring by the United States Government or any agency thereof. The views and opinions of authors expressed herein do not necessarily state or reflect those of the United States Government or any agency thereof.

DISCLAIMER

Portions of this document may be illegible in electronic image products. Images are produced from the best available original document.

Evaluation of the ${}^4I_{11/2}$ Terminal Level Lifetime for
Several Neodymium-Doped Laser Crystals and Glasses

BY

Camille Bibeau
B.S. (University of Oregon, Eugene) 1986

DISSERTATION

Submitted in partial satisfaction of the requirements for the degree of

DOCTOR OF PHILOSOPHY

in

Applied Science

in the

GRADUATE DIVISION

of the

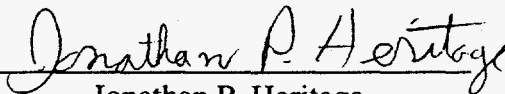
UNIVERSITY OF CALIFORNIA

DAVIS

Approved:



Ann E. Orel



Jonathan P. Heritage



Stephen A. Payne

Committee in Charge

1995

Acknowledgments

My work on this dissertation has involved the valued support and encouragement from colleagues, friends, and family.

Among my colleagues, I would first like to thank John Hunt for initially encouraging me to join the B.S./M.S. Program within the Laser Directorate at Lawrence Livermore National Laboratory. This unique program, which combined programmatic research with thesis research, has had the support of many people within the Laser Directorate including Mike Campbell and Howard Powell, both of whom I wish to thank for their continued support throughout my thesis research. I would also like to thank Bill Krupke for his encouragement and interest in my thesis research.

Instrumental to the timely completion of my thesis research was Stephen Payne, my research advisor. His ability to always see the big picture along with his honesty and energetic drive were all contributing factors to my growth as a scientist. His positive influence in my research will be an integral part of my future career as a physicist. I wish to thank Ann Orel, the chairperson of my thesis committee, for offering valuable advise during the course of my graduate studies. She acted not only as a mentor but also became an influential and positive a role model during my graduate research. I also wish to thank Jonathan Heritage, a member of the committee, for offering valuable suggestions on and for approving my dissertation.

Along the way there were valued conversations and advise from my coworkers: John Trenholme, Ken Jancaitis, Dave Milam, John Caird, Ray Beach, Steve Velsko, Chris Ebbers, and Mark Hermann. All of whom had a friendly open door policy for questions and words of wisdom.

I would also like to thank many of the members of the Advance Solid State Laser Group including Joel Speth, Gary Wilke, Chris Marshall, Laura DeLoach, Kathleen Schaffers, John Tassano, and Larry Smith. In particular, I wish to thank Joel for his help with maintaining the laser systems, Gary for his assistance with the spectroscopy, and Chris for his advise on experimental techniques. I would also like to thank Ron Vallene and Peter Thelin for carefully preparing the glasses and crystals in a timely manner.

Of the friends who influenced me before entering graduate school, I would like to thank Jim Isenberg, Kwangjai Park, and David Sokolof from the University of Oregon for initially encouraging me to pursue a degree in physics. Their overall support lead the way to my continued studies throughout graduate school.

Closer to home, I would like to thank two very special friends, Janice Lawson and Michael Lambert. Janice, having finished her thesis research before me, never hesitated to offer me her insights, understanding, and loyal support. I wish to especially thank Michael for his thoughtfulness, love, and ability to listen and listen and... Together, their strong support and friendship helped make the periodic disappointments seem a small but normal part of the journey.

And finally, I would like to thank my parents and the other family members who conveyed to me the importance of continuing my education. In particular, I wish to thank my grandmother, Mary Bibeau, who has always encouraged me to pursue my goals while providing me with an immeasurable amount of love and pride for all of my achievements along the way.

Table of Contents

Chapter	Page Number
Abstract	1
Chapter 1	
Introduction and scope of research	3
Chapter 2	18
Measurements of the terminal level lifetime ($\tau_{11/2}$) for the ${}^4I_{11/2} \rightarrow {}^4I_{9/2}$ transition in 16 Nd-doped crystals and glasses using a novel pump and probe technique	
2.1 Introduction	
2.2 Experimental arrangement	
2.3 Data analysis	
2.4 Results and fit to kinetic model	
2.5 Evaluation of the lower limit to the ${}^4I_{11/2}$ lifetime	
2.6 Conclusion	
Chapter 3	45
Measurements of the nonradiative lifetime ($\tau_{7/2}$) for the ${}^4G_{7/2} \rightarrow {}^4G_{5/2}, {}^2G_{7/2}$ transition in 30 Nd-doped crystals and glasses	
3.1 Introduction	
3.2 Time-correlated single photon counting experimental arrangement	
3.3 Data analysis and results	
3.4 Time resolved emission measurements (fluoride materials)	
3.5 Data analysis and results	
3.6 Comparison of the pump-probe and emission methods and best assessment of the terminal level lifetime for 15 Nd-doped crystals and glasses	
3.7 Conclusion	

Chapter 4	77
Measurements of the nonradiative lifetime ($\tau_{5/2}$) for the ${}^4G_{5/2}, {}^2G_{7/2} \rightarrow {}^2H_{11/2}$ transition in 10 Nd-doped fluoride materials	
4.1 Introduction	
4.2 Experimental arrangement	
4.3 Results and summary	
Chapter 5	89
Comparison of the energy gap theory and energy transfer model for predicting nonradiative transition rates	
5.1 Introduction	
5.2 Derivation of energy gap law by perturbation theory	
5.3 Derivation of energy transfer model	
5.4 Applicability of energy transfer model for predicting nonradiative transition rates and conclusions	
Chapter 6	113
Pulse length and terminal level lifetime dependence of energy extraction for a Nd-doped phosphate amplifier glass	
6.1 Introduction and motivation	
6.2 Numerical model	
6.3 Numerical computation	
6.4 Formulation of empirical model	
6.5 Applicability of model to variations in the input parameters	
6.6 Determination of $\tau_{11/2}$ from numerical modeling of gain saturation data	
6.7 Comparison of $\tau_{11/2}$ values obtained from time resolved experiments	
6.8 Conclusion	
Summary	135

Abstract

All models of lasing action require knowledge of the physical parameters involved, of which many can be measured or estimated. The value of the terminal level lifetime is an important parameter in modeling many high power laser systems since the terminal level lifetime can have a substantial impact on the extraction efficiency of the system. However, the values of the terminal level lifetimes for a number of important laser materials such as Nd:YAG and Nd:YLF are not well known. The terminal level lifetime, a measure of the time it takes for the population to drain out of the terminal (lower) lasing level, has values that can range from picoseconds to microseconds depending on the host medium, thus making it difficult to construct one definitive experiment for all materials. Until recently, many of the direct measurements of the terminal level lifetime employed complex energy extraction or gain recovery methods coupled with a numerical model which often resulted in large uncertainties in the measured lifetimes.

In this report we demonstrate a novel and more accurate approach which employs a pump-probe technique to measure the terminal level lifetime of 16 neodymium-doped materials. An alternative yet indirect method, which is based on the "Energy Gap Law," is to measure the nonradiative lifetime of another transition which has the same energy gap as the transition of the terminal level lifetime. Employing this simpler approach, we measured the lifetime for 30 neodymium-doped materials. We show for the first time a direct comparison between the two methods and determine that the indirect method can be used to infer the terminal level lifetime within a factor of two for most neodymium-doped glasses and crystals.

In addition, we evaluate the validity of the energy gap law for nonradiative transitions which occur over very small energy gaps ($\leq 1000 \text{ cm}^{-1}$). We show that several measured nonradiative rates still follow an exponential dependence on the energy gap in accordance with the energy gap law. We also discuss an alternative approach for predicting the nonradiative rates by observing that the absorption coefficient has a similar exponential dependence on the energy gap and that the two quantities can be related.

Given the importance of the terminal level lifetime, it would be useful if an approximate solution of the energy transport and kinetic differential equations existed which explicitly included the terminal level lifetime and the extraction pulse length. The exact solutions which currently exist are only for the two extreme cases of either infinitely long or short pulse lengths compared to the terminal level lifetime. We have formulated an empirical solution of the saturation fluence which explicitly includes the ratio of the pulse width to the terminal level lifetime and can be substituted within the well known Frantz-Nodvik analytic solution to model the energy extracted from a phosphate amplifier. For a third, independent evaluation of the terminal level lifetime for the phosphate glass, LG-750, we used our modified expression for the saturation fluence to model data taken from a previous set of energy extraction experiments. We found that terminal level lifetime derived from the best fit to the data is in agreement with the values derived from the pump-probe and emission experiments described above, thus giving confidence to the measured terminal level lifetime of LG-750.

In summary, we have shown that the experimental, theoretical, and computational studies described in this report can be used individually or in combination with each other to determine the terminal level lifetime for existing or prospective laser glasses and crystals.

Chapter 1

Introduction and scope of research

The performance of a neodymium solid state laser is determined in part by the kinetics of energy flow among the energy levels of the neodymium dopant ion in the crystalline or glassy host and in the pumping and extraction processes. In the case of most Nd^{3+} laser media, the pumping method involves the use of either laser diodes or flash lamps, and the pump energy is found to accumulate in the ${}^4\text{F}_{3/2}$ metastable or upper laser level (**Figure 1.1a**). The neodymium ion can then be made to lase at the 0.9, 1.06, or 1.3 μm wavelengths, depending on the identity of the terminal laser level (the ${}^4\text{I}_{9/2}$, ${}^4\text{I}_{11/2}$, or ${}^4\text{I}_{13/2}$ state respectively); laser action in most Nd-lasers involves the 1.06 μm (${}^4\text{F}_{3/2} \rightarrow {}^4\text{I}_{11/2}$) transition. Since the ${}^4\text{I}_{11/2}$ terminal laser level is about 2000 cm^{-1} above the ${}^4\text{I}_{9/2}$ ground state, the last event in this sequence of steps is the ${}^4\text{I}_{11/2} \rightarrow {}^4\text{I}_{9/2}$ nonradiative relaxation process. In this system, the terminal level lifetime ($\tau_{11/2}$) is the decay time for the neodymium ions in the ${}^4\text{I}_{11/2}$ level to drain into the ${}^4\text{I}_{9/2}$ ground state.

The value of the terminal level lifetime can be an important parameter in determining the design and performance specifications of high power laser systems. Its magnitude relative to the laser pulse width, will determine whether a system operates as a four- or three-level laser. In most cases, four-level operation is desired since extraction is improved. The lasing scheme shown in **Figure 1.1a** is an example of a four level laser when the terminal level lifetime is infinitely fast compared to the length of the pulse, $\tau_{11/2} \ll t_p$. In this case, the ${}^4\text{I}_{11/2}$ level will appear to be virtually unpopulated for the duration of the extraction pulse. Since the small signal gain coefficient is directly proportional to the population inversion between the upper ${}^4\text{F}_{3/2}$ level and the lower ${}^4\text{I}_{11/2}$ level, the incoming laser pulse will extract more of the stored energy if the ${}^4\text{I}_{11/2}$ level remains unpopulated. On the other hand, if the length of the extracting pulse is much less than the terminal level lifetime, $\tau_{11/2} \gg t_p$, then the population in the ${}^4\text{I}_{11/2}$ level will become bottlenecked and the attainable extraction efficiency will be diminished since the upward and downward transitions at the laser frequency will eventually become equal, thereby imposing a fundamental limit on the fraction of extractable energy.

An example of *purely* three-level laser occurs in systems where the laser transition terminates on the ground state. An example of this is found in the ruby laser (Cr-doped sapphire) where the main laser transition at the 0.694 μm wavelength transfers a fraction of the Cr ion population between the E level and the ${}^4\text{A}_2$ ground state level (**Figure 1.1b**). In this case, the value of terminal level lifetime can be considered to be infinitely long and thus limits the maximum attainable extractable energy.

For neodymium laser systems, the fraction of extractable energy may be expressed in the high temperature limit as:

$$\eta_{\text{extr}} = \frac{1}{\left[1 + \frac{d_u}{d_l}\right]} \quad (1)$$

where d_u/d_l is the ratio of the degeneracies for the upper ${}^4\text{F}_{3/2}$ and lower ${}^4\text{I}_{11/2}$ neodymium levels. For finite temperatures, the ratio of degeneracies, d_u/d_l , can be replaced by the ratio of Boltzmann occupation fractions, f_l/f_u , of the crystal field levels within the ${}^4\text{I}_{11/2}$ and ${}^4\text{F}_{3/2}$ manifolds. If the ${}^4\text{I}_{11/2}$ level is fully bottlenecked, the internal extraction efficiency, η_{extr} , for a Nd laser is at its minimum and is equal to 75%. If one considers the additional impact of a square output pulse of duration, t_p , together with the terminal level lifetime, $\tau_{11/2}$, the limiting extraction efficiency is found to be:

$$\eta_{\text{extr}}(t_p, \tau_{11/2}) = \frac{1}{\left[1 + \frac{d_u}{d_l} \times \Omega\right]} \quad (2)$$

where Ω represents the bottlenecking efficiency which ranges from zero to one depending on the ratio of $t_p/\tau_{11/2}$ (derived in Chapter 6). In **Figure 1.2**, the ideal extraction efficiency is plotted as a function of $R = t_p/\tau_{11/2}$ for the Nd-doped phosphate glass LG-750. This glass is used in the amplifier section of the Nova Laser and is similar to the glass used in the design of the National Ignition Facility (NIF)¹. For comparison, a few additional data are shown including the oxide crystals, Nd:YAG and Nd:YALO, and the fluoride crystal, Nd:YLF (The data points for these materials will not lie exactly on the phosphate curve due to differences in the degeneracies of the upper and lower laser levels and thus the values for the extraction efficiency). The pulse lengths (t_p) were assumed to be square in

shape with a length of 3 ns with the exception of the NIF data point where a pulse length of 8 ns was used. Using this extraction model, we are able to show that the extraction efficiencies for a Nd:phosphate glass laser are only moderately impacted by the short terminal level lifetime (<1 ns) whereas for Nd:YLF, the long terminal level lifetime (~10 ns) can become a limiting factor.

The progress of solid-state laser science during the last decade is such that, it is now possible to model and predict the pumping and extraction dynamics in numerous kinds of systems as discussed above. For more accurate modeling and prediction, additional detailed information concerning the laser physics of the gain medium is required to completely account for the various mechanisms impacting the efficiencies, pulse distortion, and other effects. The terminal level lifetime can be included as an important parameter for many kinetic, energy transport and extraction efficiency models as illustrated in **Figure 1.2**. As a result, there have been several experimental and theoretical approaches over the last three decades to accurately measure the terminal level lifetime. However, agreement in the results among the different approaches for a large sampling of laser materials has never been demonstrated due to the experimental complexities involved in making a precise measurement of the short lifetimes (< 1ns) found in many laser materials.

To illustrate the differences found in the experimental values for the terminal level lifetime, we list several results for Nd:YAG in **Table 1.1** where we find values ranging from 0.370 to 500 ns^{2,3,4,5,6,7,8,9,10}. Of the measurements listed, the shortest value of 370 ps was obtained by Basiev and coworkers² in an experiment in which they measured the nonradiative lifetime of the ${}^4G_{7/2}$ level through time resolved luminescence decay. Since in Nd:YAG, the ${}^4G_{7/2} \rightarrow {}^4G_{5/2}, {}^2G_{7/2}$ and ${}^4I_{11/2} \rightarrow {}^4I_{9/2}$ transitions both have similar sized energy gaps of 1150 cm^{-1} , the measured nonradiative lifetime for ${}^4G_{7/2} \rightarrow {}^4G_{5/2}, {}^2G_{7/2}$ transition should in principle (according to the energy gap law which we will discuss later) be equal to the $\tau_{11/2}$ lifetime. Another experimental approach listed was to measure the temporal gain recovery of the ${}^4F_{3/2} \rightarrow {}^4I_{11/2}$ laser transition by using a weak pulse to probe the remaining small-signal gain within a test amplifier after the passage of a saturating pulse. The results obtained from these measurements have resulted in lifetimes

ranging from 5 to 300 ns. It is evident from the wide range of values listed in **Table 1.1** that there is a lack of agreement among the various measurements suggesting the need for a new approach.

Therefore, one of the goals of this project was to develop a direct and more accurate approach for measuring the terminal level lifetime of several Nd-doped glasses and crystals. In the past, many direct measurements usually employed either an energy extraction⁶ or gain recovery¹¹ method coupled with a numerical model of the population dynamics. For example, in **Figure 1.3a** we show an energy level diagram for an energy extraction experiment where population is transferred from the ${}^4F_{3/2}$ level to the ${}^4I_{11/2}$ level in a Nd-doped host via stimulated emission. The amount of energy extracted from the gain medium is evaluated from measurements of the laser pulse energy before and after passage through the material. The terminal level lifetime is included as a fitting parameter in the numerical model and found by the best fit to the data. Our approach differed from experiments such as these in that we were able to more directly populate the terminal level utilizing a unique pump and probe technique¹². In the experiment, a 2.41 μm pump beam excites a fraction of the ground state population into the ${}^4I_{13/2}$ (**Figure 1.3b**). A probe beam monitors the draining of the ${}^4I_{11/2}$ population into the ${}^4I_{9/2}$ ground state by exciting a fraction of the ${}^4I_{11/2}$ population into the upper ${}^4F_{3/2}$ level. Here the radiative emission for the ${}^4F_{3/2} \rightarrow {}^4I_{9/2}$ transition is *time integrated*. The value of the time integrated emission signal is proportional to the population in the ${}^4I_{11/2}$ level at each instant in time. In order to record the complete temporal profile of the ${}^4I_{11/2}$ population, this process is repeated for increased time delays of the probe beam with respect to the pump beam. We discuss this experimental scheme in detail in Chapter 2 and present the analysis and results for 16 Nd-doped laser materials.

Although we found that the above experiment is an ideal technique suitable for directly measuring the terminal level lifetime, the experimental setup and analysis can be complex. And therefore, it would be useful to find a simpler method which could be used to infer the value of the terminal level lifetime based on a comparisons with the lifetime derived from the more accurate pump-probe experiment. Upon surveying the experimental techniques discussed in the literature, we found that an indirect method

which is based on the validity of the energy gap law^{13,14} is the most widely used because of its simple and straightforward approach. The energy gap law postulates that the nonradiative lifetime between two electronic levels within a given material primarily depends upon the host phonon spectrum and the size of the energy gap between the two levels; the symmetries of the electronic levels are not considered relevant. Coincidentally, there exists a higher lying nonradiative transition (${}^4G_{7/2} \rightarrow {}^4G_{5/2}, {}^2G_{7/2}$) in neodymium whose energy gap nearly matches that of the lower, ${}^4I_{11/2} - {}^4I_{9/2}$ gap (**Figure 1.3c**). Based on the validity of the energy gap theory, the two lifetimes, $\tau_{7/2}$ and $\tau_{11/2}$ (corresponding to the ${}^4G_{7/2} \rightarrow {}^4G_{5/2}, {}^2G_{7/2}$ and ${}^4I_{11/2} \rightarrow {}^4I_{9/2}$ transitions respectively) are inferred to be equal. Time resolved emission intensity from the ${}^4G_{7/2}$ level at ~ 600 nm will produce a signal which is dominated by the nonradiative rate. Therefore, the fluorescence signal is a direct measure of the ${}^4G_{7/2} \rightarrow {}^4G_{5/2}, {}^2G_{7/2}$ nonradiative decay and an indirect measure of the ${}^4I_{11/2} \rightarrow {}^4I_{9/2}$ transition. This method typically requires a high temporal resolution detector and/or a time-correlated single photon counting system since some materials such as YAG (see **Table 1.1**) have very short nonradiative lifetimes. In Chapter 3, we describe the measurements of the $\tau_{7/2}$ lifetime in 30 Nd-doped materials including those investigated in the pump-probe experiments. We also show that the inferred terminal level lifetimes ($\tau_{7/2}$) from the indirect method are within a factor of two of the pump-probe terminal level lifetimes ($\tau_{11/2}$) for most of Nd-doped glasses and crystals investigated thus offering validation for the simpler, indirect approach.

In Chapter 4 we measure the $\tau_{5/2}$ lifetime for the ${}^4G_{5/2}, {}^2G_{7/2} \rightarrow {}^2H_{11/2}$ transition in 10 Nd-doped fluoride glasses and crystals. The nonradiative rates for this particular transition have not been measured in many materials due to the small energy gaps (< 1000 cm^{-1}) and fast rates expected (nanoseconds). The experiments in this chapter help to provide additional data to what is currently available in the literature and explore the validity of the energy gap law for nonradiative transitions which occur over very small energy gaps (i.e. less than that of the ${}^4I_{11/2} - {}^4I_{9/2}$ separation).

We also recognize that in addition to needing to know the measured $\tau_{11/2}$ values for existing common laser materials, it would also be useful to have a theoretical means

of reliably predicting the values for new prospective crystals and glasses. Several theoretical approaches have been taken to formulate an expression for the nonradiative rate between two levels of a rare-earth ion in terms of measurable or calculable quantities. Some of the early theoretical formulations were constructed by Perlin¹⁵, Huang¹⁶, Kiel¹⁷, Orbach¹⁸, Partlow and Moos¹⁹, Miyakawa and Dexter²⁰, Fischer²¹, Soules and Duke²², Fong et al.²³, and Struck and Fonger²⁴. Some of these attempts relied upon knowing complex matrix elements, ion-phonon coupling coefficients, phonon densities, and other quantities that were difficult to calculate, measure, or even estimate. Included among the first theoretical efforts to render these equations in a convenient form were ideas expressed by Riseberg and Moos¹³ for rare-earth doped crystalline hosts, and Layne, Lowdermilk, and Weber¹⁴ for rare-earth doped glasses. Their final expression (rederived in Chapter 5) for the nonradiative rate (W_{nr}) involved several measurable quantities: the energy gap between the two levels of interest (ΔE_{gap}), the effective phonon frequency (ν_{eff}), and the temperature. Their expression suggests that for a given temperature, a simple exponential relationship exists between the nonradiative rate and energy gap:

$$W_{nr} = A \exp(-\kappa p) \quad \text{“Energy Gap Law”} \quad (3)$$

where A and κ are host-dependent parameters, and p is the normalized energy gap, ($\Delta E_{gap}/h\nu_{eff}$). The quantity p is the order of the phonon process and arises from considering the single phonon term in the interaction Hamiltonian expansion taken in the p -th order perturbation calculation. The assumption here is that for transitions involving approximately two or more phonons, only the highest frequency of vibration, (ν_{eff}), in the host plays a significant role in enabling the nonradiative transition. Therefore, the smallest number of high frequency phonons will tend to dominate the nonradiative decay rate (**Figure 1.4**). The vibrational frequencies of each host can be independently estimated through measurements of Raman or infrared spectra.

In general, the above expression, known as the energy gap law, has adequately modeled most of the available experimental data corresponding to higher order (>2) phonon processes and larger ($>2000 \text{ cm}^{-1}$) energy gaps. Some theoretical formulations, such as those by Perlin et al.²⁵, Huang and Gu²⁶ include the entire phonon density in their

calculations and do not assume that only the highest frequency phonons are dominant in the transition. A different approach by Gapontsev and Sirtlanov²⁷ has been to incorporate an electric dipole-dipole model that includes the host absorption and rare-earth ion emission in their theoretical nonradiative rate calculations. These latter approaches may be required since for transitions involving 1-2 phonon relaxation processes, we may expect the single-frequency theory to begin to break down since the requisite statistical averaging over matrix elements and other quantities is reduced.

In Chapter 5, we explore the validity of the energy gap law for transitions which have energy gaps that are smaller than 1000 cm^{-1} and involve lower order (1-2 phonon) processes. We found that the measured nonradiative rates still appear to follow an exponential dependence on the energy gap of the transition. This implies that if the transition rates for the larger energy gaps are known, then the values of the faster rates (with smaller energy gaps) can be extrapolated from the W_{nr} versus ΔE_{gap} curve. However, in order to extrapolate to the faster rates, an adequate number of experimental data must be taken in order to accurately establish the slope of the W_{nr} versus ΔE_{gap} curve. We propose an alternative theoretical approach to the gap law by showing that a simple relationship exists between the nonradiative rate and the absorption coefficient for three crystalline materials. This approach employs many of the same ideas used in energy transfer theory to describe the nonradiative transfer of energy between donor and acceptor ions in a host medium. Using this approach, only a measurement of the absorption coefficient and two predetermined scaling factors are needed to determine the nonradiative lifetime for the Nd-doped laser materials investigated.

In the final chapter, we conclude our studies by developing an approximate solution of the energy transport and kinetic differential equations which explicitly includes the terminal level lifetime and the pulse length. Such a solution, is useful for predicting the impact of the terminal level lifetime on energy extraction (recall **Figure 1.2**). To date, the only exact analytic solutions which exist are for the two extreme cases of $t_p/\tau_{11/2} \ll 1$ and $t_p/\tau_{11/2} \gg 1$, that is, very short or long pulse lengths relative to the terminal level lifetime²⁸. We have formulated an empirical solution of the saturation fluence which explicitly includes the ratio, $t_p/\tau_{11/2}$ and is therefore valid in the

intermediate region of $t_p/\tau_{11/2} \approx 1$ as well. Our empirical solution of the saturation fluence can be substituted within the well known Frantz-Nodvik²⁸ analytic solution to model the energy extracted from an amplifier. The motivation for finding an empirical solution was two fold. First, we wanted a simple expression that could be used within the existing models that would include the effects of the terminal level lifetime without having to tediously integrate the energy transport and kinetic differential equations and second, we wanted to verify by a third independent method, that our measured value of the terminal level lifetime for the Nd:phosphate glass, LG-750, is accurate. Therefore, in Chapter 6, we present a modified expression for the saturation fluence and use it to model energy extraction data taken from a previous set of experiments and show that the terminal level lifetime derived from the best fit to the data is in agreement with the lifetimes measured from the direct and indirect methods described in Chapters 2 and 3 respectively.

Table 1.1 A partial list of methods and corresponding terminal level lifetimes reported for Nd:YAG. The results from the various measurement techniques, which include and indirect method (${}^4G_{7/2}$ lifetime) and direct method (gain recovery), illustrate the wide range of reported values and uncertainties.

Nd:YAG	Lifetime (ns)	Method
Basiev ²	0.37	Gap-law (${}^4G_{7/2}$ lifetime)
Cruz ³	0.47	
Kushida ⁴	<10	
Zverev ⁵	~500	
Palombo ⁶	<5	Gain recovery
Hovis ⁷	<11	
Zlenko ⁸	<300	
Zlenko ⁸	<30	Other
Grigoryants ⁹	<10	
Gapontsev ¹⁰	~10	

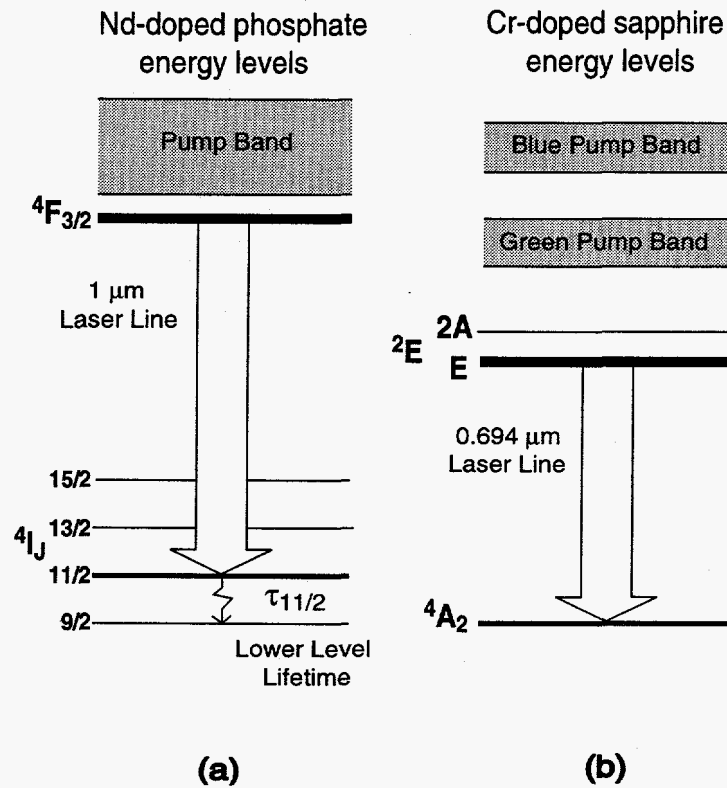


Figure 1.1 Energy level diagrams showing (a) the 1 μ m transition in Nd-doped phosphate glass and (b) the 0.694 μ m transition in Cr-doped sapphire or ruby. In (a) the terminal level lifetime is defined as the time for the Nd population to decay from the $4I_{11/2}$ state to the $4I_{9/2}$ ground state.

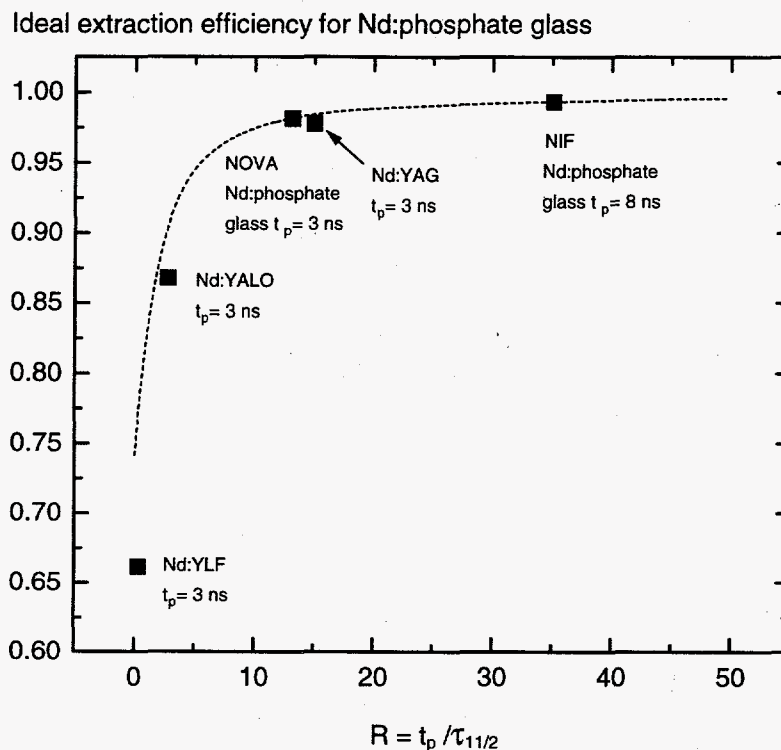


Figure 1.2 The ideal extraction efficiency (dashed line) plotted as a function of the ratio of the pulse length to the terminal level lifetime for a Nd:phosphate glass. For comparison, additional data are shown (Nd:YLF, Nd:YALO, and Nd:YAG). The plots illustrates that the relatively short terminal level lifetime (< 1 ns) of the phosphate glass used in the Nova Laser and of the glass used in the design of the National Ignition Facility (NIF) is not a limiting factor in obtaining the highest possible extraction efficiency. In comparison the long lifetime (~ 10 ns) of the fluoride crystal, Nd:YLF, can actually be a limiting factor.

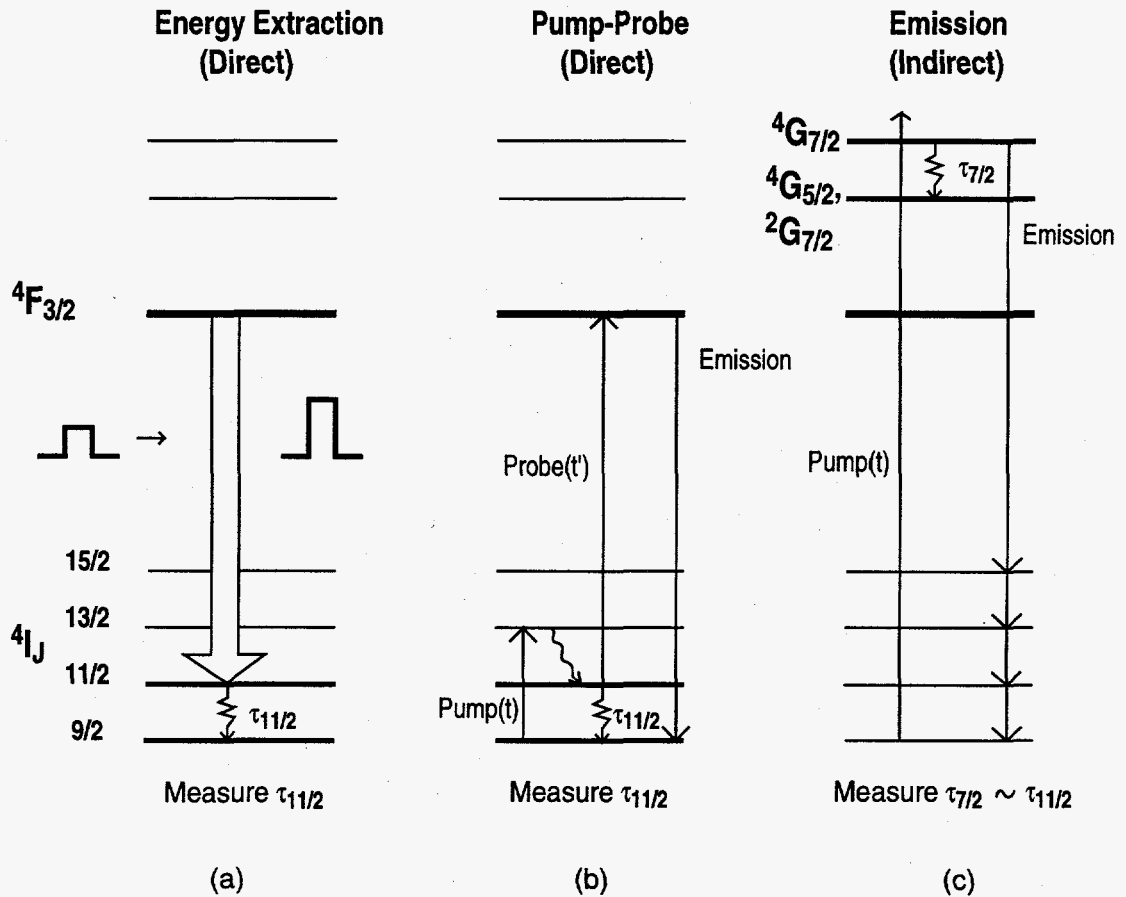
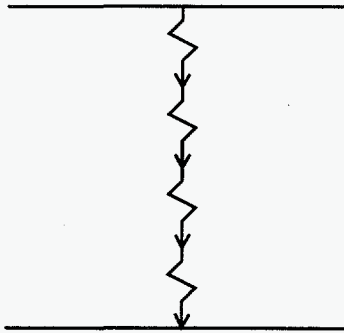
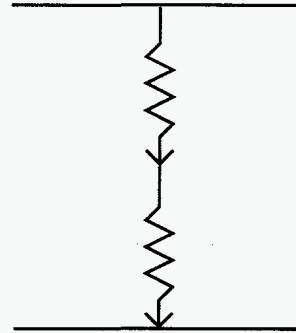


Figure 1.3 Energy level diagrams showing three different methods to measure the terminal level lifetime, $\tau_{11/2}$, in a Nd-doped material. In (a) an extracting pulse is passed through an amplifier medium. The output fluence of the extraction pulse is dependent on the terminal level lifetime and therefore, through numerical modeling of the extracted energy, $\tau_{11/2}$ can be determined. **Fig. (b)** illustrates a more direct method which employs a pump-probe technique. A pump beam followed in time by a probe beam monitors the Nd population in the ${}^4I_{11/2}$ level. The integrated emission signal from the ${}^4F_{3/2}$ level will be proportional to the ${}^4I_{11/2}$ population. The pump-probe process is repeated and eventually the $\tau_{11/2}$ lifetime is constructed. **Fig. (c)** illustrates the least direct but simplest method for determining $\tau_{11/2}$. The nonradiative lifetime for the ${}^4G_{7/2} \rightarrow {}^4G_{5/2}, {}^2G_{7/2}$ transition is determined from the ${}^4G_{7/2}$ emission signal. Since the ${}^4G_{7/2} - {}^4G_{5/2}, {}^2G_{7/2}$ and the ${}^4I_{11/2} - {}^4I_{9/2}$ gaps are nearly the same, the energy gap law implies that $\tau_{7/2} \cong \tau_{11/2}$.

4-phonon process**2-phonon process**

$$W_{nr} (p=4) < W_{nr} (p=2)$$

$$W_{nr} = A \exp(-\kappa p)$$

Figure 1.4 Lower order phonon processes ($p=2$) will lead to faster nonradiative rates (W_{nr}) since a smaller number of phonons are needed to conserve energy and bridge the energy gap.

Chapter 1 References

- ¹Lawrence Livermore National Laboratory ICF Quarterly Report Vol. 5, No. 1, UCRL-LR-105821-95-1, Oct.-Dec. 1994.
- ²T. T. Basiev, A. Y. Dergachev, Y. V. Orlovskii, and A. M. Prokhorov, "Multiphonon nonradiative relaxation from high-lying levels of Nd³⁺ ions in fluoride and oxide laser materials," OSA Proceedings on Advanced Solid-State Lasers **10**, 358 (1991).
- ³J. Cruz, G. Giuliani, and H. M. van Driel, "Measurement of the subnanosecond, nonradiative relaxation time from excited states of Nd³⁺ in a Nd:YAG crystal," Opt. Lett. **15**, 282 (1990).
- ⁴T. Kushida, S. Kinoshita, T. Ohtsuki, and T. Yamada, "Multiphonon relaxation rate from pumped level to upper laser level in YAG:Nd," Solid State Comm. **44**, 1363 (1982).
- ⁵G. M. Zverev, G. Ya. Kolodnyi, and A. M. Onishchenko, "Nonradiative transitions between levels of trivalent rare-earth ions in yttrium-aluminum garnet crystals," Sov. Phys. - JETP **33**, 497 (1971).
- ⁶K. Palombo, S. Matthews, S. Sheldrake, and D. Capps, "Determination of the effective lower level lifetime for Nd:YLF and Nd:YAG through experimental measurement and computer modeling," OSA Proceedings on Advanced Solid-State Lasers **15**, 78 (1993).
- ⁷F. E. Hovis, M. Stuff, C. J. Kennedy, and B. Vivian, "Lower level relaxation of Nd:YAG," IEEE J. Quantum Electron. **28**, 39 (1992).
- ⁸A. A. Zlenko, V. A. Sychugov, and G. P. Shipulo, "Measurement of the relaxation time τ_{21} of a Y₃Al₅O₁₂:Nd³⁺ crystal," Sov. J. Quantum Electron. **2**, 474 (1973).
- ⁹V. V. Grigor'yants, M. E. Zhabotinskii, and V. M. Markushev, "Determination of the probability of relaxation of the population of the ⁴I_{11/2} level of neodymium ions from luminescence dumping in a small external sample," Sov. J. Quantum Electron. **12**, 1010 (1982).
- ¹⁰V. P. Gaponstev, M. R. Sirtlanov, A. K. Gromov, A. A. Isineev, "New data on nonradiative relaxation of impurity center excitations in laser materials," Proceedings of the International Conference on Lasers '81 763 (STS Press, McLean, 1981).
- ¹¹W. E. Martin and D. Milam, "Direct measurement of gain recovery in a saturated Nd-glass amplifier," Appl. Phys. Lett. **32**, 816 (1978).
- ¹²C. Bibeau, S. A. Payne, and H. T. Powell, "Direct measurements of the terminal laser level lifetime in neodymium-doped crystals and glasses," submitted to the J. Opt. Soc. Amer. B.
- ¹³L. A. Riseberg and H. W. Moos, "Multiphonon orbit-lattice relaxation of excited states of rare-earth ions in crystals," Phys. Rev. **174**, 429 (1968).
- ¹⁴C. B. Layne, W. H. Lowdermilk, and M. J. Weber, "Multiphonon relaxation of rare-earth ions in oxide glasses," Phys. Rev. B **16**, 10 (1977).
- ¹⁵Y. E. Perlin, "Modern methods in the theory of many-phonon processes," Sov. Phys. **6**, 542 (1963).
- ¹⁶K. Huang and A. Rhys, "Theory of light absorption and non-radiative transition in F centres," Proceedings of the Royal Society of London A **204**, 406 (1950).
- ¹⁷A. Kiel, "The interaction of paramagnetic ions with lattice vibrations," Ph.D. Thesis, Johns Hopkins University, Baltimore MD (1962).

-
- ¹⁸R. Orbach, *Optical properties of ions in solids*, p. 445. (Wiley-Interscience Inc., New York, 1967).
- ¹⁹W. D. Partlow and H. W. Moos, "Multiphonon relaxation in $\text{LaCl}_3:\text{Nd}^{3+}$," *Phys. Rev.*, **157**, 252 (1967).
- ²⁰T. Miyakawa and D. L. Dexter, "Phonon sidebands, multiphonon relaxation of excited states, and phonon assisted energy transfer between ions in solids," *Phys. Rev. B*, **1** 2961 (1970).
- ²¹S. F. Fischer, "Correlation function approach to radiationless transitions," *J. Chem. Phys.* **53**, 3195 (1970).
- ²²T. F. Soules and C. B. Duke, "Resonant energy transfer between localized electronic states in a crystal," *Phys. Rev. B* **3**, 262 (1971).
- ²³F. K. Fong, S. L. Naberhuis, and M. M. Miller, "Theory of radiationless relaxation of rare-earth ions in crystals," *J. Chem. Phys.* **56**, 4020 (1972).
- ²⁴C. W. Struck and W. H. Fonger, "Unified model of the temperature quenching of narrow-line and broad-band emissions," *J. of Lumin.* **10**, 1 (1975).
- ²⁵Y. E. Perlin, A. A. Kaminskii, M. G. Blazha, V. N. Enakii, and V. V. Ryabchenkov, "Nonlinear electron-phonon interaction as cause of nonradiative transitions of TR^{3+} ions in crystals," *Sov. Phys. Solid State* **24**, 386 (1982).
- ²⁶K. Huang and Z. Gu, "Phonon analysis in multiphonon transitions," *Commun. Theor. Phys.* **1**, 535 (1982).
- ²⁷V. Gapontsev and M. Sirtlanov, "Progress in understanding of mechanisms of RE^{3+} -excited states nonradiative relaxation in crystals," *J. of Lumin.* **31&32**, 201 (1984).
- ²⁸L. M. Frantz and J. S. Nodvik, "Theory of pulse propagation in a laser amplifier," *J. Appl. Phys.* **34**, 2346 (1963).

Chapter 2

Measurements of the terminal level lifetime ($\tau_{11/2}$) for the ${}^4I_{11/2} \rightarrow {}^4I_{9/2}$ transition in 16 Nd-doped crystals and glasses using a novel pump and probe technique

2.1 Introduction

We have designed an experiment to directly measure the terminal level lifetime in several glassy and crystalline hosts. As discussed in Chapter 1, the value of the terminal level lifetime can be an important parameter in energy extraction models when terminal level lifetime begins to approach the extraction pulse width. We chose to investigate a variety of laser materials such as Nd:YAG and Nd:YLF as well as several Nd-doped phosphate and silicate glasses using a novel pump-probe method. In our experiment we were able to directly monitor the terminal level ${}^4I_{11/2}$ population as a function of time, thus making the results of the measurements more accurate than previous direct methods.

The basic concept of our experimental design is based on a pump and probe scheme shown in **Figure 2.1**. Because the ${}^4I_{11/2}$ state cannot be directly pumped from the ${}^4I_{9/2}$ state due to phonon host absorption in many materials, we use 2.41 μm light to pump the population from the ground state into the next higher level, or the ${}^4I_{13/2}$ state. After a time τ_d , a 1.06 μm beam then probes the population at the ${}^4I_{11/2}$ level by exciting a fraction of those ions to the ${}^4F_{3/2}$ level. These ions will subsequently emit radiation at 0.88 μm with a signal strength that is proportional to the population at the ${}^4I_{11/2}$ level. This process is repeated for a longer time delay, τ_d , and a new value for the integrated emission is obtained. The integrated emission signals are then plotted as a function of time delay between pump and probe. So as the ${}^4I_{11/2}$ population drains into the ground state, the 0.88 μm emission should decrease and the temporal evolution of the terminal level population will be recorded.

We first discuss in detail how the experiment was conducted and then describe the theoretical modeling, data fitting, and the uncertainties associated with our approach in the data analysis section. The data is presented in the results section along with a summary table. We next establish lower and upper limits on the $\tau_{11/2}$ lifetime and finally provide a summary of this work.

2.2 Experimental arrangement

The detailed experimental arrangement employed is shown in **Figure 2.2**. The 1.06 μm output from an Coherent mode-locked Nd:YAG laser operating at a repetition rate of 76 MHz is injected into a Continuum regenerative amplifier to produce a 10 Hz output of 55 mJ per pulse. The pulse widths are on the order of 100 ps at FWHM. The laser beam is then split into two pulses using a 20/80 beam splitter since two nonlinear processes are required to generate the 2.41 μm pump pulse. First, the more energetic pulse is focused into a Raman cell filled with hydrogen at a pressure of 55 atmospheres to provide a 1.91 μm first Stokes pulse and recollimated using a pair of 50 cm lenses chosen to match the length of the cell. Conversion to the first Stokes line is about 9%, producing 3.8 mJ at 1.91 μm . Next, the 1.06 μm beam (s polarized) from the original beam path and the 1.91 μm (p polarized) beams are weakly focused into a lithium niobate crystal specifically cut with respect to the proper phase matching angles for difference frequency conversion to 2.41 μm . The conversion efficiency to the 2.41 μm beam was about 8% of the total energy into the crystal which amounted to 500 μJ . A dispersive prism was used to separate the 2.41 μm and residual 1.06 μm beams so that the 1.06 μm beam could be sent into a variable delay line and used as the probe. The length of the delay line allowed for a maximum time delay of 6500 ps between the pump and probe pulses. The delay line was computer controlled and programmed to shift a corner cube in 50.8 ps steps between data points. In the 1.06 μm path, a filter was used to both reduce the energy and provide a reflected beam for a 1.06 μm reference detector ($R_{1.06}$). A reflection off of an uncoated beam splitter was used for the 2.41 μm reference detector ($R_{2.41}$). These detectors were used to account for the thermal background and shot to shot fluctuations of the pump and probe energies as discussed below.

The thermal background signal was significant since the ${}^4I_{11/2}$ level lies approximately 2000 cm^{-1} above the ground state and is therefore expected to hold about 10^{-4} of the ground state population. We found that the ${}^4I_{11/2}$ thermal population is large enough to produce an interfering signal compared to our induced signal. Therefore, before each data run, a measurement of the thermal background was taken by exciting the

sample with the 1.06 μm probe beam only. Without the pump beam present, this measurement provided a 0.88 μm emission signal that was proportional to the thermal population in the lower levels. The 0.88 μm emission was detected with an infrared sensitive photomultiplier tube positioned on the side of the sample with a narrow band filter placed directly in front of the detector. The ratio of the 0.88 μm signal to the 1.06 μm signal was then evaluated (referred to as B_{ratio}) and employed throughout the experimental run. During a data run, the inferred thermal background was accounted for by subtracting out the previously determined fixed ratio (B_{ratio}) from the 0.88 μm emission signal ($S_{0.88}$). However, in order to account for the fluctuating probe signal, the 0.88 μm emission signal ($S_{0.88}$) was normalized by the 1.064 reference signal ($R_{1.06}$) and B_{ratio} must be multiplied by $R_{1.06}$. The background subtracted signal shown in the parenthesis below is then normalized by the 2.41 μm reference signal ($R_{2.41}$) to account for fluctuations in the pump beam. The final expression employed to evaluate the terminal level population for each τ_d is:

$$S = \frac{\left(\frac{S_{0.88}}{R_{1.06}} - B_{\text{ratio}} \times R_{1.06} \right)}{R_{2.41}} \quad (1)$$

It is important to note that 0.88 μm emission signal and the background signal were generally found to be comparable in magnitude. For each shot, signals from all three detectors were sent into individual electronic boxcar signal integrators that were interfaced to a personal computer. Twenty shots were averaged for each time delay and the data was stored on floppy disk for subsequent numerical analysis.

2.3 Data analysis

A more detailed picture of the kinetic processes involved in the pump and probe scheme is shown in **Figure 2.3**. Here we include the existence of a complicating additional resonance at 1.06 μm that had not been previously discussed. This resonance causes the probe beam to simultaneously transfer population from both the $^4I_{11/2}$ and the $^4I_{13/2}$ levels to the upper $^4F_{3/2}$ and $^4F_{7/2}$ levels respectively followed by rapid nonradiative

relaxation through the ${}^4F_{5/2}$ and ${}^2H_{9/2}$ levels to the ${}^4F_{3/2}$ level. Therefore, the observed decay of 0.88 μm signal is a function of both the $\tau_{11/2}$ and $\tau_{13/2}$ lifetimes as well as the ratio of cross sections, $\sigma_{11/2}/\sigma_{13/2}$, (see **Figure 2.3**). Consequently, in order to determine the terminal level lifetime, we must fit our data to a model which includes these physical parameters. The simplified population rate equations used for modeling this system are:

$$\frac{dN_u}{dt} = \frac{I_{\text{probe}}(t)}{h\nu_{1.06}} (\sigma_{13/2}N_2 + \sigma_{11/2}N_1) - \frac{N_u}{\tau_u} \quad (2a)$$

$$\frac{dN_2}{dt} = \frac{I_{\text{pump}}(t)}{h\nu_{2.41}} \sigma_0 N_0 - \frac{N_2}{\tau_{13/2}} - \frac{I_{\text{probe}}(t)}{h\nu_{1.06}} \sigma_{13/2} N_2 \quad (2b)$$

$$\frac{dN_1}{dt} = -\frac{N_1}{\tau_{11/2}} + \frac{N_2}{\tau_{13/2}} - \frac{I_{\text{probe}}(t)}{h\nu_{1.06}} \sigma_{11/2} N_1 \quad (2c)$$

$$N_0 \approx \text{constant} \quad (2d)$$

with

$$I_{\text{probe}}(t) = A_{\text{probe}} \exp\left(-\left[\frac{t - \tau_d}{w_{\text{probe}}}\right]^2\right) \quad (2e)$$

$$I_{\text{pump}}(t) = A_{\text{pump}} \exp\left(-\left[\frac{t}{w_{\text{pump}}}\right]^2\right) \quad (2f)$$

where N_u is the combined population deposited in the upper ${}^4F_{3/2}$ and ${}^4F_{7/2}$ levels, N_2 and N_1 are the populations of the ${}^4I_{13/2}$ and ${}^4I_{11/2}$ levels respectively, and N_0 corresponds to the ${}^4I_{9/2}$ ground state population. The pump and probe intensities are denoted by $I_{\text{pump}}(t)$ and $I_{\text{probe}}(t)$ and were assumed to be Gaussian in character with widths of w_{pump} and w_{probe} respectively. For weak probe beams, as in our case, the last terms in 2b and 2c can usually be left out. In Eqns. 2 we have assumed that the pump and probe beams are weak so that $N_0 \gg N_1, N_2,$ and N_u . Based on the energy gap law expressed in Chapter 1, Eqn. 3, we expect the nonradiative lifetime for the ${}^4I_{13/2} \rightarrow {}^4I_{9/2}$ transition to be significantly longer than both the $\tau_{11/2}$ and $\tau_{13/2}$, lifetimes and therefore we do not include this nonradiative lifetime in our model. As a starting condition for the numerical solution, the probe beam is allowed to arrive several picoseconds ahead of the pump beam. Since the signal arising from the excitation of the thermal population of the lower levels is automatically accounted for in the data acquisition process (see Eqn. 1), there is no calculated emission

signal at the beginning of the solution. Overlap of the pump and probe peaks occurs in the steep rise of the 0.88 μm signal. As the solution advances, the probe and pump pulses will no longer overlap and the probe beam will eventually arrive at times long after the pump pulse. This approach allows us to model the entire 0.88 μm emission signal and include the overlap effects of the pump and probe pulses in the population decays. For each incremental time delay (τ_d), the coupled differential equations are solved using a standard Runge-Kutta integration routine¹.

For each material, the solution to the above equations involves three variable parameters: $\tau_{11/2}$, $\tau_{13/2}$, and $\sigma_{11/2}/\sigma_{13/2}$, and the following scaling factors: τ_u , σ_0 , A_{pump} , and A_{probe} . The spontaneous 0.88 μm emission lifetime (τ_u), the cross section for the ${}^4\text{I}_{9/2} \rightarrow {}^4\text{I}_{13/2}$ transition (σ_0), and the pump and probe amplitudes (A_{pump} , A_{probe}), only effect the overall magnitude of the 0.88 μm emission signal. Since the data only depends on the relative changes of the 0.88 μm signal for each time delay of the probe pulse, the precise values of these scaling parameters are unimportant. The pump and probe pulse widths were determined from fitting the model to the Nd:YLF data taken with high (2.54 ps) temporal resolution. We chose this material because its long (>10 ns) relaxation time assures us that the risetime due to the laser pulse widths can be unambiguously separated out. The pulse widths were fit with an accuracy of $\pm 25\%$ using $w_{\text{pump}} = w_{\text{probe}} = 50$ ps.

In trying to fit the numerical solution to the data, we initially tried to independently vary all three of the parameters ($\tau_{11/2}$, $\tau_{13/2}$, $\sigma_{11/2}/\sigma_{13/2}$) in order to find the best fit, but in doing so, we found that different sets of parameters produced similar fits to the data. We next discuss how the fits to the data varied as we changed the parameters, and what constraints were imposed to find the best fit. LG-750, a phosphate glass, was chosen as the representative material for our analysis and discussion.

In order to find the best fit to the data we varied the cross section ratio, $\sigma_{11/2}/\sigma_{13/2}$, and the $\tau_{11/2}$ lifetime while holding the lifetime ratio, $\tau_{13/2}/\tau_{11/2}$, fixed until we found the minimum fitting error (χ^2). As an example, by setting $\tau_{13/2}/\tau_{11/2} = 1$, we found the values of $\tau_{11/2} = 450$ ps and $\sigma_{11/2}/\sigma_{13/2} = 1.4$ gave the minimum fitting error. These values are

plotted on the graphs shown in **Figures 2.4a and b**. **Figure 2.4a** shows the corresponding fitting error for each of the lifetime ratios plotted and **Figure 2.4b** shows the corresponding value of the cross section ratio that gave the minimum fitting error. We found that as we tried to increase the imposed ratio of lifetimes, we also had to increase the ratio of cross sections. However, in the process, the minimum fitting error increased.

In order to find limits for the range of acceptable values (shown by the two gray shaded areas on the plots) We used two independent assessments. Based on the quality of the fit, we believe that the range of acceptable errors should be less than roughly twice the minimum error as indicated by the gray shaded area in **Figure 2.4a**. Secondly, using an independent calculation for the ratio of the cross sections for LG-750 based on the Judd² and Ofelt³ theory, we calculated the $\sigma_{11/2}/\sigma_{13/2}$ ratio to be approximately 0.8 (See Appendix 2A). Based on the uncertainties in the Judd-Ofelt calculation (usually a factor of two), we assigned the range of allowable cross sections to be between 0.4 and 1.6 which is indicated by the gray shaded area in **Figure 2.4b**. Lastly, we mention that the vertical dotted line corresponds to a constraint imposed by the energy gap law, whereby the decreasing nonradiative rate with increasing energy gap suggests that the ratio of the lifetimes ($\tau_{13/2}/\tau_{11/2}$) should be no less than one since the ${}^4I_{13/2} \rightarrow {}^4I_{11/2}$ gap is always greater than the ${}^4I_{11/2} \rightarrow {}^4I_{9/2}$ gap.

We can now use the plots of **Figures 2.4a and b** to provide an assessment as to the range of reasonable $\tau_{13/2}/\tau_{11/2}$ values that should be employed. If we constrain the $\tau_{13/2}/\tau_{11/2}$ ratio to fall within both of the gray shaded areas in **Figures 2.4a and 2.4b**, we find that the $\tau_{13/2}/\tau_{11/2}$ values between approximately one and two are acceptable to model the acquired LG-750 phosphate data. Therefore, in order to satisfy the requirements of minimizing the fitting error while using a reasonable value for the ratio of cross sections, we chose to constrain the lifetimes to be equal to one another ($\tau_{11/2} = \tau_{13/2} = \tau_{\text{eff}}$) for all of the materials studied. This constraint is consistent with the possibility that the ${}^4I_{13/2} \rightarrow {}^4I_{11/2}$ and ${}^4I_{11/2} \rightarrow {}^4I_{9/2}$ transitions occur over averaged, similar sized energy gaps. If we consider the 300-1000 cm^{-1} spread in the crystal field levels within the 4I_J manifolds with respect to 1200-1700 cm^{-1} gap between the 4I_J electronic states, we can assume the possibility of

an averaging effect over which these population decays take place. If this averaging effect were highly effective, then the $\tau_{11/2} = \tau_{13/2} = \tau_{\text{eff}}$ would hold exactly. If the averaging among the different crystal field levels were not important, then the τ_{eff} would serve as an *upper limit*, since the decay should be faster for the approximately 200 cm^{-1} smaller ${}^4\text{I}_{11/2}$ - ${}^4\text{I}_{9/2}$ energy gap compared to the ${}^4\text{I}_{13/2}$ - ${}^4\text{I}_{11/2}$ separation. Therefore, for each material, we varied the effective lifetime, τ_{eff} , and the cross section ratio, $\sigma_{11/2}/\sigma_{13/2}$, until the errors in the fit to the data were minimized. This process allows us to calculate an upper limit on the $\tau_{11/2}$ terminal level lifetime, and in a later section the energy gap law is used to derive an expression for a lower limit. As we will show, this approach adequately modeled the data well for nearly all of the materials investigated.

2.4 Results and fit to kinetic model

We selected a variety of samples for which we assessed the terminal level lifetime. The sample selection was chosen to be representative of the different types of materials that are important to laser technology. As listed in **Table 2.1** we examined 5 different phosphates including 4 glasses (LG-750, APG-1, and the experimental glasses: APG-x and APG-y) and one crystal known as fluorapatite or C-FAP ($\text{Ca}_5(\text{PO}_4)_3\text{F}$). We looked at three silicate glasses: LG-660, LG-650 and a Nd-doped fused silica (SiO_2) prepared by a sol-gel synthesis route⁴. Several of the common oxide crystals were studied: YAlO_3 (YALO), $\text{Gd}_3\text{Sc}_2\text{Ga}_3\text{O}_{12}$ (GSGG), and $\text{Y}_3\text{Al}_5\text{O}_{12}$ (YAG). In addition, we considered four fluoride hosts that included two crystals: SrF_2 and LiYF_4 (YLF), and two glasses: ZBLAN and LG-812 (a fluorophosphate glass). Lastly, we include one crystal from the vanadate group, YVO_4 .

The data and modeled fits for several of the materials investigated at room temperature are shown in **Figures 2.5 and 2.6**. In each plot, the integrated $0.88 \mu\text{m}$ signal is plotted as a function of the time delay (τ_d) between the pump and probe pulses. The maximum time delay of 6500 ps permitted by our translation stage was adequate for most of the lifetimes measured, although for all the fluoride materials investigated, additional data was needed. We were able to take an additional 6000 ps of lifetime data by moving

the delay line further back and repeating the pump-probe experiment in the new location. This was only done for YLF since the ZBLAN and SrF₂ data were too noisy. Therefore, only the YLF plot in **Figure 2.6** consists of two connected data runs. In an effort to reduce the statistical noise, a minimum of three data runs were averaged together for each sample. In addition, the data has been smoothed with a three point weighted average; the center point was weighted by two and the points on either side of the center point were weighted by unity.

In **Table 2.1**, we list the materials names and chemical formulas along with the corresponding fitted values of τ_{eff} and $\sigma_{11/2}/\sigma_{13/2}$. We also include the averaged energy gap (ΔE_{ave}) between ${}^4I_{13/2}$ - ${}^4I_{11/2}$ and ${}^4I_{11/2}$ - ${}^4I_{9/2}$ levels, effective phonon energy ($h\nu_{\text{eff}}$), and the normalized energy gap ($p=\Delta E_{\text{ave}}/h\nu_{\text{eff}}$). Recall from Chapter 1 that the energy gap law expresses the nonradiative rate as: $W_{\text{nr}}=A \exp(-\kappa p)$, where A and κ are host dependent parameters. For all of the crystals investigated, the energy gaps for the ${}^4I_{13/2}$ - ${}^4I_{11/2}$ and ${}^4I_{11/2}$ - ${}^4I_{9/2}$ separations were obtained from the literature and are referenced in **Table 2.1**.^{5,6,7,8} For the glasses, we experimentally deduced the energy separations from the emission spectra for each of the samples. In order to determine the energy gap between the lowest upper multiplet and the highest lower multiplet for the ${}^4I_{13/2} \rightarrow {}^4I_{11/2}$ transition, the horizontal distance between the falling edge of the 1.06 μm emission peak and rising edge of the 1.31 μm emission peak was measured at the half maximum of each peak. A similar calculation was done for the ${}^4I_{11/2} \rightarrow {}^4I_{9/2}$ transition. The two measured energy gaps were then averaged together to obtain a value for ΔE_{ave} . The effective phonon frequencies for each material are also referenced in **Table 2.1**^{9,10,11,12,13,14,15,16,17,18} with the exception of the GSGG and the ZBLAN materials, where we instead used the referenced effective phonon frequencies of the GGG¹³ and ZBLN¹⁷ materials respectively since no vibrational data could be found. These substitutions were made because the effective phonon frequencies are expected to be similar. For example, since the ZrF₄ complex comprises the highest concentration of molecular species in both the ZBLN and ZBLAN glasses and since this complex is believed to be responsible for the high frequency vibrations in ZBLN¹⁷, we can assume that ZBLAN should exhibit the same high

frequencies as ZBLN. A similar argument can also be made for the GaO_4 complex which is present in both the GSGG and GGG crystals.

The phosphate and silicate materials investigated all have effective lifetimes of less than a nanosecond. These short lifetimes are primarily due to the high phonon frequencies ($1000\text{--}1200\text{ cm}^{-1}$) which allow for low order phonon processes ($p < 2$). Within the oxide group, we find that YAG has an extremely short lifetime of 225 ps whereas for all of the fluoride materials, we find that the larger gaps coupled with the lower phonon frequencies lead to long effective lifetimes in the nanosecond regime. Within each of the phosphate, silicate, and oxide groups we find that a decrease in the effective lifetime τ_{eff} roughly corresponds to a decrease in the order of the process, p (within experimental error). This observation qualitatively agrees with expectation for the energy gap law at a fixed temperature. This comparison could not be made for the fluoride materials since noise prevented us from taking reliable data for the ZBLAN and SrF_2 hosts, although we can make qualitative observations based on the order of their processes. Since YLF and ZBLAN have similar effective phonon frequencies and averaged energy gaps (and therefore similar $p = \Delta E_{\text{ave}} / h\nu_{\text{eff}}$ values) we would expect ZBLAN to have a terminal level lifetime comparable to that of YLF whereas SrF_2 should have a longer lifetime than YLF since the order of the process, p , is larger.

The fluorophosphate data could not be modeled with a single effective lifetime and instead was fitted with two lifetimes of 650 and 5300 ps. The unusually large difference between these lifetimes indicates that the discrepancy between the lifetimes is too large to be associated with the difference in energy gap between the ${}^4\text{I}_{13/2} \rightarrow {}^4\text{I}_{11/2}$ and ${}^4\text{I}_{11/2} \rightarrow {}^4\text{I}_{9/2}$ transitions. So, while we can fit the data with our model, the physical origin of the two lifetimes is different. The fluorophosphate material has a distribution of phosphate and fluoride anions and therefore each Nd ion will be surrounded by a different concentration of these species. The Nd ions that have more phosphates nearby, will naturally have a faster decay rate than those Nd ions that are surrounded predominately by fluorides since the PO_4 species typically possesses vibrations with $1000\text{--}1200\text{ cm}^{-1}$ energies, while the fluorides are closer to $400\text{--}600\text{ cm}^{-1}$. The presence of the phosphates accelerates the energy transfer to the surrounding medium and therefore we might

associate the lifetimes with two energy transfer processes occurring over different time scales; the shorter 650 ps phenomena could be attributed to the phosphate or PO_4 complexes while the longer 5300 ps decay time could be due to the lower phonon frequency fluoride ions. Although there is not enough data to analyze this detail, it is our assumption that an increase in the relaxation decay rate is mediated by the proximity of the phosphates.

Based on either the Judd-Ofelt cross section analysis or emission spectra we found that the cross section ratios listed in **Table 2.1** are reasonable. The phosphate and silicate glasses all have a calculated ratio close to one. The SiO_2 (sol-gel prep.) and the crystalline materials of YALO, YAG, C-FAP, and YVO_4 are all expected to have a cross section ratio significantly greater than one, since there is a strong emission line for the ${}^4\text{F}_{3/2} \rightarrow {}^4\text{I}_{11/2}$ transition at 1.06 μm , suggestive of an exact 1.06 μm energy resonance between the ${}^4\text{F}_{3/2}$ and ${}^4\text{I}_{11/2}$ levels. We might expect a smaller ratio for GSGG and the fluoride materials, since the strong emission lines occur at a different wavelength from the 1.06 μm probe beam.

The doping levels for the 16 crystalline materials investigated roughly ranged from 0.2-2% whereas for the glasses, the concentrations ranged from 2-5 weight %. We measured the effective lifetime for two additional samples of LG-750 and LG-660 with increased doping levels of 4 wt % and 8 wt % respectively and found no difference in the effective lifetimes. This was to be expected since concentration dependent phenomena such as energy transfer normally occur on longer (microsecond) time scales compared to the picosecond lifetimes measured here. We cannot be sure however that this result is completely general since some crystals could have accidental resonances that lead to enhanced transfer rates.

2.5 Evaluation of the lower limit to the ${}^4\text{I}_{11/2}$ lifetime

In **Figure 2.7** we plot the τ_{eff} and ΔE_{ave} values along with lifetime data taken from the literature^{9,12,18,19,20,21} for many nonradiative transitions that occur across the energy gaps lying above the ${}^4\text{F}_{3/2}$ metastable level and for other rare-earth ions within the same materials. A best fit line was drawn through the data for each plot. We did not include the

data relating to SrF₂ and ZBLAN since our data point only represented an upper bound. For most of the materials we utilized the data in **Figure 2.7** to calculate the slope, γ , of the best fit line. Based on the energy gaps ($\Delta E_{13/2}$, $\Delta E_{11/2}$) and the slope (γ), we calculate the expected ratio of lifetimes of the ${}^4I_{13/2}$ and ${}^4I_{11/2}$ levels, $R_{\text{life}} = \tau_{13/2}/\tau_{11/2}$, for each material to be:

$$\frac{\tau_{13/2}}{\tau_{11/2}} = \frac{A \exp(-\gamma \Delta E_{11/2})}{A \exp(-\gamma \Delta E_{13/2})} = \exp(\gamma \Delta E_{\text{diff}}) = R_{\text{life}} \quad (3a)$$

where $\Delta E_{\text{diff}} = \Delta E_{13/2} - \Delta E_{11/2}$ (3b)

The values R_{life} as well as ΔE_{diff} and γ are listed in **Table 2.2**^{5,6,7,8}

The values of R_{life} represent the lifetime ratio that should exist if the energy gap law were rigorously applicable in the small gap (< 2) limit. Since this physical law was originally intended to apply to the 2-4 phonon range, it was not apparent whether it is applicable for describing the small gaps of the ${}^4I_{13/2} \rightarrow {}^4I_{11/2} \rightarrow {}^4I_{9/2}$ relaxations. The main manner in which we might expect the energy gap law to break down would involve a kind of averaging effect where the relaxation rates would approach a limiting value. This averaging might occur because the splitting among the crystal field levels of each 4I_j electronic state becomes comparable to the gaps between the 4I_j states. As a consequence, many relaxation sequences become possible between different pairs of crystal field levels and this averaging causes the $\tau_{11/2}$ and $\tau_{13/2}$ lifetimes to become equal. This is the case relating to the assignment of the τ_{eff} values for an upper limit, as discussed above. On the other hand, the assumption of full applicability for the energy gap law would naturally provide a *lower limit* to the value of the $\tau_{11/2}$ of the ${}^4I_{11/2}$ level. The $\tau_{11/2}$ value should be less than the τ_{eff} quantity derived from the fits of **Figures 2.5 and 2.6** since the ${}^4I_{11/2} - {}^4I_{9/2}$ energy gap is known to be typically $\sim 200 \text{ cm}^{-1}$ smaller than the ${}^4I_{13/2} - {}^4I_{11/2}$ gap. In order to calculate the lower limit we need to combine the τ_{eff} fitted value with the imposed constraint of R_{life} in order to calculate the lower limit value. We have found through extensive computer fittings of the data that we were able to devise a simple empirical relationship between the effective lifetime τ_{eff} and the pairs of $\tau_{11/2}$, $\tau_{13/2}$ values that

minimized the χ^2 fitting error. We in fact found that the geometrical mean adequately represents this relationship:

$$\tau_{\text{eff}} = \sqrt{\tau_{11/2} \times \tau_{13/2}} \quad (4a)$$

Using Eqns. 3a and b to substitute for $\tau_{13/2}$ we then have

$$\tau_{11/2} = \frac{\tau_{\text{eff}}}{\sqrt{R_{\text{life}}}} \quad (4b)$$

On the basis of the above definition for $\tau_{11/2}$ and the data in **Table 2.1** along with the slopes derived from **Figure 2.7** the lower limits are calculated and listed in **Table 2.2** along with the corresponding ${}^4I_{11/2}$ energy gaps. The slopes for C-FAP and GSGG were estimated using the phosphate and GGG data respectively. We did not calculate a lower limit for SrF_2 and ZBLAN since the τ_{eff} lifetimes could not be accurately measured.

We reviewed the literature for comparisons to other direct terminal level lifetime measurements and we found data for the phosphate and silicate glasses and YLF that compared well with our data. The gain saturation data taken by Yarema and Milam²² for the Nd-doped phosphate glass LG-750 and modeled by Bibeau et al.²³ with Eqn. 3 for the saturation fluence, yielded a $\tau_{11/2}$ value of 280 ± 100 ps. In the gain recovery measurements made by Martin and Milam²⁴ for a Nd-doped silicate glass similar to LG-660, they determined the lifetime to be 1250 ± 200 ps from directly observing the gain recovery after the passage of a saturating pulse. In a recent gain recovery experiment conducted by Palombo and coworkers²⁵ they determined the lifetime to be approximately 20 ns for Nd:YLF. In comparison, our data on Nd:LG-750, LG-660 and YLF yielded ranges of 250-450 ps, 535-750 ps and 10.5-20 ns respectively. The luminescence decay measurements made by Basiev and coworkers¹⁹ are of the nonradiative relaxation rate for the ${}^4G_{7/2}$ level in Nd:YALO, GSGG, YAG, and YLF and represent an indirect method. Their values yielded lifetimes that fall within our upper and lower $\tau_{11/2}$ bounds for similar sized gaps, with the exception of Nd:YAG, where their lifetime of 370 ps was longer than our upper limit of 225 ps. Although our $\tau_{11/2}$ lower limits appear to be shorter than all the above reported lifetimes, they nevertheless represent an improvement over the previous levels of discrepancy encountered in the literature.

2.6 Conclusion

We have directly measured the terminal level lifetime for several crystalline and glassy materials using a novel pump (2.41 μm) and probe (1.06 μm) scheme. This method allows us to infer the population decays from the ${}^4\text{I}_{13/2}$ and ${}^4\text{I}_{11/2}$ levels by measuring the integrated 0.88 μm emission signal. The time resolution of the population decays from these two levels is achieved by plotting the integrated 0.88 μm signal as a function of the time delay between the pump and probe pulses. As a consequence of directly pumping the ground state population into the ${}^4\text{I}_{13/2}$ level, the data is found to be a function of both the $\tau_{13/2}$ and $\tau_{11/2}$ lifetimes (the ${}^4\text{I}_{13/2}$ and ${}^4\text{I}_{11/2}$ levels respectively). Furthermore, since the probe beam simultaneously excites two resonance transitions at the 1.06 μm wavelength, the ratio of cross sections for these transitions must also be considered ($\sigma_{11/2}/\sigma_{13/2}$). Therefore, our computer model of the data primarily depends upon three independent physical parameters: $\tau_{13/2}$, $\tau_{11/2}$ and $\sigma_{11/2}/\sigma_{13/2}$. On the basis of our fitting analysis however, we set the $\tau_{11/2}$ and $\tau_{13/2}$ lifetimes to be equal to one another and defined an effective lifetime ($\tau_{11/2} = \tau_{13/2} = \tau_{\text{eff}}$) that corresponds to the averaged energy gap for the ${}^4\text{I}_{13/2} \rightarrow {}^4\text{I}_{11/2}$ and ${}^4\text{I}_{11/2} \rightarrow {}^4\text{I}_{9/2}$ transitions. Therefore, the data uniquely determined only two parameters. Through further analysis, we incorporated the gap law theory to account for the $\sim 200 \text{ cm}^{-1}$ smaller energy gap corresponding to the ${}^4\text{I}_{11/2} \rightarrow {}^4\text{I}_{9/2}$ transition. This allows us to estimate the difference between the $\tau_{11/2}$ and $\tau_{13/2}$ lifetimes and establish upper and lower limits for the $\tau_{11/2}$ lifetime.

Based on comparisons with other data from the literature we found agreement within a factor of two for the phosphate and silicate glasses, the oxide crystals of YALO, GGG, and YAG, and the fluoride crystal, YLF. Our results seem to indicate that the energy gap law is still valid for energy separations on the order of 1500 cm^{-1} . As is to be expected, we did not see any neodymium concentration dependence on the lifetimes since the time scales associated with inter-ion energy transfer processes are generally much longer (microseconds) compared to the picosecond to nanosecond nonradiative relaxation lifetimes measured here. The temperature dependence of Eqn. 3 in Chapter 1, is dependent on the order of the process (p). With the exception of the fluoride materials,

most of the materials investigated have p values that are less than 2 and therefore, we do not expect to see any significant differences for the low temperature rates. In conclusion, we have demonstrated a unique method of measuring the terminal level lifetime for several important laser media and through our analysis have determined upper and lower bounds for the $\tau_{11/2}$ lifetime. Several examples of our experimental results include 115-225 ps for Nd:YAG, 250-450 ps for Nd:LG-750, and 10.5-20 ns for Nd:YLF.

Appendix 2A

The absorption cross sections for the ${}^4I_{11/2} \rightarrow {}^4F_{3/2}$ and ${}^4I_{13/2} \rightarrow {}^4F_{7/2}, {}^4S_{3/2}$ transitions (referred to as $\sigma_{11/2}$ and $\sigma_{13/2}$ in text) were calculated using the Judd² and Ofelt³ method of absorption intensity analysis for rare-earth ions. The Judd-Ofelt method can also be used to calculate radiative lifetimes and branching ratios once the line strength, $S(aJ:bJ')$, for the particular transition of interest has been determined. The expression utilized for the absorption cross section calculation is shown below²⁶:

$$\sigma = \frac{8 \pi^3 e^2 \lambda (n^2 + 2)^2 S(aJ:bJ')}{27 c h n (2J + 1) \Delta\lambda_{\text{eff}}} \quad (\text{A1})$$

where $(2J+1)$ is the degeneracy of the initial state (aJ), $\Delta\lambda_{\text{eff}}$ is the effective linewidth of the transition, λ is the average wavelength of the transition, e , c , and h , are fundamental physical constants, and n is the index of refraction at wavelength λ . The line strength can be written as a sum of products in the form:

$$S(aJ:bJ') = \sum_{t=2,4,6} \Omega_t \times \langle aJ \| U^{(t)} \| bJ' \rangle^2 \quad (\text{A2})$$

where the matrix elements $\langle U^{(t)} \rangle$ represent the doubly reduced unit tensors operating between the intermediate-coupled eigenstates (aJ) and (bJ') of the free ion. The intensity parameters Ω_t will vary depending on the local environment and therefore they must be experimentally determined for each host from a least squares fit of the measured and calculated integrated absorption band strengths.

Using Eqns. A1 and A2, the ratio of cross sections can be written as:

$$\frac{\sigma_{11/2}}{\sigma_{13/2}} = \frac{14 \lambda_{11/2} \Delta\lambda_{13/2} S_{11/2}}{12 \lambda_{13/2} \Delta\lambda_{11/2} S_{13/2}} \quad (\text{A3})$$

$$\text{with } S_{11/2} = 0.1423 \times \Omega_4 + 0.4083 \times \Omega_6 \quad ({}^4I_{11/2} \rightarrow {}^4F_{3/2}) \quad (\text{A4})$$

$$S_{13/2} = 0.3314 \times \Omega_4 + 0.3259 \times \Omega_6 \quad ({}^4I_{13/2} \rightarrow {}^4F_{7/2}, {}^4S_{3/2}) \quad (\text{A5})$$

where the $\langle U^{(t)} \rangle$ elements in (A4) and (A5) were obtained from the literature for the neodymium ion²⁷ and the 11/2 and 13/2 subscripts denote the identity of the initial (${}^4I_{11/2}$ and ${}^4I_{13/2}$) state of the transition. The effective linewidths employed by Eqn. A3 have been

inferred from the absorption spectra of the ground state (${}^4I_{9/2}$) to the relevant final electronic states (${}^4F_{3/2}$ and ${}^4F_{7/2}$, ${}^4S_{3/2}$).

Table 2.1 A summary table of fitted results and energy gap parameters: the effective lifetime (τ_{eff}), ratio of cross sections ($\sigma_{11/2}/\sigma_{13/2}$), averaged energy gap (ΔE_{ave}), effective phonon energy ($h\nu_{\text{eff}}$), and normalized energy gap (p).

Material	Formula	τ_{eff} (ps)	$\frac{\sigma_{11/2}}{\sigma_{13/2}}$	ΔE_{ave} (cm^{-1})	$h\nu_{\text{eff}}$ (cm^{-1})	p $\frac{\Delta E_{\text{ave}}}{h\nu_{\text{eff}}}$
Phosphate						
LG-750	$\text{P}_2\text{O}_5\text{-Al}_2\text{O}_3+\dots$	450	1.4	1671	1100 ⁹	1.52
APG-1	$\text{P}_2\text{O}_5\text{-Al}_2\text{O}_3+\dots$	380	1.7	1612	1100 ⁹	1.47
APG-x	$\text{P}_2\text{O}_5\text{-Al}_2\text{O}_3+\dots$	375	1.5	1578	1100 ⁹	1.43
APG-y	$\text{P}_2\text{O}_5\text{-Al}_2\text{O}_3+\dots$	310	1.6	1606	1100 ⁹	1.46
C-FAP	$\text{Ca}_5(\text{PO}_4)_3\text{F}$	200	5.0	1251 ⁵	1080 ¹⁰	1.16
Silicate						
LG-660	$\text{SiO}_2\text{-K}_2\text{O-ZnO}+\dots$	740	2.0	1411	1000 ⁹	1.41
LG-650	$\text{SiO}_2\text{-K}_2\text{O}+\dots$	680	1.6	1375	1000 ⁹	1.38
Sol-gel prep.	$\text{SiO}_2\text{-Al}_2\text{O}_3$	350	3.0	1336	1200 ¹¹	1.11
Oxide						
YALO	YAlO_3	1900	3.8	1464 ⁶	750 ¹²	1.95
GSGG	$\text{Gd}_3\text{Sc}_2(\text{GaO}_4)_3$	1175	3.5	1347 ⁷	742 ^{b, 13}	1.82
YAG	$\text{Y}_3\text{Al}_2(\text{AlO}_4)_3$	225	3.5	1273 ⁶	860 ¹⁴	1.48
Fluoride						
SrF ₂	SrF_2	> 5ns	1.0	1467 ⁸	360 ¹⁵	4.08
YLF	LiYF_4	20ns	1.0	1577 ⁶	560 ¹⁶	2.82
ZBLAN	$\text{ZrF}_4\text{-BaF}_2\text{-AlF}_3\text{-LaF}_3\text{-NaF}$	> 5ns	1.0	1615	580 ^{c, 17}	2.78
Vanadate						
YVO ₄	YVO_4	870	6.0	1626 ⁶	943 ¹⁸	1.72
Fluorophosphate						
LG-812		650,5300 ^a	3.0	1550	1000 ¹¹	1.55

(a) Cannot be fit to a single τ_{eff} value.

(b) Based on GGG phonon data.

(c) Based on ZBLN phonon data.

Table 2.2 A summary table of the $\tau_{11/2}$ upper and lower limits and corresponding energy gaps, $\Delta E_{11/2}$. The lower limit was established from an expression that included the slope (γ), energy difference (ΔE_{diff}), and ratio of lifetimes ($\tau_{13/2}/\tau_{11/2}$) expected from the slope of the decay rate versus energy gap plots.

Material	γ 10^{-3} (cm^{-1})	ΔE_{diff} (cm^{-1})	R_{life} $\tau_{13/2}/\tau_{11/2}$	$\tau_{11/2}$ limits (ps)		$\Delta E_{11/2}$ (cm^{-1})
				Upper	Lower	
Phosphate						
LG-750	4.67	252	3.24	450	250	1545
APG-1	4.67	293	3.93	380	192	1465
APG-x	4.67	268	3.50	375	200	1444
APG-y	4.67	288	3.84	310	158	1462
C-FAP	4.67 ^a	107	1.65	200	-156	1197 ⁵
Silicate						
LG-660	4.11	158	1.91	740	535	1332
LG-650	4.11	140	1.78	680	510	1305
SiO ₂ (Sol-gel prep.)	4.11	170	2.01	350	247	1251
Oxide						
YALO	6.75	223	4.50	1900	896	1352 ⁶
GSGG	8.21 ^b	262	8.59	1175	-401	1216 ⁷
YAG	5.24	256	3.82	225	115	1145 ⁶
Fluoride						
SrF ₂	—	216	—	>5ns	—	1359 ⁸
YLF	6.01	214	3.62	20ns	10.5	1470 ⁶
ZBLAN	—	324	—	>5ns	—	1453
Vanadate						
YVO ₄	4.81	205	2.68	870	531	1523 ⁶

(a) Value estimated from phosphate glass data.

(b) Estimated from GSGG and GGG data combined.

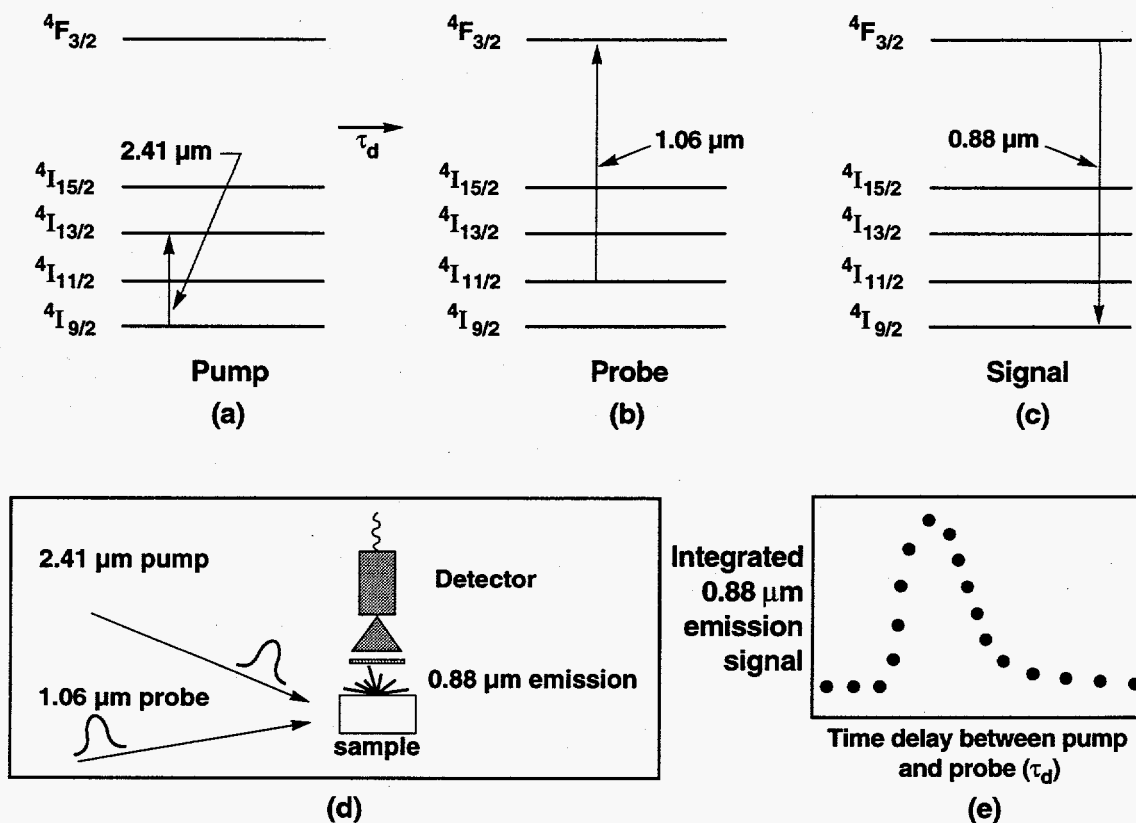


Figure 2.1 Illustration of the pump ($2.41 \mu\text{m}$) and probe ($1.06 \mu\text{m}$) method employed in our experiment. A 100 ps pump pulse is used to excite a fraction of the $4I_{9/2}$ ground state population into the $4I_{13/2}$ level (a). After a time τ_d , a weak probe pulse then probes the $4I_{11/2}$ population by exciting a fraction of these ions to the upper $4F_{3/2}$ level (b). The resulting $0.88 \mu\text{m}$ emission signal is then recorded and integrated (c). Experimentally, the pump and probe beams are focused into the sample with a detector placed on the side to record the $0.88 \mu\text{m}$ emission signal (d). Therefore, as the $4I_{11/2}$ population returns back down to the $4I_{9/2}$ ground state, the relative integrated $0.88 \mu\text{m}$ signal strength will decrease and enable us to infer the $\tau_{11/2}$ lifetime (e).

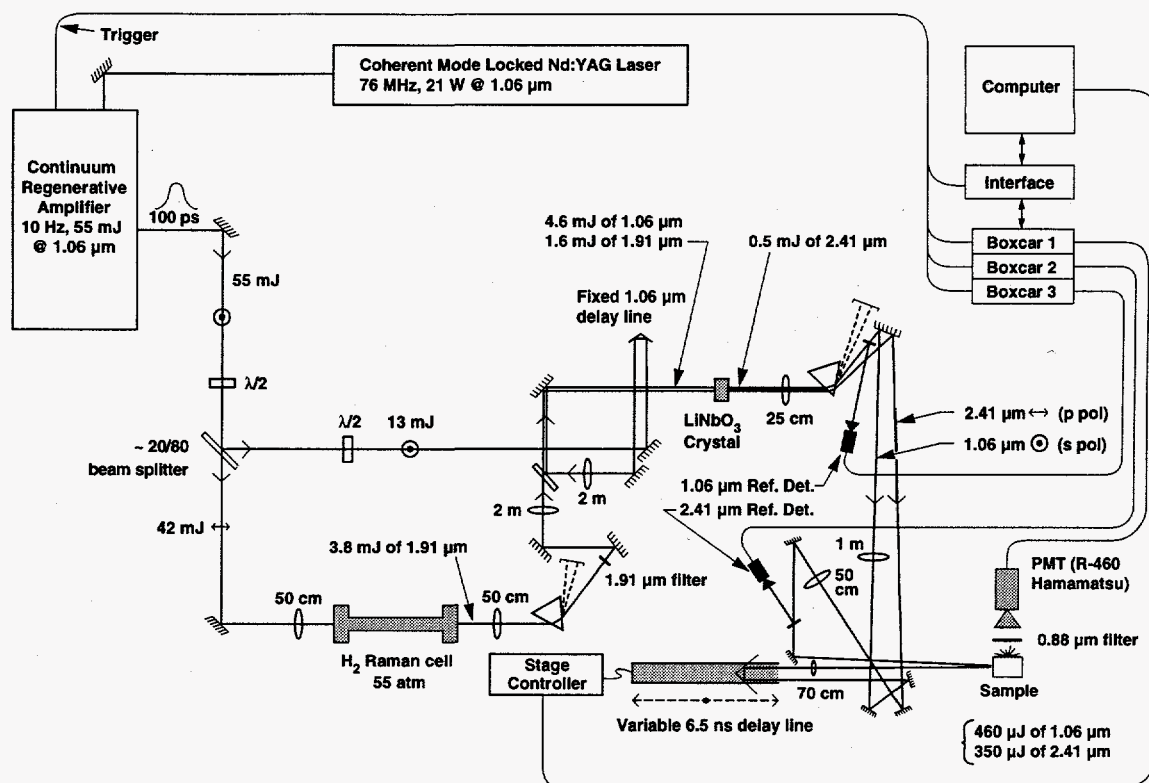


Figure 2.2 Detailed schematic of the experimental arrangement used to measure the terminal level lifetime. A 100 ps pulse is first passed through a $\sim 20/80$ beamsplitter. The more energetic, transmitted beam is focused into a high pressure H_2 Raman cell where 9% of the incident $1.06 \mu\text{m}$ energy is converted to the first Stokes frequency at $1.91 \mu\text{m}$. The $1.91 \mu\text{m}$ light is then combined with the $1.06 \mu\text{m}$ light from the upper path into a LiNbO_3 crystal to generate $\sim 0.5 \text{ mJ}$ of $2.41 \mu\text{m}$ energy. A prism separates the $2.41 \mu\text{m}$ (pump) from the $1.06 \mu\text{m}$ (probe) beams so that the $1.06 \mu\text{m}$ beam can be sent into a computer controlled variable delay line. The pump and probe beams are then focused into the sample with a PMT detector placed on the side to record the $0.88 \mu\text{m}$ signal ($S_{0.88}$). The $1.06 \mu\text{m}$ reference detector ($R_{1.06}$) and the $2.41 \mu\text{m}$ reference detector ($R_{2.41}$) also shown are used to correct for the ${}^4\text{I}_{11/2}$ thermal population and energy fluctuations in the $1.06 \mu\text{m}$ and $2.41 \mu\text{m}$ energies. All of the signals ($S_{0.88}$, $R_{1.06}$, and $R_{2.41}$) are electronically sent into the boxcars integrators and then to the computer where the data is stored for post analysis.

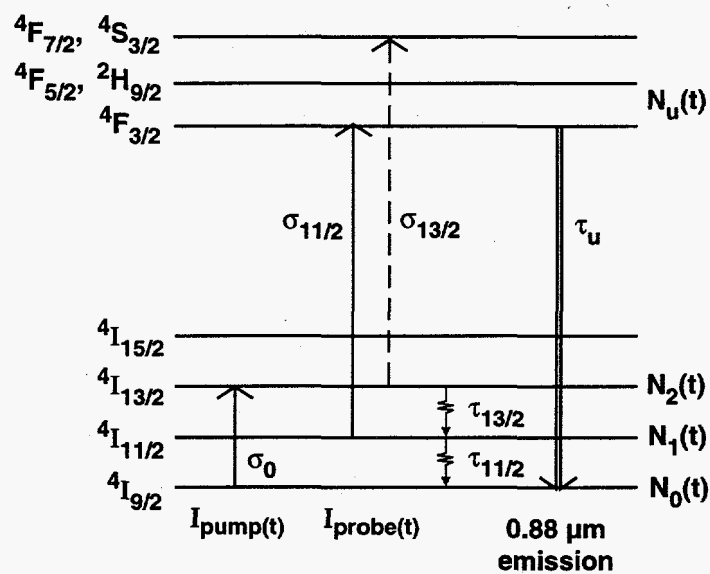


Figure 2.3 A more detailed diagram of the Nd energy levels showing the additional resonance (dashed line) excited by the $1.06 \mu\text{m}$ probe beam. The diagram also identifies the populations: N_0 , N_1 , N_2 , and N_u , used in the rate equations for the modeling of the data.

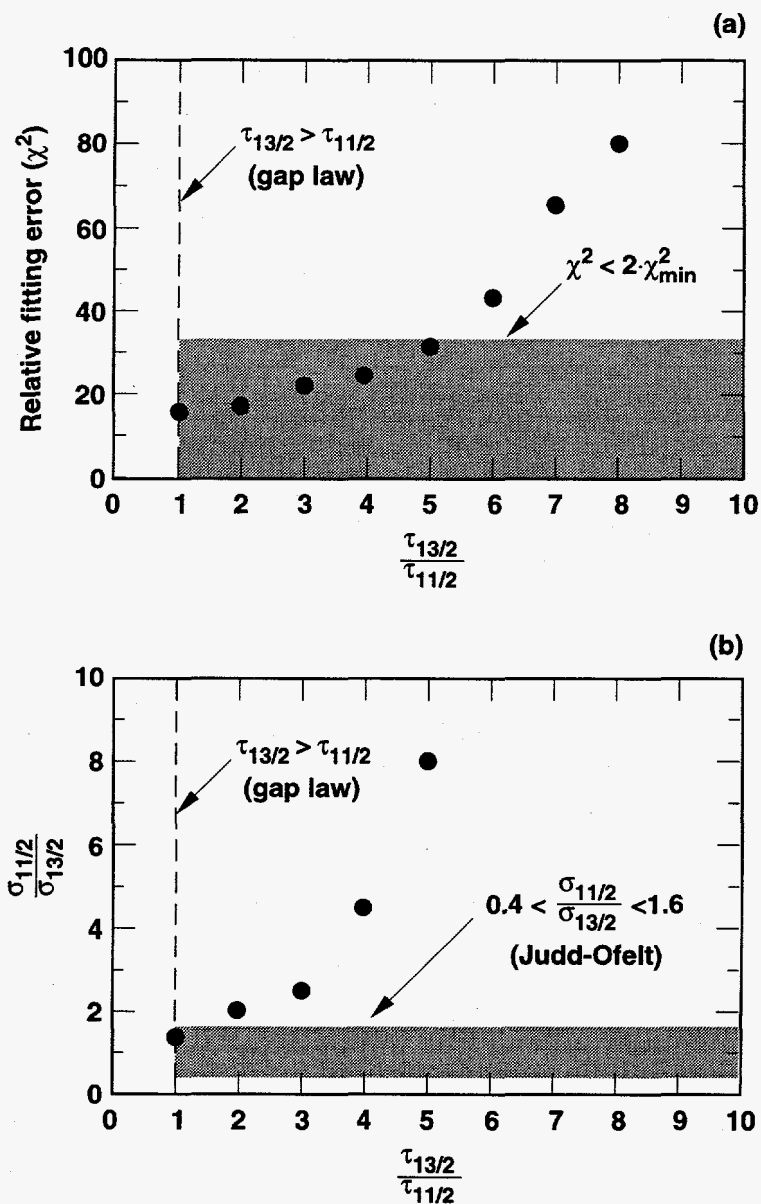


Figure 2.4 (a) A plot of the relative fitting error, χ^2 of LG-750 as a function of the ratio of lifetimes, $\tau_{13/2}/\tau_{11/2}$, and (b) a plot of the ratio of cross sections, $\sigma_{11/2}/\sigma_{13/2}$, as a function of the ratio of lifetimes, $\tau_{13/2}/\tau_{11/2}$. The gray band in (a) is based on the maximum allowable fitting error. The gray band in (b) is based on the factor of two uncertainty in the independent calculation of the ratio cross sections using the Judd-Ofelt analysis. The gap-law theory assumes a decrease in the nonradiative rate with increasing energy gap and therefore, since the ${}^4I_{11/2}-{}^4I_{9/2}$ gap is always $\sim 200 \text{ cm}^{-1}$ smaller than the ${}^4I_{13/2}-{}^4I_{11/2}$ gap, the ratio of lifetimes should be greater than one (vertical dashed line).

Nd:Glass hosts

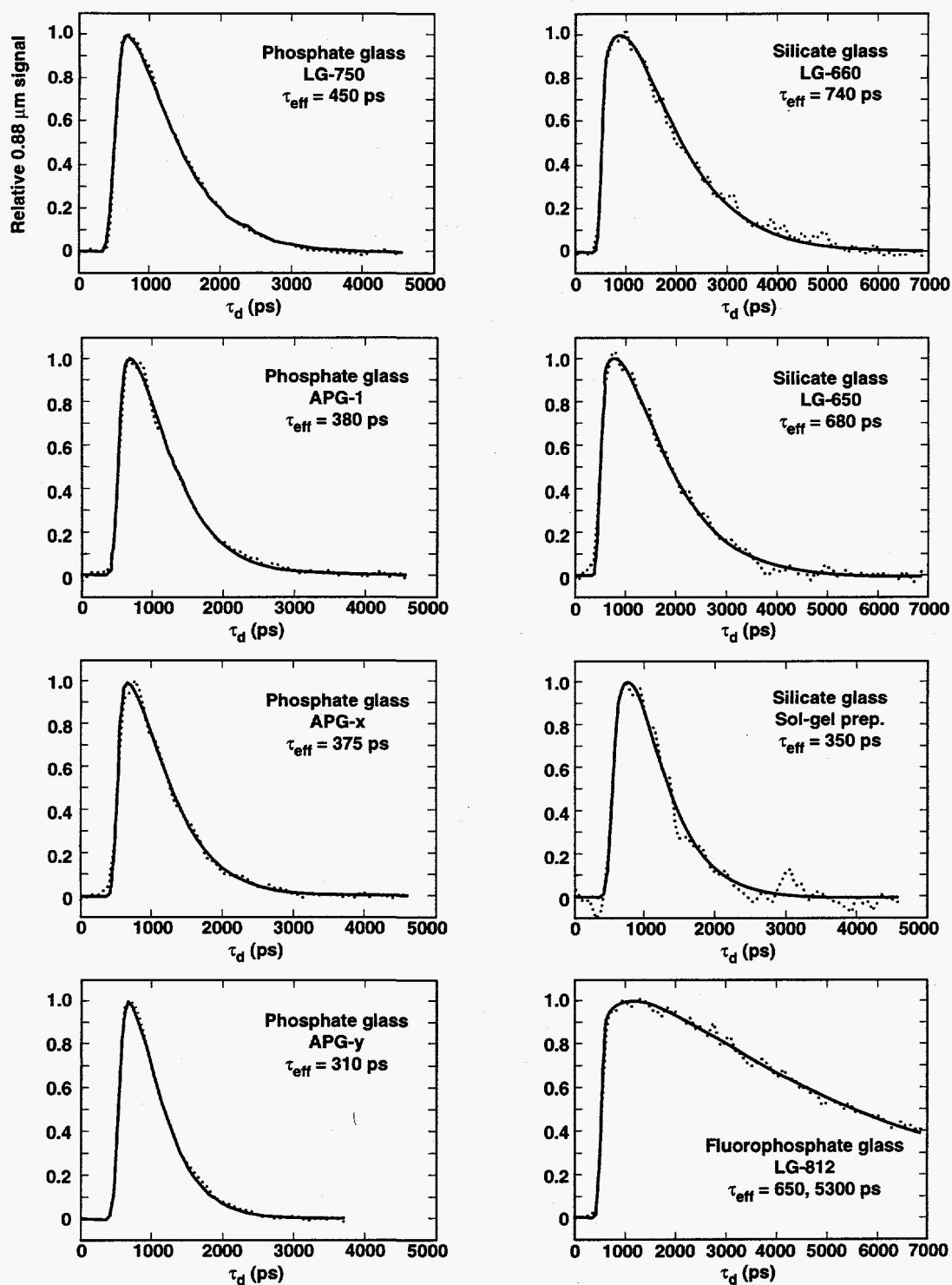


Figure 2.5 The data (\cdots) and model (—) are shown for eight of the glasses investigated. The effective lifetimes corresponding to the averaged energy gap are listed. The higher phonon frequencies of the LG-series phosphates lead to shorter lifetimes compared to the LG-series silicates

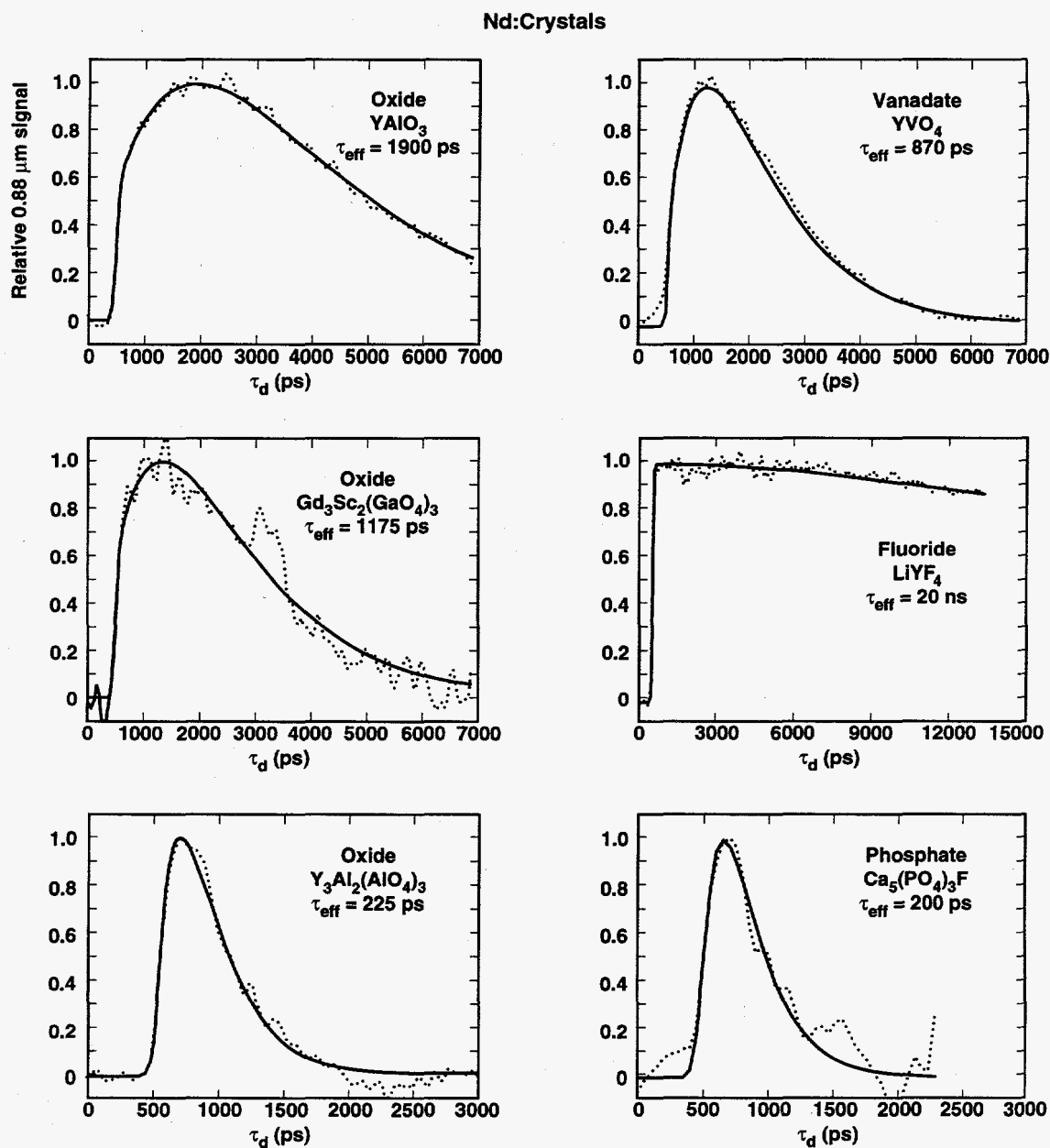


Figure 2.6 The data (...) and model (—) are shown for six of the crystals investigated. The effective lifetimes corresponding to the averaged energy gap are listed. The small energy gaps and high effective phonon frequencies lead to the short lifetimes (~200 ps) measured for the $\text{Y}_3\text{Al}_5\text{O}_{12}$ (YAG) and $\text{Ca}_5(\text{PO}_4)_3\text{F}$ (C-FAP) crystals.

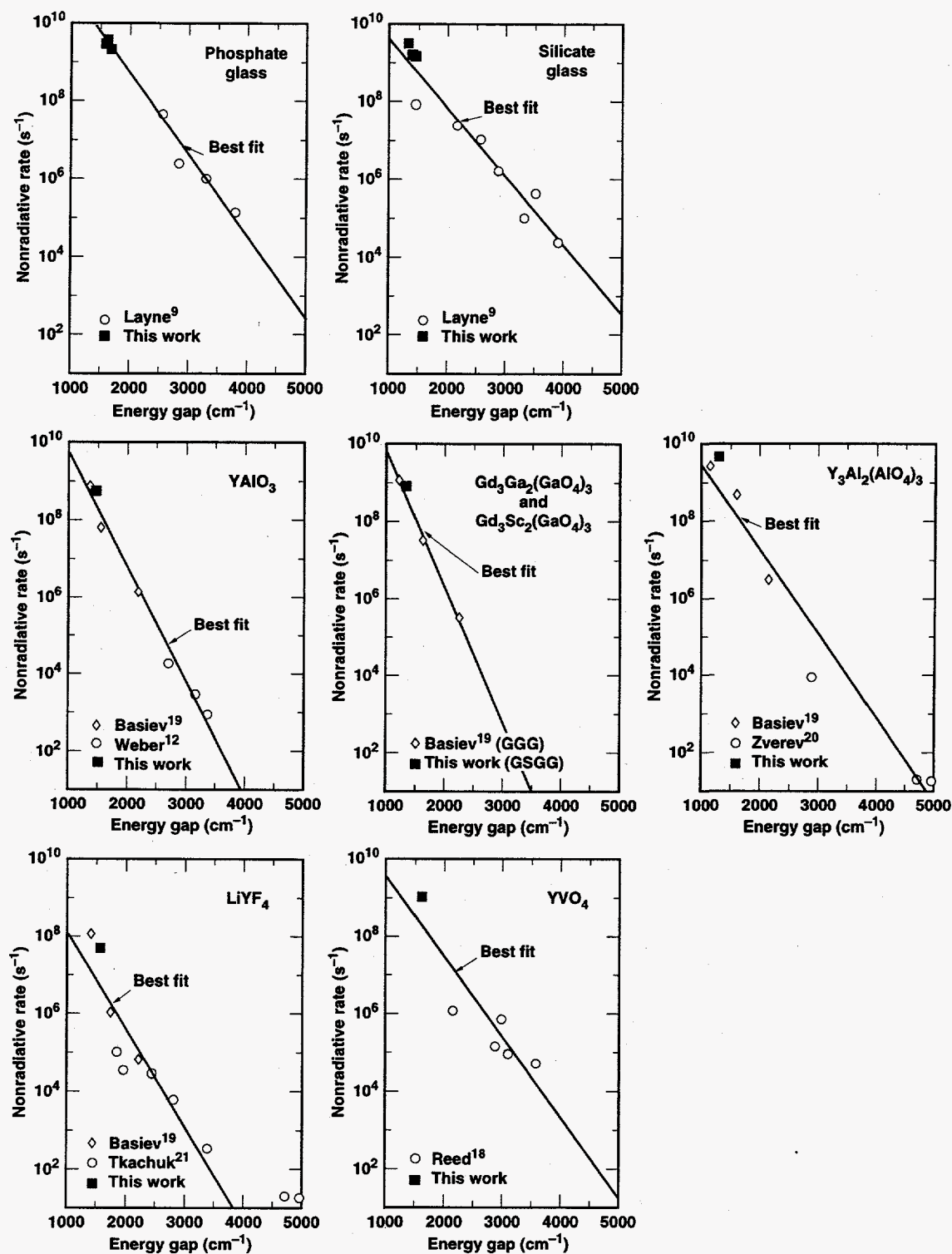


Figure 2.7 Plot of nonradiative rate as a function of energy gap for various Nd-doped crystals and glasses that includes the present work and others along with a best fit line through the data (—).

Chapter 2 References

- ¹G. E. Forsythe, M. A. Malcolm, and C. B. Moler, *Computer Methods for Mathematical Computations*, pg. 129, (Prentice-Hall, Inc., New Jersey, 1977)
- ²B. R. Judd, "Optical absorption intensities of rare-earth ions," *Phys. Rev* **127**, 750 (1962).
- ³G. S. Ofelt, "Intensities of crystal spectra of rare-earth ions," *J. of Chem. Phys.* **37**, 511 (1962).
- ⁴I. M. Thomas, S. A. Payne and G. D. Wilke, "Optical properties and laser demonstration of Nd-doped sol-gel silica glasses," *Journal of Non-Crystalline Solids* **151**, 183 (1992).
- ⁵G. V. Maksimova and A. A. Sobol, "Nd³⁺ Optical centers in crystals of calcium and strontium fluorophosphates," *Proceedings of the P. N. Lebedev Physics Institute* **60**, 59 (1974).
- ⁶K. A. Gschneidner, Jr. and L. Eyring, *Handbook on the Physics and Chemistry of Rare Earths* **5**, Chap. 46, (North-Holland, New York, 1982).
- ⁷J. B. Gruber, M. E. Hills, C. A. Morrison, G. A. Turner, and M. R. Kokta, "Absorption spectra and energy levels of Gd³⁺, Nd³⁺, and Cr³⁺ in the garnet Gd₃Sc₂Ga₃O₁₂," *Phys. Rev. B*, **37**, 8564 (1988).
- ⁸Y. E. Kariss, M. N. Tolstoi, and P. P. Feofilov, "On the luminescence and absorption of trivalent neodymium in crystals of the fluorite type," *Opt. Spectrosc.* **18**, 247 (1965).
- ⁹C. B. Layne, W. H. Lowdermilk, and M. J. Weber, "Multiphonon relaxation of rare-earth ions in oxide glasses," *Phys. Rev. B* **16**, 10 (1977).
- ¹⁰S. R. Levitt, K. C. Blakeslee, and R. A. Condrate, Sr., "Infrared spectra and laser-Raman spectra of several apatites," *Memoires de la Societe Royal des Sciences de Liege* **5**, 121 (1970).
- ¹¹D. Heiman, R. W. Hellwarth, and D. S. Hamilton, "Raman scattering and nonlinear refractive index measurements of optical glasses," *J. Non-Crystalline Solids* **34**, 63 (1979).
- ¹²M. J. Weber, "Multiphonon relaxation of rare-earth ions in yttrium orthoaluminate," *Phys. Rev. B* **8**, 54 (1973).
- ¹³P. Zhang, Y. Liu, and Y. Mo, "The Raman spectrum of single crystal Gd₃Ga₅O₁₂," *Chinese Phys.* **4**, 530 (1984).
- ¹⁴J. P. Hurrell, S. P. S. Porto, I. F. Chang, S. S. Mitra, and R. P. Bauman, "Optical phonons of yttrium aluminum garnet," *Phys. Rev.* **173**, 851 (1968).
- ¹⁵I. Richman, "Vibronic Spectra of SrF₂:Sm²⁺ and BaF₂:Sm²⁺," *Phys. Rev.* **133**, A1364 (1964).
- ¹⁶S. A. Miller, H. E. Rast, and H. H. Caspers, "Lattice Vibrations of LiYF₄," *J. Chem. Phys.* **52**, 4172 (1970).
- ¹⁷E. B. Sveshnikova, A. A. Stroganov, and L. N. Urusovskaya, "Mechanism of nonradiative transitions in rare-earth ions in fluorozirconate bases," *Opt. Spectrosc. (USSR)* **63** (5), 618 (1987).
- ¹⁸E. D. Reed Jr., and H. W. Moos, "Multiphonon relaxation of excited states of rare-earth ions in YVO₄, YAsO₄, and YPO₄," *Phys. Rev. B* **8**, 980 (1973).

-
- ¹⁹T. T. Basiev, A. Y. Dergachev, Y. V. Orlovskii, and A. M. Prokhorov, "Multiphonon nonradiative relaxation from high-lying levels of Nd³⁺ ions in fluoride and oxide laser materials," OSA Proceedings on Advanced Solid-State Lasers **10**, 358 (1991).
- ²⁰G. M. Zverev, G. Ya. Kolodnyi, and A. M. Onishchenko, "Nonradiative transitions between levels of trivalent rare-earth ions in yttrium-aluminum garnet crystals," Sov. Phys. - JETP **33**, 497 (1971).
- ²¹A. M. Tkachuk, A. V. Khilko, and M. V. Petrov, "Probabilities for nonradiative intermultiplet transitions in the holmium ion in lithium-yttrium double fluoride crystals and stimulated emission," Opt. Spectrosc. (USSR), **58** (2), 216 (1985).
- ²²S. M. Yarema and D. Milam, "Gain saturation in phosphate laser glasses," IEEE J. Quantum Electron. **QE-18**, 1941 (1982).
- ²³C. Bibeau, J. B. Trenholme, and S. A. Payne, "Pulse Length and terminal level lifetime dependence of energy extraction for neodymium doped phosphate amplifier glass," Submitted to the IEEE J. of Quantum Electron.
- ²⁴W. E. Martin and D. Milam, "Direct measurement of gain recovery in a saturated Nd-glass amplifier," Appl. Phys. Lett. **32**, 816 (1978).
- ²⁵K. Palombo, S. Matthews, S. Sheldrake, and D. Capps, "Determination of the effective lower level lifetime for Nd:YLF and Nd:YAG through experimental measurement and computer modeling," OSA Proceedings on Advanced Solid-State Lasers **15**, 78 (1993).
- ²⁶W. F. Krupke, "Induced-emission cross sections in neodymium laser glasses," IEEE J. Quantum Electron. **QE-10**, 450 (1974).
- ²⁷W. T. Carnall, H. Crosswhite, and H. M. Crosswhite, *Energy level structure and transition probabilities of the trivalent lanthanides in LaF₃*, (Argonne National Laboratory, Argonne, Ill.).

Chapter 3

Measurements of the nonradiative lifetime ($\tau_{7/2}$) for the ${}^4G_{7/2} \rightarrow {}^4G_{5/2}, {}^2G_{7/2}$ transition in 30 Nd-doped crystals and glasses

3.1 Introduction

In the previous chapter, we presented a new experimental method to measure the temporal evolution of the neodymium population for the ${}^4I_{11/2} \rightarrow {}^4I_{9/2}$ transition in several glasses and crystals. Although this method is more accurate and direct than most other experimental techniques, our pump-probe method utilizes a complex experimental arrangement and requires a detailed numerical analysis of the data to determine the value of the terminal level lifetime. In this chapter, we are primarily interested in investigating a simpler approach for inferring the value of the terminal level lifetime. This simpler, but indirect method, involves measuring the nonradiative lifetime for the ${}^4G_{7/2} \rightarrow {}^4G_{5/2}, {}^2G_{7/2}$ transition, since this particular transition happens to have a similar sized energy gap as the ${}^4I_{11/2} \rightarrow {}^4I_{9/2}$ transition in most Nd-doped materials (**Figure 3.1**). If the energy gap law^{1,2} (discussed in Chapter 1) is assumed to be valid, then the values of the $\tau_{7/2}$ and $\tau_{11/2}$ lifetimes corresponding to these transitions should also be similar, thus allowing one to perform an easier experiment in order to predict the terminal level lifetime.

In the experiment, the neodymium ions are excited from the ground state to the ${}^4G_{7/2}$ level with the frequency doubled output of a 1 μm laser. The resulting emission signal from the ${}^4G_{7/2}$ level provides a direct measure of the $\tau_{7/2}$ lifetime because the decay rate of the emission signal will be largely dominated by the ${}^4G_{7/2} \rightarrow {}^4G_{5/2}, {}^2G_{7/2}$ nonradiative rate ($W_{\text{nr}} = 1/\tau_{7/2}$):

$$W_{\text{signal}} = W_{\text{nr}} + W_{\text{rad}} \approx W_{\text{nr}} \quad \text{since } W_{\text{nr}} \gg W_{\text{rad}} \quad (1)$$

The energy level diagram for the pumping and emission processes are shown in **Figure 3.1**. After exciting the ground state Nd-ions with the 532 nm pump beam, the ~ 600 nm emission signal corresponding to the ${}^4G_{7/2} \rightarrow {}^4I_{11/2}$ transition is recorded. In our experimental setup we chose a technique suitable for measuring time resolved emission spectra characterized by weak signal levels and/or picosecond lifetimes, called time-

correlated single photon counting³. We employed the single-photon counting method for all of the samples investigated except for the fluoride materials. A combination of the high repetition rate of the laser (76 MHz) and the long lifetimes (ns) of the fluoride materials required the use of an alternative technique. We will first discuss the experimental arrangement, data, and results from the photon-counting method followed by a similar discussion for the time resolved emission measurements for the fluoride materials. We will conclude this chapter with a comparison of the results obtained from the indirect photon-counting experiments and the direct pump-probe experiments (Chap. 2). We will show that the results are very similar for most of the materials investigated thus offering validation for an alternative approach to determining the terminal level lifetime. In addition, this comparison implies that the lower limit of τ_{eff} from Chapter 2 is a more appropriate assessment of the ${}^4I_{11/2}$ lifetime.

3.2 Time-correlated single photon counting experimental arrangement

Figure 3.2 illustrates an experimental scheme for measuring the $\tau_{7/2}$ lifetime with a time-correlated single photon counting system. The frequency doubled output of a Coherent mode locked Nd:YAG laser produced 1W of 532 nm light with a ~90 ps pulse width (1/e) and operated at a repetition rate of 76 MHz. The samples were illuminated with 532 nm light and the fluorescence at the ~600 nm wavelength for the ${}^4G_{7/2}$ emission was detected at the output of a monochromator with a multichannel plate photomultiplier-tube (MCP-PMT) from Hamamatsu (Model 1564-07). The electronic signal from the MCP-PMT was amplified with a high bandwidth amplifier from Phillips Scientific (Model 6954 B-100).

In principle, the entire intensity versus time distribution could be recorded for the ${}^4G_{7/2} \rightarrow {}^4I_{11/2}$ transition with a single 532 nm excitation pulse. However, the weak signal levels coupled with the picosecond time scales would place stringent specifications on the time resolution and sensitivity of the detector. We chose to use a method called time-correlated single photon counting. This method uses the high repetition rate of the laser system to build up the emission signal after many excitation pulses. Eventually, the emission signal can be reproduced with very high temporal resolution (a decay resolution

of 3 ps has been reported⁴). This technique is based on the concept that the probability distribution for the emission of a single photon after excitation is also the intensity versus time distribution of all the photons emitted as a result of the excitation. Therefore, by measuring the time at which a single photon emitted for a large number of excitation events allows the experiment to eventually construct the full probability distribution³.

We will next describe the sequence of electronic events. The MCP-PMT is used to monitor the arrival of the first photon emitted after the sample has been excited. From the single photon event, the MCP-PMT is able to generate an electronic signal known as the start pulse. The electronic start pulse is sent into the time-to-amplitude converter (TAC) and initiates the charging of a capacitor. However, since amplitude fluctuations in the start pulse can result in timing jitter, the start pulse is preconditioned by a constant fraction discriminator (CFD, Ortec Model 9307) before it is sent into the TAC. The CFD is able to output a TTL (transistor-transistor logic) signal with a precisely timed leading edge that is independent of the amplitude fluctuations.

The 532 nm pulse from the second path is time delayed and sent into a fast silicon photodetector from Electro-Optics Technology (Model ET-2000). The output from the silicon detector is also sent into the CFD and is used to stop the charging of the capacitor in the TAC. The amount of charge stored on the capacitor is proportional to the time interval (Δt) between the start and stop pulses. The TAC outputs an electronic pulse with an amplitude (A) that is directly proportional to the stored charge on the capacitor and thus Δt . The multichannel buffer (MCB, Ortec model 917) performs an analog to digital conversion of this pulse and increments the count in one of its segmented memory channels. The internal buffer of the MCB is segmented into several channels or storage bins so that the MCB is able keep a running count of the different pulse amplitudes generated from the TAC. The storage bins that have the largest number of counts will correspond to the peak of the fluorescence shape since there is a higher probability of detecting a photon immediately after excitation of the sample. The above sequence of events is repeated until an adequate number of single photon events have been sampled to accurately reconstruct the emission signal.

3.3 Data analysis and results

The data is shown in **Figures 3.3-3.6** where the numerical model of the population kinetics is shown as the overlaid solid curve. In our kinetic model we include the $\tau_{7/2}$ and $\tau_{5/2}$ lifetimes of the ${}^4G_{7/2} \rightarrow {}^4I_{11/2}$ and ${}^4G_{5/2}, {}^2G_{7/2} \rightarrow {}^4I_{9/2}$ transitions respectively, since both transitions give rise to a resonant emission signal at ~ 600 nm (**Figure 3.7**). We will denote the ${}^4G_{5/2}, {}^2G_{7/2}$ level with a single 5/2 subscript throughout the text. The rate equations for the kinetic model are:

$$\frac{dN_{7/2}}{dt} = -\frac{N_{7/2}}{\tau_{7/2}} + N_{9/2}\sigma_o \frac{I_{\text{pump}}}{h\nu_{532}} \quad (2)$$

$$\frac{dN_{5/2}}{dt} = \frac{N_{7/2}}{\tau_{7/2}} - \frac{N_{5/2}}{\tau_{5/2}} \quad (3)$$

where we assume the lower level populations to be virtually unchanged by the pump beam:

$$N_{11/2} \cong \text{constant} \quad (4)$$

and
$$N_{9/2} \cong \text{constant} \quad (5)$$

The recorded signal will be directly proportional to the cross section of the transition (σ) multiplied by the solutions for the population densities (N) from the equations above:

$$I_{\text{signal}} \propto (\sigma_{7/2}N_{7/2} + \sigma_{5/2}N_{5/2}) \quad (6)$$

or
$$\propto \left(N_{7/2} + \frac{\sigma_{5/2}}{\sigma_{7/2}} N_{5/2} \right) \quad (7)$$

The ratio of cross sections ($\sigma_{5/2}/\sigma_{7/2}$) is estimated from the of the Judd-Ofelt analysis described in Appendix 3A at the end of this chapter. We were able to record the temporal shape of the pump beam by allowing a small amount of light to pass through the monochromator and into the MCP-PMT. The recorded shape was fit to an asymmetric Gaussian as shown in **Figure 3.8** and substituted into I_{pump} in Eqn. 2.

The nonradiative lifetimes ($\tau_{7/2}$ and $\tau_{5/2}$) derived from the kinetic analysis, the corresponding energy gaps, $\Delta E_{7/2}$ and $\Delta E_{5/2}$, the calculated ratio of cross sections ($\sigma_{5/2}/\sigma_{7/2}$), and the effective or highest phonon frequencies are all listed in **Table 3.1**. Based on an analysis of the best fit to the data, the uncertainty in the value of the $\tau_{7/2}$

lifetimes is $\Delta\tau_{7/2} (<1 \text{ ns}) = \pm 50 \text{ ps}$ for data with lifetimes less than 1 ns and $\Delta\tau_{7/2} (>1 \text{ ns}) = \pm 200 \text{ ps}$ for data with lifetimes greater than 1 ns. We also list the $\tau_{5/2}$ lifetimes for completeness. However, these lifetimes are known with less certainty, since for some of the materials, the $\tau_{5/2}$ lifetimes were less than the width of the pump pulse thus making an accurate evaluation difficult. Therefore, we choose to emphasize the results of the $\tau_{7/2}$ lifetimes.

In comparing the values of the $\tau_{7/2}$ lifetimes among the various materials investigated we found that the phosphate and silicate glasses both exhibit very short lifetimes ($\sim 200 \text{ ps}$) due to the high phonon frequencies present in the host materials ($1000\text{--}1100 \text{ cm}^{-1}$). However, the fluorophosphate glass, LG-812, was shown to have a combination of a shorter lifetime ($<1 \text{ ns}$) and a longer lifetime ($>1 \text{ ns}$) present in the emission signal. As a consequence, we were not able to fit the data to the kinetic model described in Eqn. 7 and so only the raw data is plotted. Because of the mixed glass composition, the Nd ion is surrounded by both high frequency phosphate complexes and low frequency fluoride complexes which could explain the presence of the two different decay rates. And therefore, an alternative physical model is needed to properly analyze the data.

Within the group of oxide crystals, (which includes two additional materials beyond those studied in Chapter 2: GGG ($\text{Gd}_3\text{Ga}_5\text{O}_{12}$) and LLGG ($\text{La}_3\text{Lu}_2\text{Ga}_3\text{O}_{12}$), we found that YAG still exhibits the shortest lifetime due to the small energy gap and high phonon frequencies. In addition, we found that several of our oxide data agree to within a factor of two with the results recently obtained from Basiev et al.⁵ using a similar technique where they reported 370 ps for YAG, 1400 ps for YALO, and 880 ps for GGG compared to our results of 200 ps, 1090 ps and 530 ps respectively (chemical formulae are $\text{Y}_3\text{Al}_5\text{O}_{12}$, YAlO_3 , and $\text{Gd}_3\text{Ga}_5\text{O}_{12}$ respectively). A possible explanation for the differences in the results could arise from the inclusion of the $\tau_{5/2}$ lifetime in our data analysis to account for the resonant emission signal. We also investigated a tungstate (CaWO_4) whose lifetime of 510 ps was similar to the lifetime reported (550 ps) for the structurally related compound CaMoO_4 by Basiev et al.⁵ It is interesting to note that both

materials have similar energy gaps and effective phonon frequencies thus giving rise to similar values of $p \cong 1.6$. (Recall from Chapter 1 that the nonradiative rate is exponentially dependent on the order of the process, $p = \Delta E_{\text{gap}}/h\nu_{\text{eff}}$). We also looked at a series of apatites of which C-FAP, exhibited the shortest nonradiative lifetime (70 ps) measured and reported in the literature thus far. We found that within the group of apatites, the fluorophosphates: C-FAP ($\text{Ca}_5(\text{PO}_4)_3\text{F}$) and S-FAP ($\text{Sr}_5(\text{PO}_4)_3\text{F}$) exhibited shorter lifetimes than the fluorovanadates: S-VAP ($\text{Sr}_5(\text{VO}_4)_3\text{F}$) and C-VAP ($\text{Ca}_5(\text{VO}_4)_3\text{F}$) and the chlorovanadate, $\text{Sr}(\text{VO}_4)_3\text{Cl}$, possibly due to the higher phonon frequencies found in the PO_4 phosphate complexes compared to the VO_4 complexes. However, we note that within the group of fluoro- and chloro-vanadates studied, C-VAP ($\text{Ca}_5(\text{VO}_4)_3\text{F}$) has a significantly shorter lifetime than both S-VAP ($\text{Sr}_5(\text{VO}_4)_3\text{F}$), and $\text{Sr}(\text{VO}_4)_3\text{Cl}$, indicating that the crystal-field coupling could be stronger between the Nd ion and the C-VAP host which would allow the nonradiative transfer of energy (Nd→host) to occur at a faster rate. The doping levels for the crystalline materials investigated roughly ranged from 0.1-2% whereas for the glasses, the concentrations ranged from ~2-5 weight %.

In addition to measuring the $\tau_{7/2}$ lifetime for a number of materials, we also measured the temperature dependence of the $\tau_{7/2}$ lifetime in two glasses: LG-750 and LG-812 (**Figure 3.9**). The measured $\tau_{7/2}$ lifetime for LG-750 at room temperature was found to be 228 ps and did not significantly change when the temperature was decreased from room temperature to 18.3 K (200 ps). The apparent shortening of the $\tau_{7/2}$ lifetime between 295 K and 18.3 K indicates that the lowest Stark level, on average, has a predominately shorter lifetime than the nonradiative transitions originating from the higher lying Stark levels. Previous temperature dependent measurements of the nonradiative lifetimes for Er and Ho:YAsO₄ and Ho:YVO₄ have also shown a similar temperature dependence. The data was modeled by modifying the energy gap law expression to include the thermal populations of the Stark levels and allowing the possibility of phonons of different energies be used in the model.⁶

For the fluorophosphate glass, LG-812, we found that as the temperature was lowered to 18.3 K, the lifetime of the emission signal became significantly shorter. In fact, the low temperature data exhibited an exponential decay lifetime (230 ps) very similar to that of LG-750 (200 ps). The model is shown as the solid curve in **Figure 3.9**. One possible explanation of this observation is that as the temperature is lowered, the energy levels of the medium are shifted in such a way that the pump beam no longer excites the Nd ions surrounded largely by fluoride anions but instead predominately excites the higher frequency phosphate complexes thus giving rise to the faster decay rate.

During our attempts to measure the $\tau_{7/2}$ lifetime for the fluoride materials using the photon counting technique, we found that the longer lifetimes (nanoseconds) and the high repetition rate of the laser (13 ns window between pulses) prevented us from accurately measuring the decay signals. This is because the emission signal does not completely decay to zero before the next excitation pulse arrives, so that photons which were emitted from the initial excitation can act as a false start signal for the following excitation. In order to operate the photon counting system properly, it is important that the start and stop pulses originate from the *same* laser pulse. Because we were not able to reduce the repetition rate of our laser system, we designed an alternative experiment for the fluoride materials.

3.4 Time resolved emission measurements (fluoride materials)

The nanosecond time-scale experimental scheme is shown in **Figure 3.10**. A JK Q-switched Nd:YAG laser (Model HY-750) operating at 10 Hz was frequency doubled to produce output pulses of ~500 mJ at 532 nanometers. The light was focused into the sample with a 35 cm focus lens. The ~600 nm emission was collected at the side of the sample with a 2.5 cm diameters lens with a focal length of 5 cm. The image was then magnified and relayed to the monochromator (Digikrom 240) slit entrance with a 10 cm lens to match the f/4 optical system with the monochromator. Depending on the signal level, the slit width ranged from ~100-200 μm . A narrowband filter (Melles Griot 03F1V046) was placed at the slit entrance to block out unwanted frequencies and a MCP-PMT (Hamamatsu 1564-07) detector was placed at the output of the monochromator

(similar to the detector used in **Figure 3.2**). A LeCroy oscilloscope (Model 9306) was used to capture the entire emission signal after one excitation pulse. However, since the emission signal levels were very low (1-20 mV at the peak), we chose to average 10,000 emission signals for each sample. The LeCroy oscilloscope has a built-in option that allows the incoming signals to be internally stored and averaged before the data is transferred onto a storage disk.

3.5 Data analysis and results

The data for the fluoride glass and crystals are shown in **Figures 3.11 and 3.12**. The numerical model is shown as the solid line and the data is shown with open circles. The kinetic population rate equation used to model the data includes information about the $\tau_{7/2}$ lifetime only, since the long length of the pump pulse width (~12 ns FWHM) did not allow us to deconvolve the $\tau_{5/2}$ lifetime from the data. The equation used for the analysis is simply:

$$\frac{dN_{7/2}}{dt} = -\frac{N_{7/2}}{\tau_{7/2}} + N_{9/2}\sigma_0 \frac{I_{\text{pump}}}{h\nu_{532}} \quad (8)$$

where we assume that the lower level population remains approximately constant:

$$N_{9/2} \equiv \text{constant} \quad (9)$$

The temporal shape of the pump pulse was recorded (**Figure 3.13**) by allowing a small amount of light to pass through the monochromator (20 μm slit width) and into the detector. Because of the irregular shape, we used the actual data as the pump shape, I_{pump} , within the numerical model. The $\tau_{7/2}$ lifetimes are listed in **Table 3.2**. Based on an analysis of the best fit to the data, the uncertainty in the value of the lifetimes is $\Delta\tau_{7/2}$ (<10 ns) = ± 1 ns for data with lifetimes less than 10 ns and $\Delta\tau_{7/2} = \pm 2$ ns for the ZBLAN and YF_3 data. All of the data exhibited a single exponential decay with the exception of LaF_3 where the data could only be fit to a two Nd-ion site model. Two uncoupled rate equations were used to model the data:

$$\frac{dN_{7/2}^{\text{site1}}}{dt} = -\frac{N_{7/2}^{\text{site1}}}{\tau_{7/2}^1} + N_{9/2}\sigma_1 \frac{I_{\text{pump}}^{\text{site1}}}{h\nu_{532}} \quad (10)$$

$$\frac{dN_{7/2}^{\text{site2}}}{dt} = -\frac{N_{7/2}^{\text{site2}}}{\tau_{7/2}^2} + N_{9/2}\sigma_2 \frac{I_{\text{pump}}^{\text{site2}}}{h\nu_{532}} \quad (11)$$

The resulting emission signal would then include information about both of the Nd environments:

$$I_{\text{signal}} = N_{7/2}^{\text{site1}} + \gamma N_{7/2}^{\text{site2}} \quad (12)$$

The best fit to the data yielded $\tau_{7/2} = 41$ ns for site 1, $\tau_{7/2} = 3$ ns for site 2, and $\gamma = 8$. The uncertainty in the lifetimes derived from this model are approximately $\pm 50\%$ since the exact value of the “ γ ” parameter is unknown. The value of the parameter γ , indicates that the emission from the second environment is eight times stronger than the first. The room temperature lifetime measured by Basiev et al.⁵ for LaF₃ was $\tau_{7/2} = 56.4$ ns. Although the publication did not report a nonexponential decay for LaF₃ it is possible that the relatively fast decay of the second site (3 ns) was not time resolved since the length of the excitation pulses used were over three times as long (10 ns). However, they did observe two different exponential decay rates in CaF₂ and SrF₂ at 77 K and attributed the observation to two or more environments surrounding the Nd ion. Finally the results from the same publication yielded $\tau_{7/2} = 8.4$ ns for YLF at room temperature compared to our value of 9.1 ns. The effective phonon frequencies ($h\nu_{\text{eff}}$) are also listed in **Table 3.2** and appear to be 1.5-2 times smaller than those listed in **Table 3.1** and therefore, as predicted from the energy gap law, the data for the fluoride materials exhibit longer lifetimes since the number of phonons needed to bridge the energy gap is greater.

3.6 Comparison of the pump-probe and emission methods and best assessment of the terminal level lifetime for 15 Nd-doped crystals and glasses

We have just described two independent experiments for measuring the $\tau_{7/2}$ lifetime in a number of Nd-doped materials. In the introduction we stated that the purpose of measuring the $\tau_{7/2}$ lifetime was to eventually compare its value with the terminal level lifetime ($\tau_{11/2}$) obtained from the direct pump-probe experiments described in Chapter 2 and explore whether the methods discussed above for measuring the $\tau_{7/2}$ lifetime are

sufficiently accurate for inferring the $\tau_{11/2}$ lifetime of most Nd-doped laser materials. Recall from the introduction that the ${}^4G_{7/2} \rightarrow {}^4G_{5/2}, {}^2G_{7/2}$ energy gap is nearly the same as the ${}^4I_{11/2} \rightarrow {}^4I_{9/2}$ gap, and is therefore expected to experience a similar relaxation time. The lifetime data for thirteen different Nd-doped laser materials taken from the pump-probe (Chapter 2) and the emission experiments discussed in this chapter are listed in **Table 3.3**. In **Figure 3.14** the lower limit of the direct pump-probe data is plotted against the lifetime from the indirect emission method. A line representing the best fit to the data of the form $y = mx$ is shown. Ideally if both methods yielded the same results then the slope, m , would be equal to one. However, the best fit produced a slope of 1.15 which suggests that the simpler indirect method can be used to determine the terminal level lifetime within a factor of two provided that the excitation pulses are short enough and the detectors and electronics have the required sensitivity and resolution. It is important to note that the plot of **Figure 3.14** implies that the lower limit of the pump-probe data more closely represents the actual $\tau_{11/2}$ lifetime. We call additional support for this assessment in Chapter 6 where we determine $\tau_{11/2}$, from a third independent measurement for the phosphate glass LG-750.

The rightmost column of **Table 3.3** lists our best assessment of the terminal level lifetime from the two approaches. In comparing the lifetimes of the various groups of materials we find that the phosphate glasses have a factor of two shorter lifetime than the silicate glasses. This is primarily due to the high phonon frequencies of the network forming PO_4 complexes in the phosphate host, compared to the relatively lower phonon frequencies of the SiO_4 complexes in the silicate glasses. The shortest lifetime measured was from the phosphate crystal, C-FAP. This material has both high phonon frequencies and a small energy gap. Within the oxide crystals, we find that Nd:YAG has the shortest lifetime and correspondingly the smallest energy gap. And finally as expected, we find that for the fluoride materials, including Nd:YLF, the relatively low 300-600 cm^{-1} phonon frequencies give rise to slower (nanosecond) lifetimes.

3.7 Conclusion

We measured the $\tau_{7/2}$ lifetime for the ${}^4G_{7/2} \rightarrow {}^4G_{5/2}, {}^2G_{7/2}$ transition in 30 Nd-doped materials using a time-correlated single photon counting method and a time resolved fluorescence measurement. We then compared the $\tau_{7/2}$ lifetime with the terminal level lifetime data ($\tau_{11/2}$) described in Chapter 2. This comparison was made since the energy gap of the ${}^4G_{7/2} \rightarrow {}^4G_{5/2}, {}^2G_{7/2}$ transition is similar to the ${}^4I_{11/2} \rightarrow {}^4I_{9/2}$ transition and therefore the measured lifetimes should also be similar based on the form of the energy gap law. We found that the $\tau_{7/2}$ lifetime was within a factor of two of the terminal level lifetime ($\tau_{11/2}$) for the ${}^4I_{11/2} \rightarrow {}^4I_{9/2}$ transition for most Nd-doped materials. Based on the best data of the two measurements we listed our best assessment of the terminal level lifetime for 15 Nd-doped materials. In addition, we measured the temperature dependence of the phosphate glass, LG-750, (a glass used in the Nova amplifiers and similar to a glass proposed for the National Ignition Facility), and found the $\tau_{7/2}$ lifetime to only weakly depend on the temperature. However, the lifetime for the fluorophosphate glass, LG-812, significantly changed and approached the value of the phosphate glass at low temperatures.

Appendix 3A

The emission cross sections for the ${}^4G_{7/2} \rightarrow {}^4I_{11/2}$ and ${}^4G_{5/2}, {}^2G_{7/2} \rightarrow {}^4I_{9/2}$ transitions were calculated using the Judd⁷ and Ofelt⁸ method of absorption intensity analysis for rare-earth ions. The following derivation is similar to that described in the Appendix 2A of Chapter 2. Recall that the expression utilized for the absorption cross section calculation can be written as⁹:

$$\sigma = \frac{8 \pi^3 e^2 \lambda (n^2 + 2)^2 S(aJ:bJ')}{27 c h n (2J + 1) \Delta\lambda_{\text{eff}}} \quad (\text{A1})$$

where $(2J+1)$ is the degeneracy of the initial state (aJ) , $\Delta\lambda_{\text{eff}}$ is the effective linewidth of the transition, λ is the average wavelength of the transition, e , c , and h , are fundamental physical constants, and n is the index of refraction at wavelength λ . The linestrength can be written as a sum of products in the form:

$$S(aJ:bJ') = \sum_{t=2,4,6} \Omega_t \times \langle aJ \| U^{(t)} \| bJ' \rangle^2 \quad (\text{A2})$$

where the matrix elements $\langle U^{(t)} \rangle$ represent the doubly reduced unit tensors operating between the intermediate-coupled eigenstates (aJ) and (bJ') of the free ion. The intensity parameters, Ω_t , will vary depending on the local environment and therefore they must be experimentally determined for each host from a least squares fit of the measured and calculated integrated absorption band strengths.

Recalling that in the high temperature limit, $\sigma_u = g_\ell/g_u \sigma_\ell$, where g_u and g_ℓ is the degeneracy of the upper and lower levels respectively, we can use Eqns. A1 and A2, to derive the emission cross section for the ${}^4G_{7/2} \rightarrow {}^4I_{11/2}$ transition, which can be written as:

$$\sigma_{7/2} = \left(\frac{8 \pi^3 e^2 \lambda (n^2 + 2)^2}{27 c h n \Delta\lambda_{\text{eff}}} \right) \frac{S({}^4G_{7/2}:{}^4I_{11/2})}{8} \quad (\text{A3})$$

However, for the ${}^4G_{5/2}, {}^2G_{7/2} \rightarrow {}^4I_{9/2}$ transition, since the initial state is a combination of two states, we take a linear combination of the linestrengths as follows:

$$\sigma_{5/2} = \left(\frac{8 \pi^3 e^2 \lambda (n^2 + 2)^2}{27 c h n \Delta\lambda_{\text{eff}}} \right) \left(f_1 \frac{S({}^4G_{5/2}:{}^4I_{9/2})}{6} + f_2 \frac{S({}^2G_{7/2}:{}^4I_{9/2})}{8} \right) \quad (\text{A4})$$

where f_1 and f_2 are the fractional occupation numbers of the electronic levels in the high temperature limit and defined in terms of the degeneracy (g) of the levels.

$$f_1 = \frac{g(^4G_{5/2})}{g(^4G_{5/2}) + g(^2G_{7/2})} \quad (\text{A5})$$

and

$$f_2 = \frac{g(^2G_{7/2})}{g(^4G_{5/2}) + g(^2G_{7/2})} \quad (\text{A6})$$

where for simplicity we enumerate the total cross section with a 5/2 subscript. The linestrengths used in the calculation are:

$$S(^4G_{7/2}:^4I_{11/2}) = 0.6684 \times \Omega_2 + 0.1075 \times \Omega_4 + 0.0099 \times \Omega_6 \quad (^4G_{7/2} \rightarrow ^4I_{11/2}) \quad (\text{A7})$$

$$S(^4G_{5/2}:^4I_{9/2}) = 0.8975 \times \Omega_2 + 0.4126 \times \Omega_4 + 0.0346 \times \Omega_6 \quad (^4G_{5/2} \rightarrow ^4I_{9/2}) \quad (\text{A8})$$

$$S(^2G_{7/2}:^4I_{9/2}) = 0.0707 \times \Omega_2 + 0.1720 \times \Omega_4 + 0.0274 \times \Omega_6 \quad (^2G_{7/2} \rightarrow ^4I_{9/2}) \quad (\text{A9})$$

where the $\langle U^{(l)} \rangle$ elements in A7-A9 were obtained from Ref. 10 for the neodymium ion. The intensity parameters Ω_i are host dependent and will vary for each medium. We assume that the effective linewidths employed by Eqns. A3 and A4 are assumed to be similar and thus cancel out when the ratio of the cross sections, $\sigma_{5/2}/\sigma_{7/2}$, is taken (Eqn. 7).

Table 3.1 List of $\tau_{7/5}$ and $\tau_{5/2}$ lifetimes of oxides measured from the photon-counting experiment.

Material	Formula	$\tau_{7/2}$ lifetime (ps)	$\Delta E_{7/2}$ (cm ⁻¹)	$\tau_{5/2}$ ^a lifetime (ps)	$\Delta E_{5/2}$ (cm ⁻¹)	$\sigma_{5/2}/\sigma_{7/2}$ ^b	$h\nu_{\text{eff}}$ (cm ⁻¹)
Phosphate glasses							
LG-750	P ₂ O ₅ -Al ₂ O ₃ +...	228	~1442	40	-	1.19	1100 ²
APG-1	P ₂ O ₅ -Al ₂ O ₃ +...	215	~1442 ^c	30	-	1.23	1100 ²
APG-x	P ₂ O ₅ -Al ₂ O ₃ +...	210	~1442 ^c	30	-	1.07	1100 ²
APG-y	P ₂ O ₅ -Al ₂ O ₃ +...	150	~1442 ^c	30	-	1.08	1100 ²
Silicate glasses							
LG-660	SiO ₂ -K ₂ O+...	215	~1090	25	-	1.12	1000 ²
LG-650	SiO ₂ -K ₂ O+...	210	~1090 ^d	10	-	1.04	1000 ²
Sol-gel	SiO ₂ -Al ₂ O ₃	245	-	50	-	0.999	1200 ¹¹
Vanadate	YVO ₄	190	1504 ¹²	125	1117 ¹²	1.09 ¹³	943 ¹⁴
Tungstate	CaWO ₄	510	1467 ¹²	260	948 ¹²	~1.32 ^e	912 ¹⁵
Oxides							
YALO	YAlO ₃	1090	1392 ¹²	130	868 ¹²	1.77 ¹⁶	750 ¹⁷
GSGG	Gd ₃ Sc ₂ Ga ₃ O ₁₂	715	1211 ¹⁸	215	800 ¹⁸	2.11 ¹³	742 ^g
YAG	Y ₃ Al ₅ O ₁₂	200	1148 ¹²	55	730 ¹²	2.14 ¹⁹	860 ²⁰
GGG	Gd ₃ Ga ₅ O ₁₂	530	1217 ²¹	100	879 ²¹	3.15 ²²	742 ²³
LLGG	La ₃ Lu ₂ Ga ₃ O ₁₂	1200	1239 ²⁴	240	822 ²⁴	1.94 ²⁴	-
Apatites							
C-FAP	Ca ₅ (PO ₄) ₃ F	70	1141 ²⁵	10	715 ²⁵	~1 ²⁵	1080 ²⁶
S-FAP	Sr ₅ (PO ₄) ₃ F	175	1081 ²⁵	20	741 ²⁵	~1 ²⁵	-
C-VAP	Ca ₅ (VO ₄) ₃ F	200	-	60	-	~1 ^f	-
S-VAP	Sr ₅ (VO ₄) ₃ F	330	1224 ^{h,27}	20	-	1.05 ²⁸	-
Sr ₅ (VO ₄) ₃ Cl	Sr ₅ (VO ₄) ₃ Cl	380	-	200	-	~1 ^f	-

(a) $\tau_{5/2}$ lifetime is inferred from numerical analysis.

(b) The ratio of cross sections ($\sigma_{5/2}/\sigma_{7/2}$) is calculated from a Judd-Ofelt analysis, whereas the $\tau_{7/2}$ and $\tau_{5/2}$ lifetimes are determined from a best fit to the data.

(c) Energy gap is assumed to be similar to the measured gap of LG-750.

(d) Energy gap is assumed to be similar to the measured gap of LG-660.

(e) Ratio of cross sections estimated from YLF data.

(f) Ratio of cross sections estimated from S-VAP data.

(g) Effective phonon frequency estimated from GGG data.

(h) ${}^4I_{11/2}-{}^4I_{9/2}$ energy gap is listed since data for the ${}^4G_{7/2}-{}^4G_{5/2}, {}^2G_{7/2}$ energy gap could not be found.

Table 3.2 List of the $\tau_{7/2}$ lifetimes of fluorides from the emission experiments in addition to the corresponding energy gaps ($\Delta E_{7/2}$) and effective phonon frequencies ($h\nu_{\text{eff}}$) if known.

Material	$\tau_{7/2}$ lifetime (ns)	$\Delta E_{7/2}$ (cm^{-1})	$h\nu_{\text{eff}}$ (cm^{-1})
Fluoride glass ZBLAN ($\text{Zr}_4\text{-BaF}_2\text{-AlF}_3\text{-LaF}_3\text{-NaF}$)	18	-	580 ²⁹
Fluoride crystals LiYF ₄	9.1	1381 ¹²	560 ³⁰
Na ₃ Sc ₂ Li ₃ F ₁₂	4	-	-
KY ₃ F ₁₀	9	(1659) ^b	-
YF ₃	22	(1556) ^b	-
SrF ₂	7	1530 ⁵	360 ³¹
BaF ₂	3.8	-	321 ³¹
SrBaF ₂	4.2	-	-
CaF ₂	6.2	(1061-) (1233) ^{b,c}	525 ⁵
LaF ₃	41,(3) ^a	1542 ¹²	414 ³²

- (a) A two Nd-ion site description was necessary to model the nonexponential decay found in LaF₃. The longer lifetime is consistent with measurements made in Ref. 5.
- (b) ${}^4I_{11/2}\text{-}{}^4I_{9/2}$ energy gap is listed since data for the ${}^4G_{7/2}\text{-}{}^4G_{5/2}$, ${}^2G_{7/2}$ energy gap could not be found.
- (c) First value is for the Type II site symmetry, second value is for the Type I site symmetry.

Table 3.3 Results from the direct, pump-probe measurements and the indirect, emission measurements. The right most column lists our best assessment of the terminal level lifetimes.

Material	lifetime $\tau_{11/2}$ (ps)	lifetime $\tau_{7/2}$ (ps)	Best assessment of terminal level lifetime (ps)
Phosphate glasses			
LG-750	250-450	228	250 ^a
APG-1	192-380	215	192 ^a
APG-x	200-375	210	200 ^a
APG-y	158-310	150	158 ^a
Phosphate crystal			
C-FAP	(156-200)	70	70 ^b
Silicate glasses			
LG-660	535-740	215	535 ^c
LG-650	510-689	210	510 ^c
SOL-GEL	247-350	245	247 ^a
Oxides			
YAG	115-225	200	200 ^b
YALO	896-1900	1090	1090 ^b
GSGG	(401-1175)	715	715 ^b
Vanadate			
YVO ₄	531-870	190	531 ^d
Fluorides			
YLF	10.5-20 ns	9.1 ns	9.1 ns ^b
SrF ₂	>5 ns	7 ns	7 ns ^b
Fluoride glass			
ZBLAN	>5 ns	18 ns	18 ns ^b

- (a) Lower limit of the lifetime from the direct method agrees with the lifetime measured from the indirect method.
- (b) Indirect method is preferred since the data is more accurate.
- (c) Energy gap relevant to $^4I_{11/2}$ and $^4G_{7/2}$ states are anomalously different so the $\tau_{11/2}$ and $\tau_{7/2}$ lifetimes do not agree.
- (d) Basis for difference between the $\tau_{11/2}$ and $\tau_{7/2}$ lifetimes is uncertain.

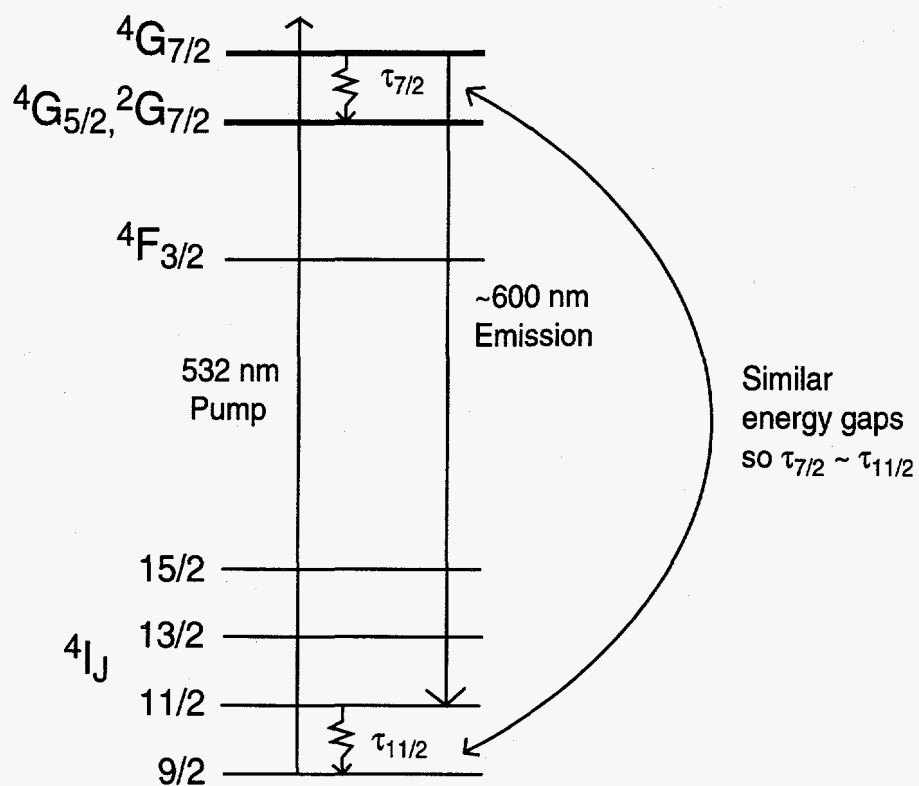


Figure 3.1 An energy level diagram for the emission experiment. A 532 nm pump beam transfers a fraction of the ground state population into the $4G_{7/2}$ level. The resulting emission from the $4G_{7/2}$ level is recorded at the 600 nm wavelength. Since the nonradiative decay for the $4G_{7/2} \rightarrow 4G_{5/2}, 2G_{7/2}$ transition will be much faster than the radiative decay rate, the 600 nm emission signal will be a direct measure the $\tau_{7/2}$ lifetime.

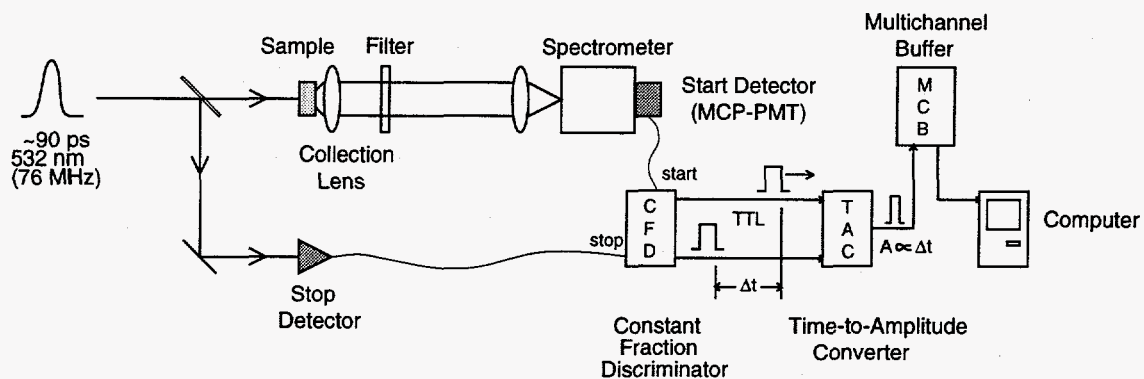


Figure 3.2 An experimental scheme for the indirect emission experiment utilizing a time-correlated photon counting technique. The 532 nm pulse is split into two beams. One beam illuminates the sample and the resulting 600 nm emission is detected with a multichannel plate detector (MCP-PMT). The beam from the second path is time delayed and focused onto a silicon detector. The photon counting electronics (CFD, TAC, MCB) condition the electronic pulses from the two detectors. After multiple excitation pulses the 600 nm emission waveform is reconstructed.

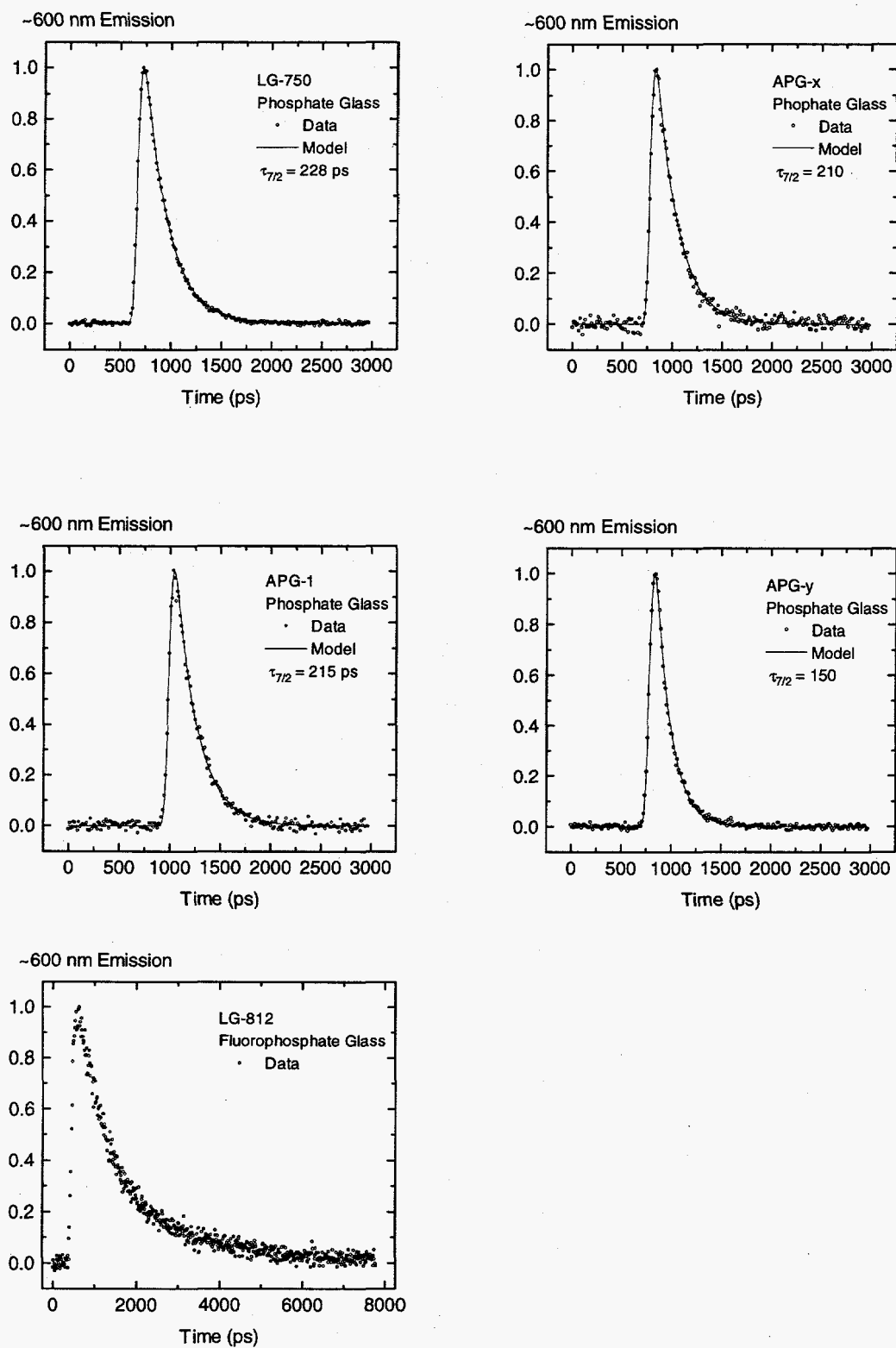


Figure 3.3 Data and numerical fits from single-photon counting experiments for Nd-doped phosphate glasses.

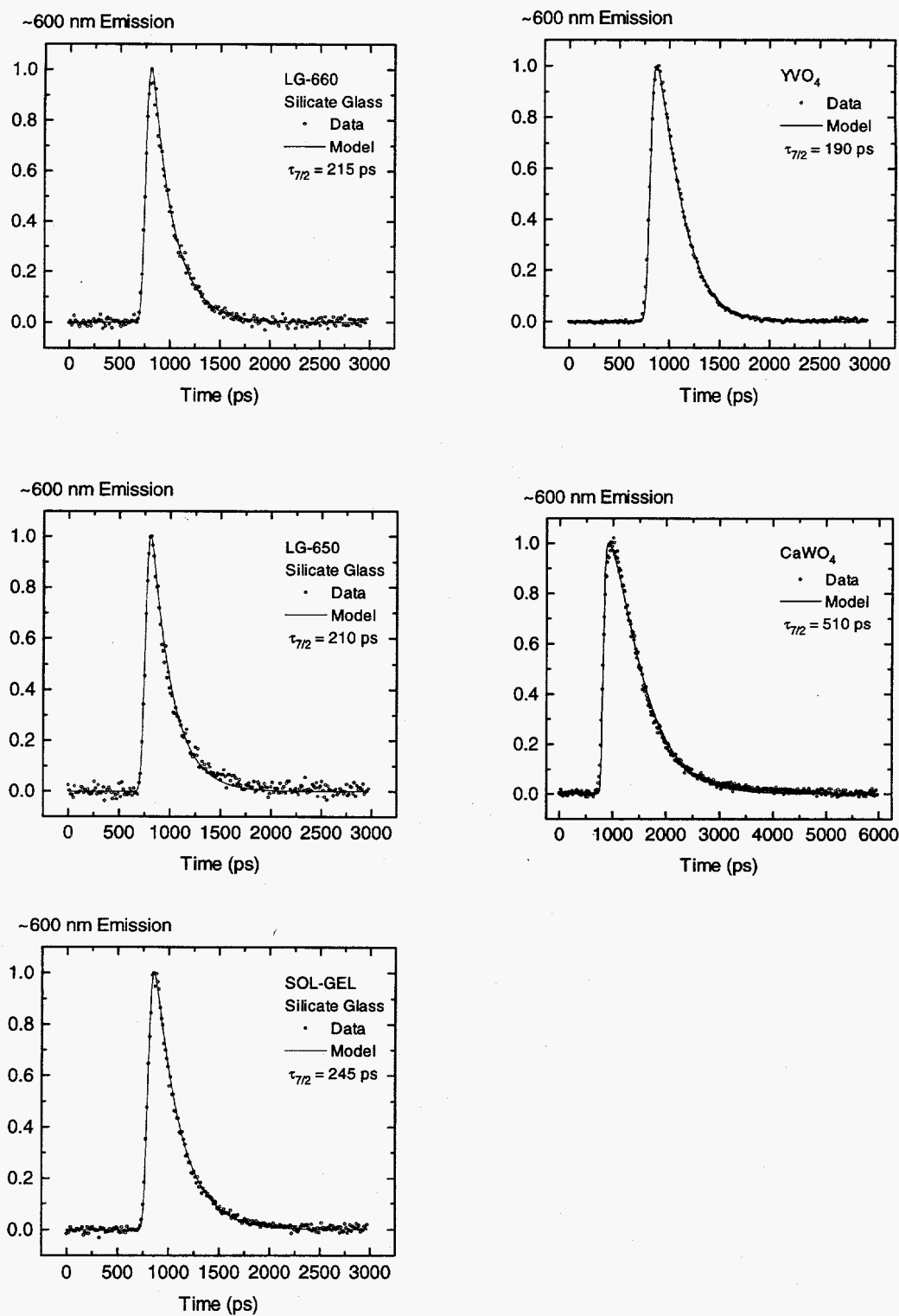
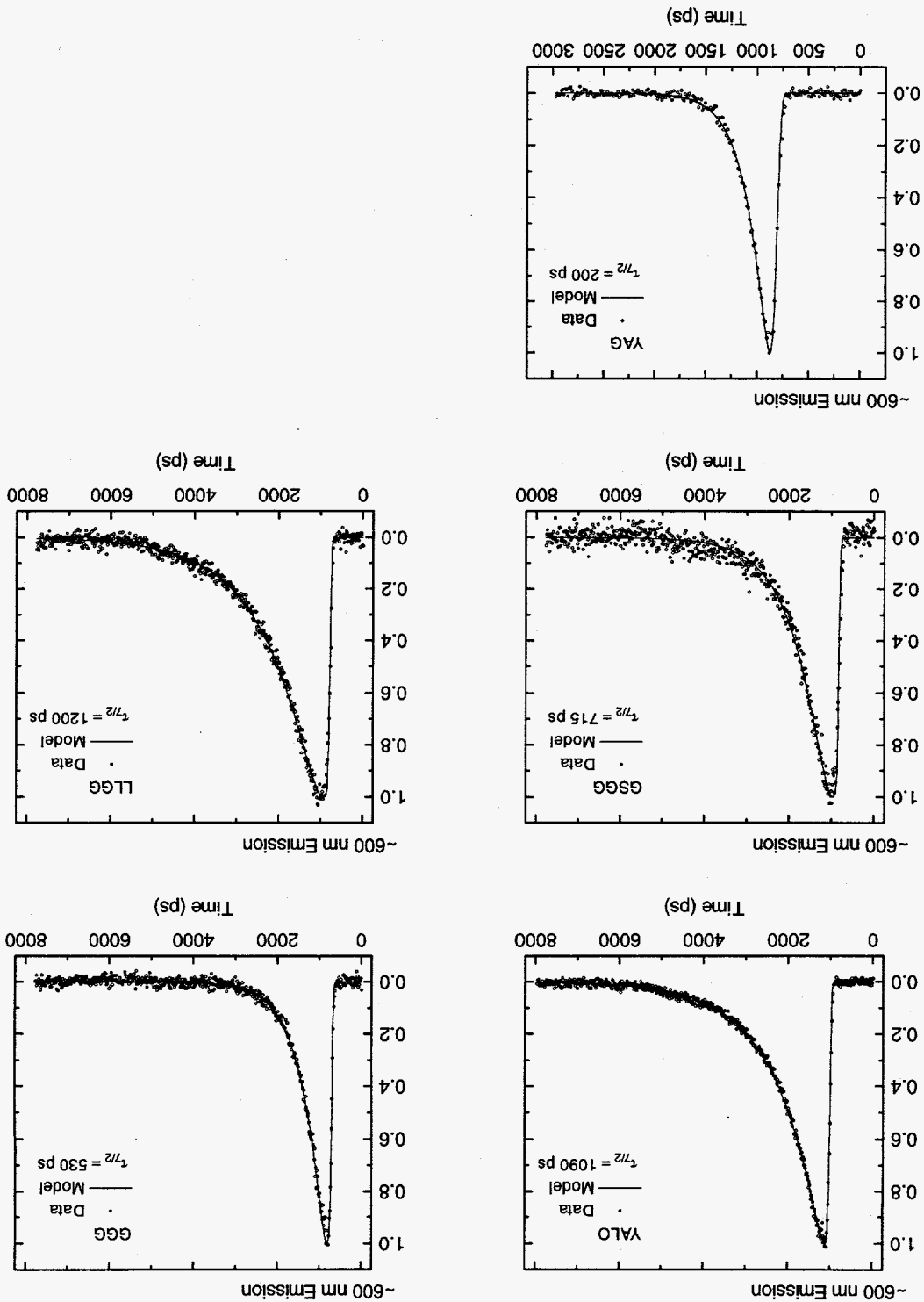


Figure 3.4 Data and numerical fits from single-photon counting experiments for Nd-doped silicate glasses and for a vanadate and tungstate crystal.

Figure 3.5 Data and numerical fits from single-photon counting experiments for Nd-doped oxide crystals.



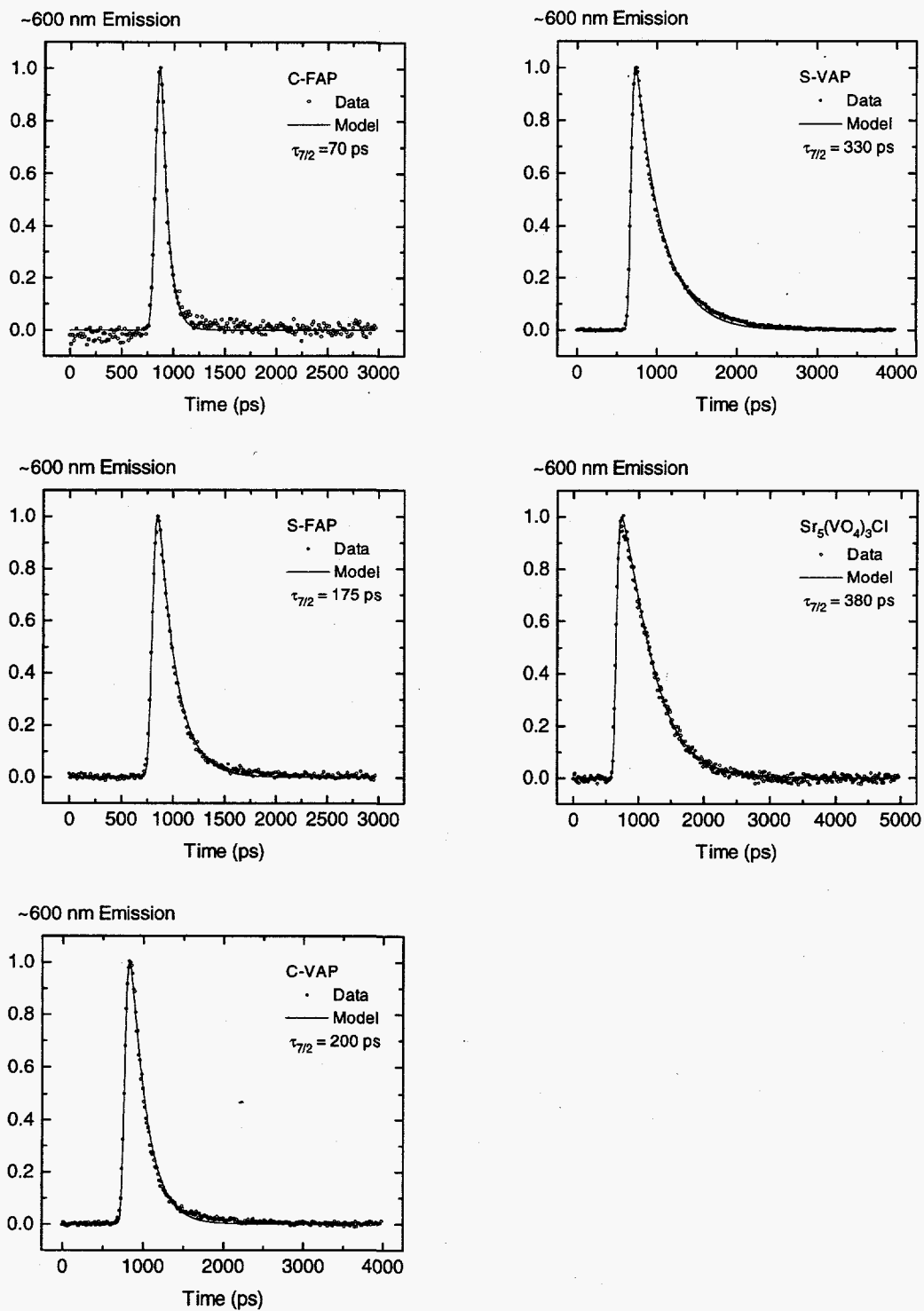


Figure 3.6 Data and numerical fits from single-photon counting experiments for several Nd-doped apatite crystals.

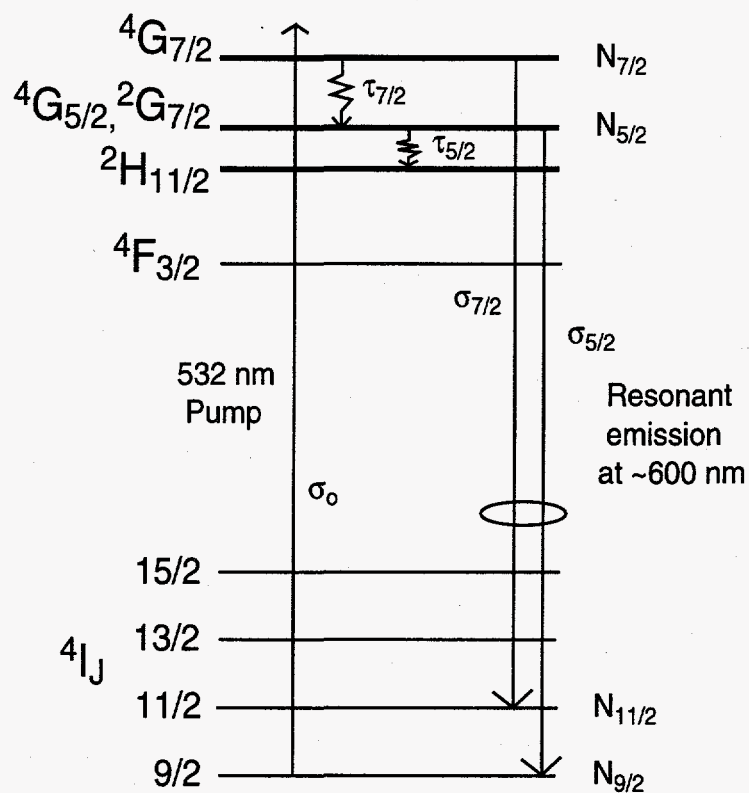


Figure 3.7 The 600 nm emission signal arises from both the $4G_{7/2} \rightarrow 4I_{11/2}$ and $4G_{5/2}, 2G_{7/2} \rightarrow 4I_{9/2}$ transitions and so the data will include information about both the $\tau_{7/2}$ and $\tau_{5/2}$ lifetimes. Employing a Judd-Ofelt analysis of the emission cross sections ($\sigma_{7/2}$ and $\sigma_{5/2}$), we can model the data to determine both of the lifetimes.

532 nm Pump Pulse Shape

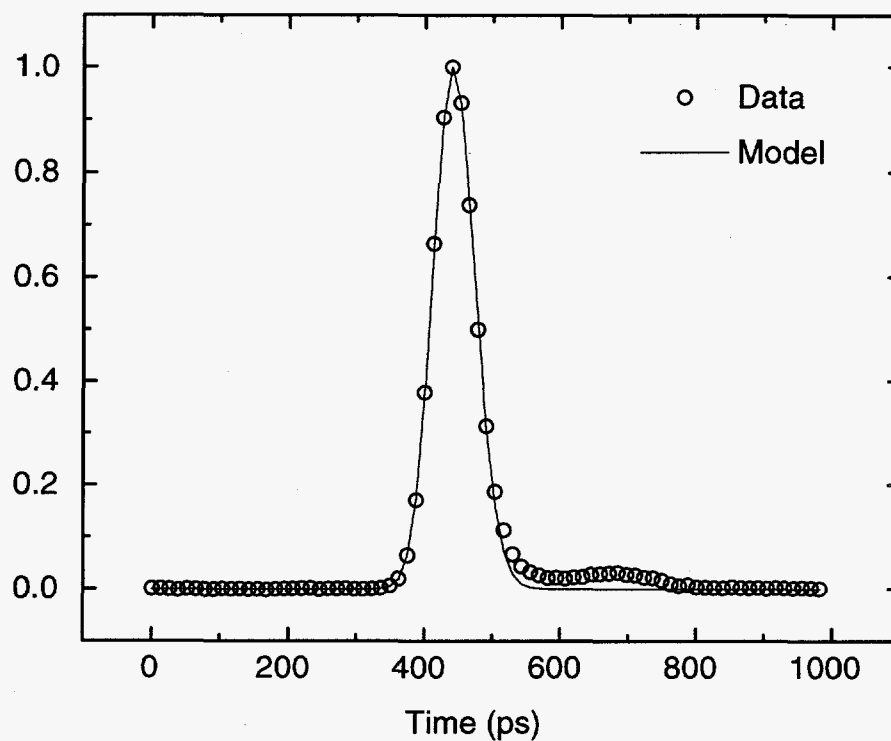


Figure 3.8 The 532 nm pump pulse is shown as the open circles. An asymmetric Gaussian with $1/e$ half pulse widths of 39 ps and 48 ps provided the best fit to the data (solid line). The calculated pulse shape was substituted into I_{pump} and used in the numerical analysis.

Nd-doped phosphate glass

Nd-doped fluorophosphate glass

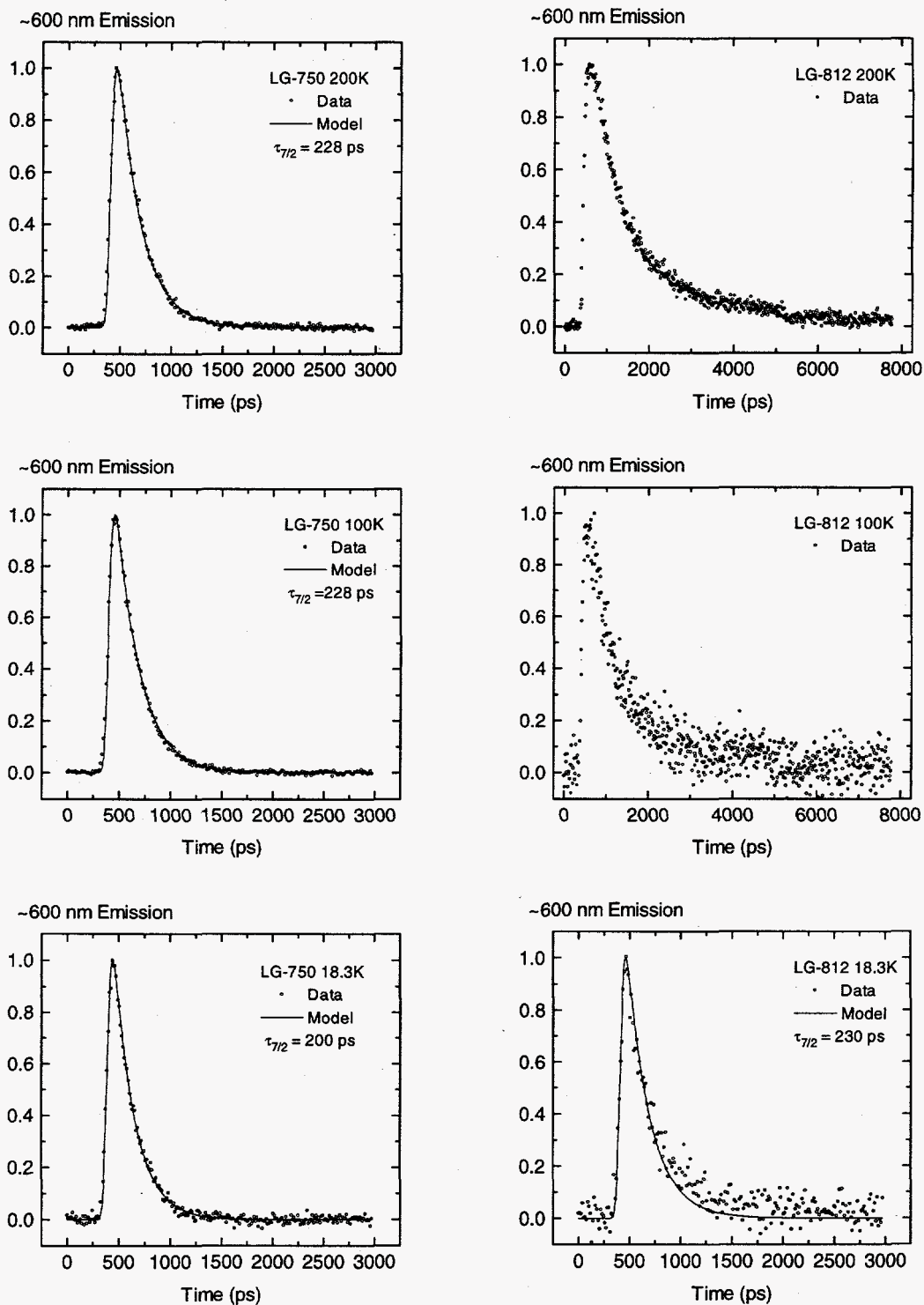


Figure 3.9 Temperature data and numerical fits for Nd-doped phosphate and fluorophosphate glasses.

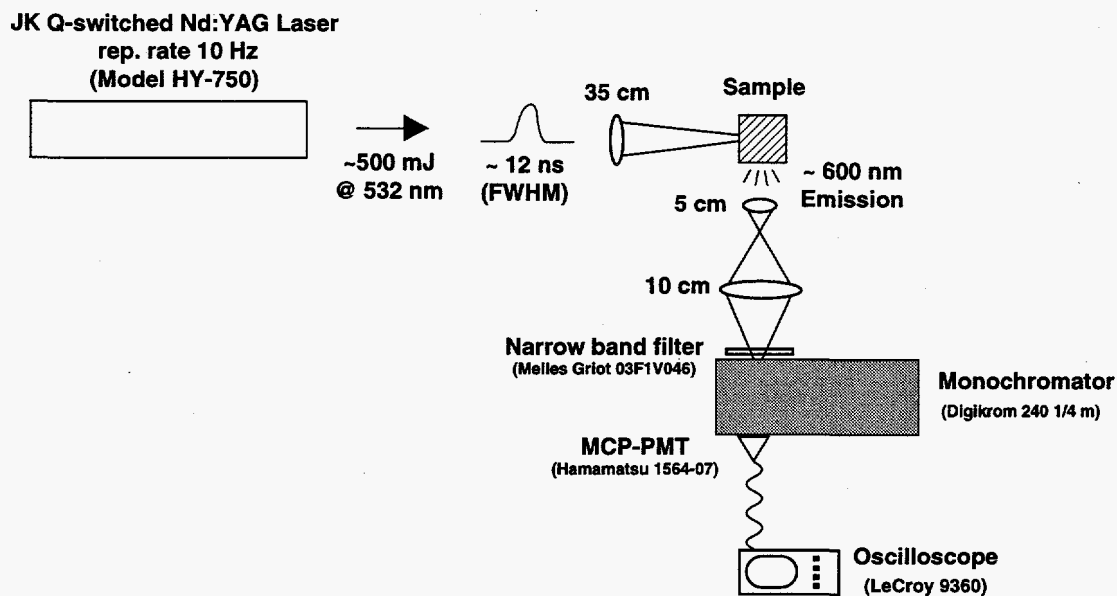


Figure 3.10 The experimental scheme for measuring the $\tau_{7/2}$ lifetime for the ${}^4G_{7/2} \rightarrow {}^4G_{5/2}$, ${}^2G_{7/2}$ transition in 10 fluoride materials is shown above. A 532 nm light pulse is focused into the fluoride sample and the emission at ~ 600 nm is collected and imaged onto the entrance slit of the monochromator. A very sensitive detector (MCP-PMT) records the emission signal at the exit slit. The recorded signal then is stored on an oscilloscope where a total of 10,000 shots were averaged to produce the final data curve.

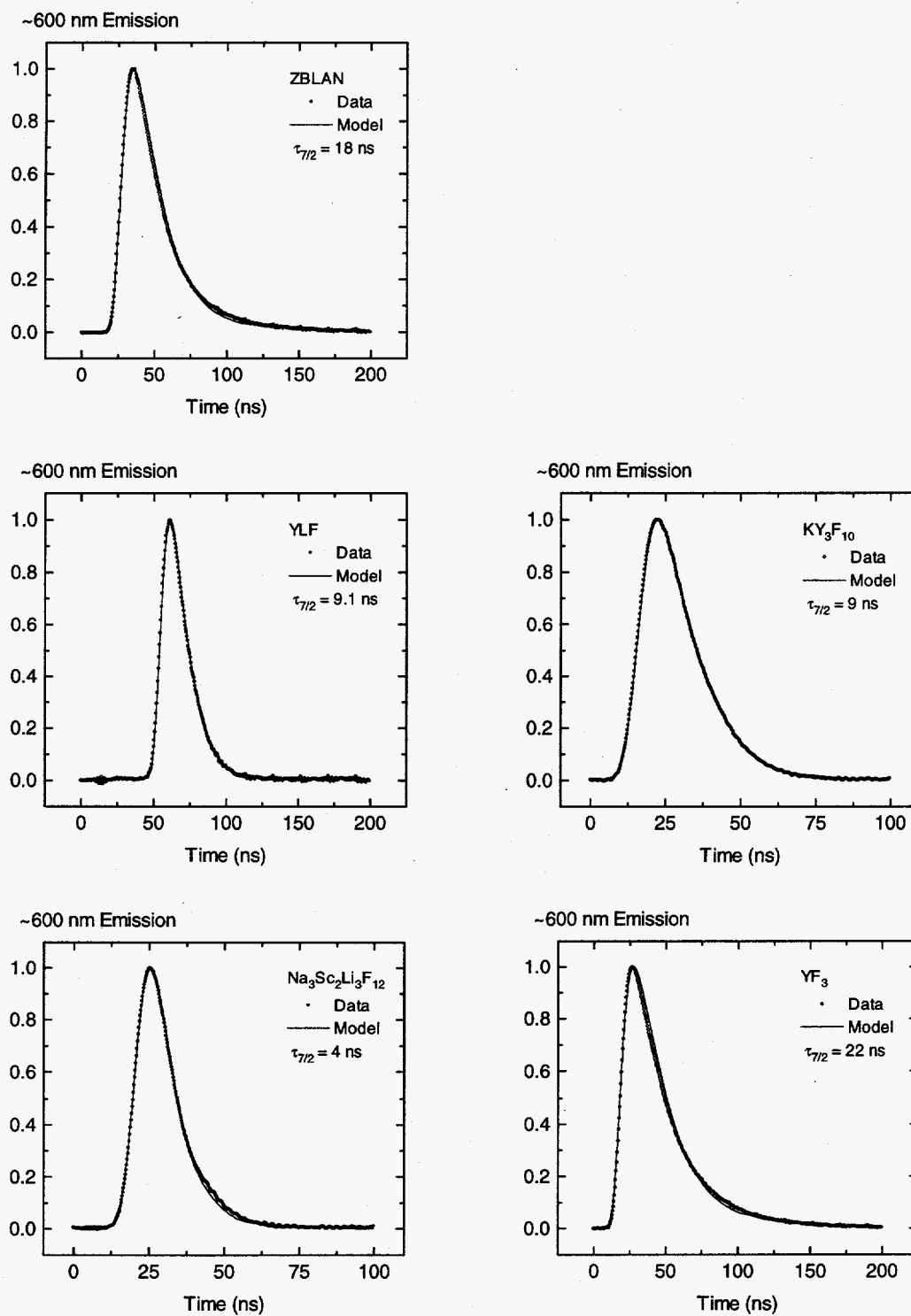


Figure 3.11 Data and numerical fits from emission experiments.

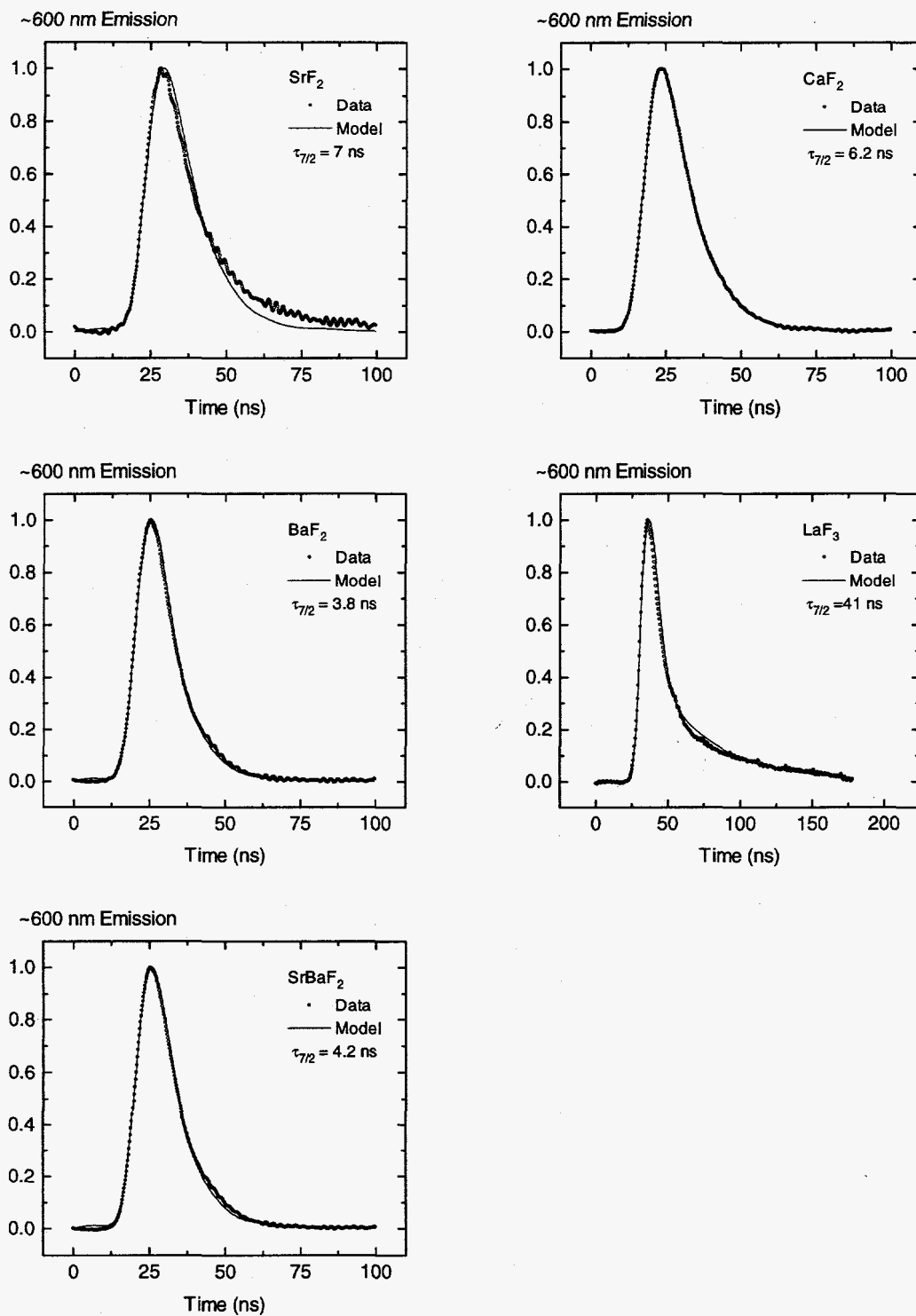


Figure 3.12 Data and numerical fits from emission experiments.

532 nm Pump Pulse Shape for Fluoride Materials

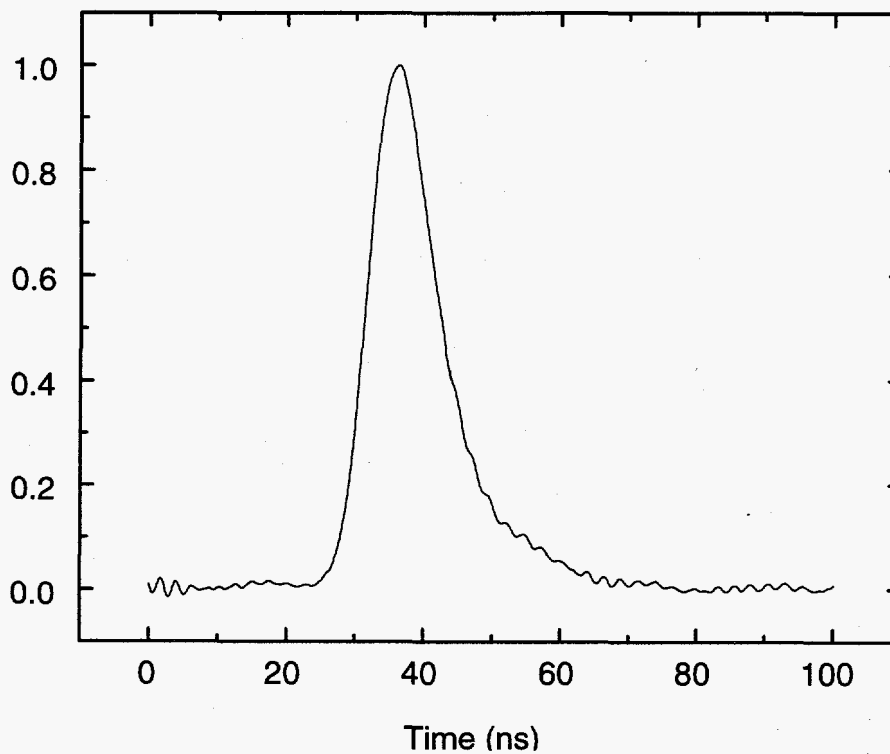


Figure 3.13 The 532 nm pump pulse for the emission experiments is shown as the solid line. Since the pulse shape could not be accurately modeled by a Gaussian, we chose to use the actual shape in the numerical analysis.

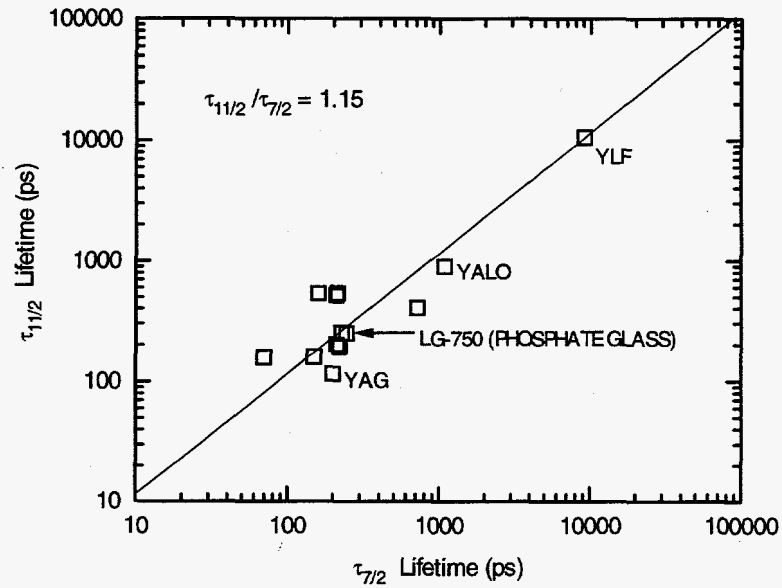


Figure 3.14 The terminal level lifetimes from the direct and indirect measurements are plotted. A best fit to the data is shown as the solid line of the form $y = mx$. The slope was found to be 1.15. We find that the indirect method ($\tau_{7/2}$) can be used to measure the terminal level lifetime ($\tau_{1/2}$) to within a factor of two for most Nd-doped laser materials.

Chapter 3 References

- ¹L. A. Riseberg and H. W. Moos, "Multiphonon orbit-lattice relaxation of excited states of rare-earth ions in crystals," *Phys. Rev.* **174**, 429 (1968).
- ²C. B. Layne, W. H. Lowdermilk, and M. J. Weber, "Multiphonon relaxation of rare-earth ions in oxide glasses," *Phys. Rev. B* **16**, 10 (1977).
- ³D. V. O'Connor and D. Phillips, "*Time-Correlated Single Photon Counting*," Academic Press (1984).
- ⁴H. Kume, K. Koyama, K. Nakatsugawa, S. Suzuki, and D. Fatlowitz, "Ultrafast microchannel plate photomultipliers," *Appl. Optics* **27**, 1170 (1988).
- ⁵T. T. Basiev, A. Y. Dergachev, Y. V. Orlovskii, and A. M. Prokhorov, "Multiphonon nonradiative relaxation from high-lying levels of Nd³⁺ ions in fluoride and oxide laser materials," *OSA Proceedings on Advanced Solid-State Lasers* **10**, 358 (1991).
- ⁶E. D. Reed Jr., "Multiphonon relaxation of excited states of rare-earth ions in yttrium-vanadate, yttrium-arsenate and yttrium-phosphate," Ph.D. Thesis, Johns Hopkins University, Baltimore MD (1972).
- ⁷B. R. Judd, "Optical absorption intensities of rare-earth ions," *Phys. Rev.* **127**, 750 (1962).
- ⁸G. S. Ofelt, "Intensities of crystal spectra of rare-earth ions," *J. of Chem. Phys.* **37**, 511 (1962).
- ⁹W. F. Krupke, "Induced-emission cross sections in neodymium laser glasses," *IEEE J. Quantum Electron.* **QE-10**, 450 (1974).
- ¹⁰W. T. Carnall, H. Crosswhite, and H. M. Crosswhite, *Energy level structure and transition probabilities of the trivalent lanthanides in LaF₃*, (Argonne National Laboratory, Argonne, Ill.)
- ¹¹D. Heiman, R. W. Hellwarth, and D. S. Hamilton, "Raman scattering and nonlinear refractive index measurements of optical glasses," *J. Non-Crystalline Solids* **34**, 63 (1979).
- ¹²K. A. Gschneidner, Jr. and L. Eyring, *Handbook on the Physics and Chemistry of Rare Earths*, **5**, Chap. 46, (North-Holland, New York, 1982).
- ¹³A. A. Kaminskii et al., *Physics and Spectroscopy of Laser Crystals*, Izdatelstvo, "Nauka" (1986).
- ¹⁴E. D. Reed Jr, and H. W. Moos, "Multiphonon relaxation of excited states of rare-earth ions in YVO₄, YAsO₄, and YPO₄," *Phys. Rev. B* **8**, 980 (1973).
- ¹⁵S. P. S. Porto and J. F. Scott, "Raman spectra of CaWO₄, SrWO₄, CaMoO₄, and SrMoO₄," *Phys Rev.* **157**, 716 (1967).
- ¹⁶M. J. Weber, T. E. Varitimos, B. H. Matsinger, "Optical absorption intensities of rare-earth ions in yttrium orthoaluminate," *Phys. Rev. B* **8**, 47 (1973).
- ¹⁷M. J. Weber, "Multiphonon relaxation of rare-earth ions in yttrium orthoaluminate," *Phys. Rev. B* **8**, 54 (1973).
- ¹⁸J. B. Gruber, M. E. Hills, C. A. Morrison, G. A. Turner, and M. R. Kokta, "Absorption spectra and energy levels of Gd³⁺, Nd³⁺, and Cr³⁺ in the garnet Gd₃Sc₂Ga₃O₁₂," *Phys. Rev. B* **37**, 8564 (1988).
- ¹⁹A. A. Kaminskii and L. Li, "Analysis of spectral line intensities of TR³⁺ ions in disordered crystal systems," *Phys. Status Solidi (a)* **26**, K21 (1974).

-
- ²⁰J. P. Hurrell, S. P. S. Porto, I. F. Chang, S. S. Mitra, and R. P. Bauman, "Optical phonons of yttrium aluminum garnet," *Phys. Rev.* **173**, 851 (1968).
- ²¹A. A. Kaminskii, *Laser Crystals: Their Physics and Properties*, Springer-Verlag, 133 (1990).
- ²²W. F. Krupke, "Transition probabilities in Nd:GGG," *Opt. Commun.* **12**, 210 (1974).
- ²³P. Zhang, Y. Liu, and Y. Mo, "The Raman spectrum of single crystal $\text{Gd}_3\text{Ga}_5\text{O}_{12}$," *Chinese Phys.* **4**, 530 (1984).
- ²⁴T. H. Allik, S. A. Stewart, et al. "Preparation, structure, and spectroscopic properties of $\text{Nd}^{3+}:\{\text{La}_{1-x}\text{Lu}_x\}_3[\text{Lu}_{1-y}\text{Ga}_y]_2\text{Ga}_3\text{O}_{12}$ crystals," *Phys. Rev. B* **37**, 9129 (1988).
- ²⁵John B. Gruber, Private Communication, San Jose State University, CA.
- ²⁶S. R. Levitt, K. C. Blakeslee, and R. A. Condrate, Sr., "Infrared spectra and laser-Raman spectra of several apatites," *Memoires de la Societe Royal des Sciences de Liege* **5**, 121 (1970).
- ²⁷R. E. Peale, P. L. Summers, H. Weidner, B. H. T. Chai, and C. A. Morrison, "Site-selective spectroscopy and crystal-field analysis for Nd^{3+} in strontium fluorovanadate," *J. Appl. Phys.* **77**, 270 (1995).
- ²⁸D. K. Sardar and P. D. Bella, "Optical characterization of $\text{Nd}^{3+}:\text{Sr}_5(\text{VO}_4)_3\text{F}$," *J. Appl. Phys.* **76**, 5900 (1994).
- ²⁹E. B. Sveshnikova, A. A. Stroganov, and L. N. Urusovskaya, "Mechanism of nonradiative transitions in rare-earth ions in fluorozirconate bases," *Opt. Spectrosc. (USSR)* **63** (5), 618 (1987).
- ³⁰S. A. Miller, H. E. Rast, and H. H. Caspers, "Lattice Vibrations of LiYF_4 ," *J. Chem. Phys.* **52**, 4172 (1970).
- ³¹I. Richman, "Vibronic Spectra of $\text{SrF}_2:\text{Sm}^{2+}$ and $\text{BaF}_2:\text{Sm}^{2+}$," *Phys. Rev.* **133**, A1364 (1964).
- ³²R. P. Bauman and S. P. S. Porto, "Lattice vibrations and structure of rare-earth fluorides," *Phys. Rev.* **161**, 842 (1967).

Chapter 4

Measurements of the nonradiative lifetime ($\tau_{5/2}$) for the ${}^4G_{5/2}, {}^2G_{7/2} \rightarrow {}^2H_{11/2}$ transition in 10 Nd-doped fluoride materials

4.1 Introduction

The fluorides represent a class of materials which tend to possess low phonon frequencies ($300\text{-}600\text{ cm}^{-1}$) compared to other laser materials such as the phosphates, silicates, and oxides, which have higher frequency phonons ranging from ($700\text{-}1200\text{ cm}^{-1}$). As a consequence, the nonradiative lifetimes tend to be longer and on nanosecond time scales. This is because an increased number of phonons are needed to bridge the energy gap (2-3) resulting in a higher order process necessary to complete the nonradiative transition. Of the fluorides investigated, Nd:YLF (LiYF_4) is still the most commonly used material in many commercial laser systems. Our measurements of the $\tau_{5/2}$ lifetime allowed us to assess whether the energy gap law was still valid for Nd:YLF and provide additional data for future theoretical evaluations of the energy gap law.

4.2 Experimental arrangement

The energy level diagram for the pumping and emission processes are shown in **Figure 4.1**. The ground state Nd ions are excited with a 582.5 nm pump beam from the output of a dye laser. The $\sim 655\text{ nm}$ emission signal corresponding to the ${}^4G_{5/2}, {}^2G_{7/2} \rightarrow {}^4I_{11/2}$ transition is recorded with an oscilloscope.

The experimental layout is shown in **Figure 4.2**. A JK Q-switched Nd:YAG laser (Model HY-750) operating at 10 Hz produced frequency doubled output pulses of $\sim 500\text{ mJ}$ at 532 nanometers. These pulses were injected into a Lumonics dye laser (Model HD-300, dye R6-G) to produce the 582.5 nm excitation pulses. A 35 cm focal length lens was used to focus the light into the sample and a 5 cm focal length lens with a diameter of 2.5 cm collected the $\sim 655\text{ nm}$ emission from the side of the sample. The image of the focus was then magnified and relayed to the monochromator slit entrance with a 10 cm lens in order to match the $f/4$ optical system of the Digikrom monochromator (Model 240). Depending on the signal level, the slit width ranged from 100-250 μm . A

narrowband filter (Melles Griot 03F1V048) was placed at the slit entrance to block out unwanted frequencies and a Hamamatsu MCP-PMT detector (1564-07) was placed at the output of the monochromator. A LeCroy oscilloscope (Model 9306) was used to capture the entire emission signal after one excitation pulse. However, since the emission signal levels were very low (1-10 mV at the signal peak), we chose to average 10,000 emission signals for each sample. The incoming signals were internally stored and averaged on the LeCroy oscilloscope before being transferred onto a storage disk.

4.3 Results and summary

The data and model for 10 Nd-doped fluoride samples are shown in **Figures 4.3 and 4.4**. The model was based on the solution to the rate equation described below:

$$\frac{dN_{5/2}}{dt} = -\frac{N_{5/2}}{\tau_{5/2}} + N_{11/2}\sigma_0 \frac{I_{\text{pump}}}{h\nu_{582.5}} \quad (1)$$

where we assume that the lower level population remains approximately constant:

$$N_{11/2} \cong \text{constant} \quad (2)$$

The shape of the pump pulse is shown in **Figure 4.5**. We recorded the temporal shape by allowing a small amount of the 582.5 nm light to pass through the monochromator (set at 20 μm) and into the MCP-PMT detector. This shape was used for all of the data modeling. The results of our analysis are listed in **Table 4.1** along with the energy gaps and highest phonon frequencies where known. Based on an analysis of the best fit to the data, the uncertainty in the value of the lifetimes is $\Delta\tau_{5/2} (<10 \text{ ns}) = \pm 1 \text{ ns}$ for data with lifetimes less than 10 ns and $\Delta\tau_{5/2} = \pm 2 \text{ ns}$ for the LaF_3 data. The doping concentration for the ZBLAN glass was ~2-5 weight % whereas for the fluoride crystals, the doping levels ranged from 0.1-2%.

With the exception of the $\text{Nd}:\text{SrBaF}_2$ sample, we found the $\tau_{5/2}$ lifetimes to be shorter than the $\tau_{7/2}$ lifetimes measured in Chapter 3 due to the ~300-400 cm^{-1} smaller energy gap. In the $\text{Nd}:\text{SrBaF}_2$ sample, we found that the lifetime increased from 4.2 ns for the ${}^4\text{G}_{7/2} \rightarrow {}^4\text{G}_{5/2}, {}^2\text{G}_{7/2}$ transition to 6.6 ns for the ${}^4\text{G}_{5/2}, {}^2\text{G}_{7/2} \rightarrow {}^2\text{H}_{11/2}$ transition. This is an anomalous result which cannot be explained by our current understanding of the energy gap law.

With the exception of LaF_3 , which had the longest measured lifetime of 15 ns, all of the fluoride materials investigated had lifetimes ranging between 2-7 ns. We found similar results in a report recently published by Basiev et al.¹ where they measured the $\tau_{5/2}$ lifetime to be 14.7 ns, 8.7-16.8 ns, and 4.6 ns for LaF_3 , SrF_2 , and a fluoride glass respectively, compared to our values of 15 ns, 5.7-6.2 ns, and 5.2 ns (ZBLAN). The range of lifetimes found in SrF_2 suggests that the data should be fit with a model that accounts for the possibility of two or more environments surrounding the Nd ion. We know that different sites surrounding the Nd ion can result in varying strengths of the crystal-field coupling. In sites where the coupling is strong, the transfer of energy from the Nd ion to the surrounding lattice can take place more quickly, resulting in shorter measured lifetimes.

In order to verify whether the energy gap law is still valid for transitions with smaller gaps, we needed additional data for the nonradiative transitions involving larger energy gaps. Unfortunately, for many of the fluoride samples studied, the data (at room temperature) were not available. We did however, find additional data^{1,2} for Nd:YLF and plotted the nonradiative rates as a function of the energy gap in **Figure 4.6**. As predicted by the energy gap law, the data still appears to follow a linear relationship. In the next chapter we will explore an alternative theory for predicting the nonradiative rates. In general, because of the lower phonon frequencies found in the fluoride hosts, the nonradiative lifetimes of these materials will tend to be longer (nanoseconds) because the order of the process is larger; that is, the number of phonons required to bridge the energy gap is larger as illustrated in **Figure 4.7**.

Table 4.1 A summary of the $\tau_{5/2}$ lifetimes measured from the emission experiments and the corresponding energy gaps $\Delta E_{5/2}$ and effective phonon frequencies ($h\nu_{\text{eff}}$) if known.

Material	$\tau_{5/2}$ lifetime (ns)	$\Delta E_{5/2}$ (cm^{-1})	$h\nu_{\text{eff}}$ (cm^{-1})
Fluoride glass ZBLAN ($\text{Zr}_4\text{-BaF}_2\text{-AlF}_3\text{-LaF}_3\text{-NaF}$)	5.2	-	580 ³
Fluoride crystals LiYF ₄	2.8	1024 ⁴	560 ⁵
Na ₃ Sc ₂ Li ₃ F ₁₂	3.3	-	-
KY ₃ F ₁₀	3	-	-
YF ₃	5	-	-
SrF ₂	5.7-6.2	1136 ¹	360 ⁶
BaF ₂	3.4	-	321 ⁶
SrBaF ₂	6.6 ^a	-	-
CaF ₂	5	-	525 ¹
LaF ₃	15	1141 ¹	414 ⁷

(a) The $\tau_{5/2}$ lifetime is anomalously larger than the $\tau_{7/2}$ lifetime (4.2 ns) reported in Chapter 3.

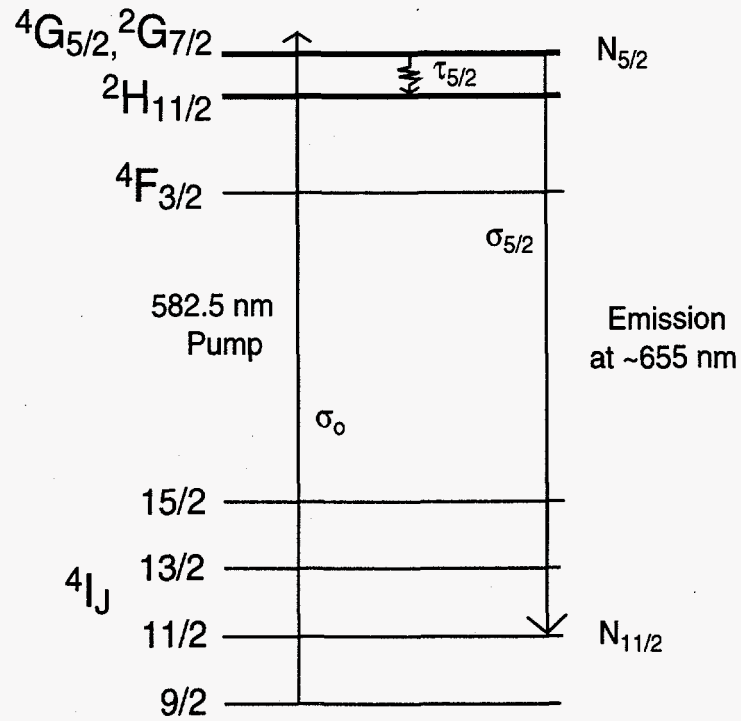


Figure 4.1 An energy level diagram that showing the pump and emission processes involved in measuring the $\tau_{5/2}$ nonradiative lifetime for the $4G_{5/2}, 2G_{7/2} \rightarrow 4I_{11/2}$ transition in 10 fluoride materials.

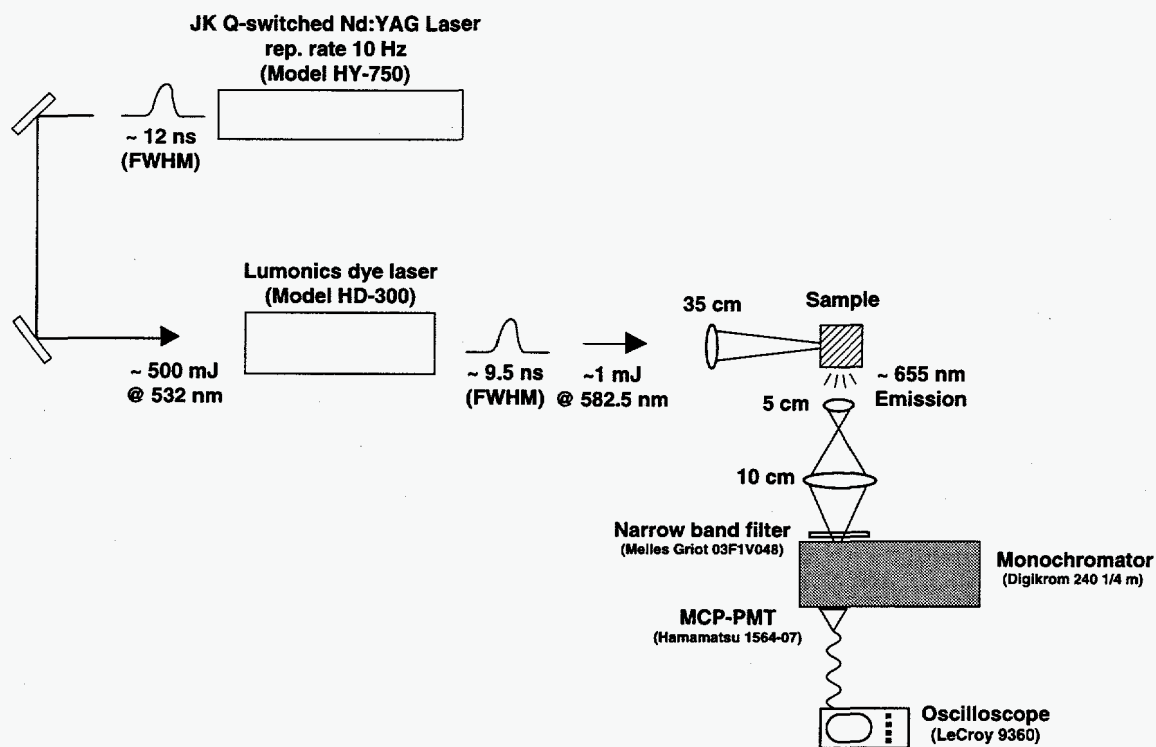


Figure 4.2 The experimental scheme for measuring the $\tau_{5/2}$ lifetime for the ${}^4G_{5/2}, {}^2G_{7/2} \rightarrow {}^2H_{11/2}$ transition in 10 fluoride materials is shown above. A 532 nm light pulse from a JK Laser is sent into the Lumonics dye laser and converted into 582.5 nm light. The 582.5 nm light is focused into the fluoride sample and the emission at ~ 655 nm is collected and imaged onto the entrance slit of the monochromator. A very sensitive detector (MCP-PMT) records the emission signal at the exit slit. The recorded signal is stored on an oscilloscope, where a total of 10,000 shots were averaged to produce the final data curve.

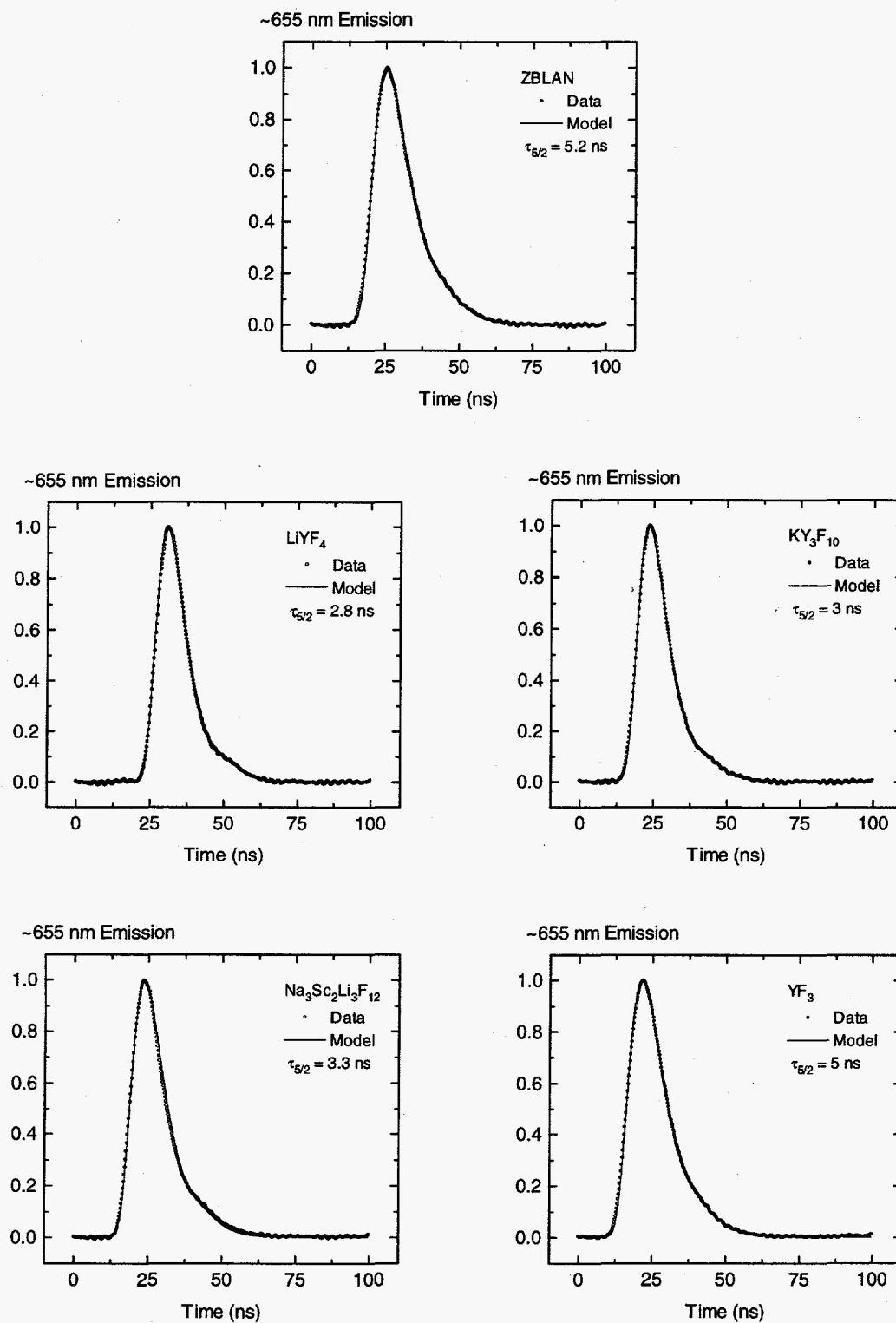


Figure 4.3 Data and numerical fits from emission experiments.

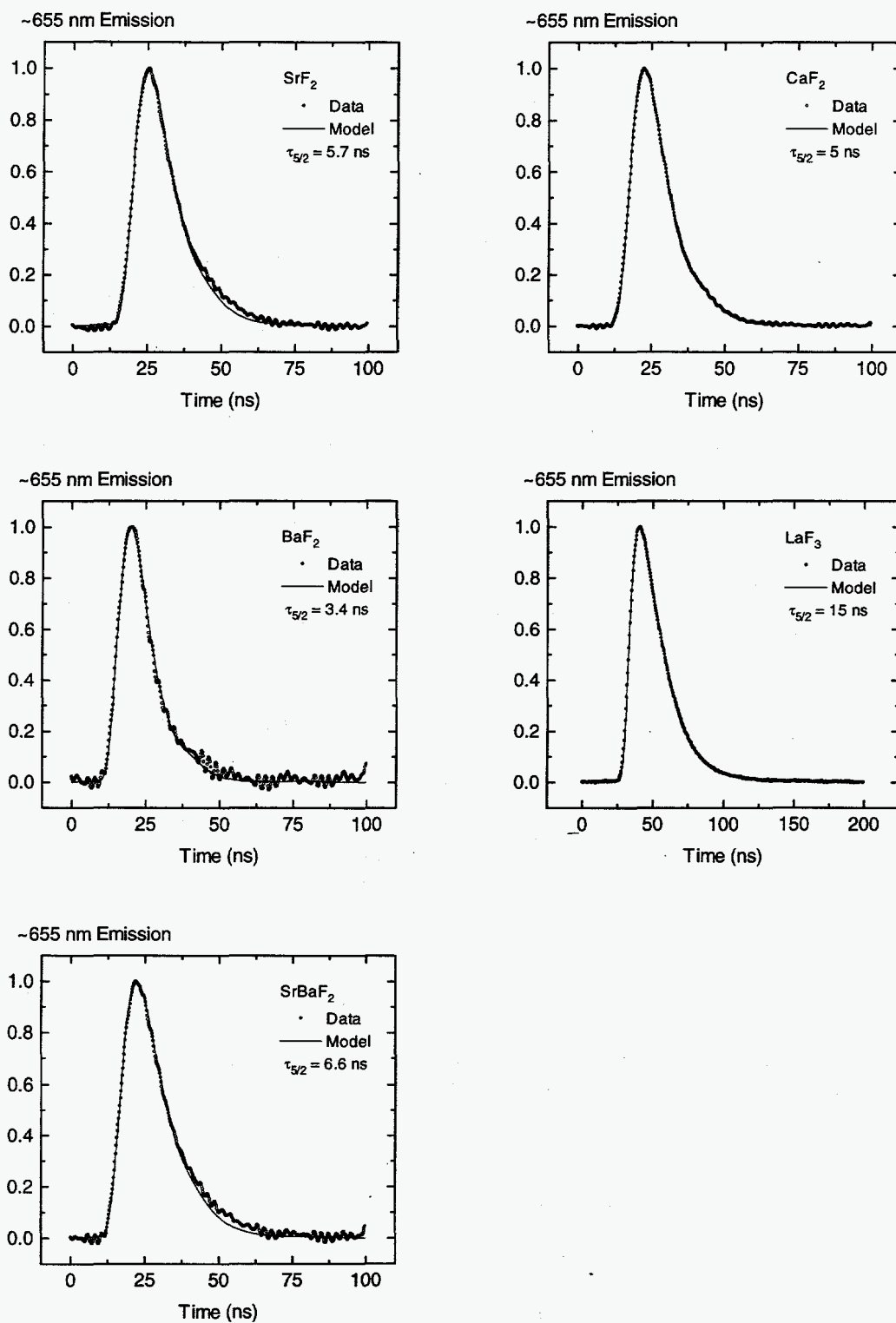


Figure 4.4 Data and numerical fits from emission experiments.

582.5 nm Pump Pulse Shape for Fluoride Materials

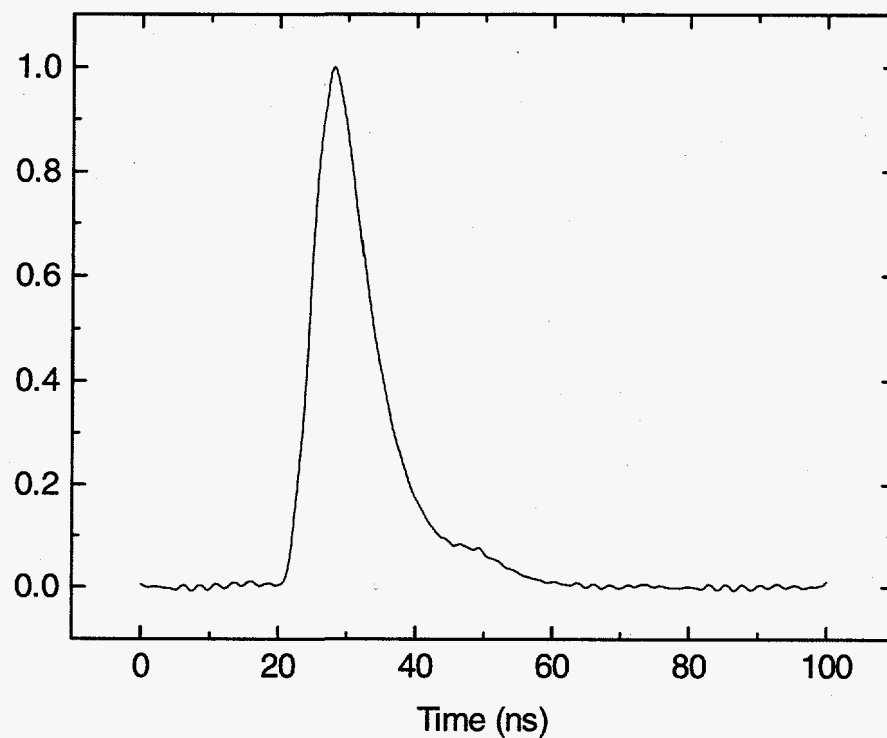


Figure 4.5 The 582.5 nm pump pulse for the emission experiments is shown as the solid line. Due to the asymmetric shape of the pulse, we chose to use the actual shape in the numerical analysis.

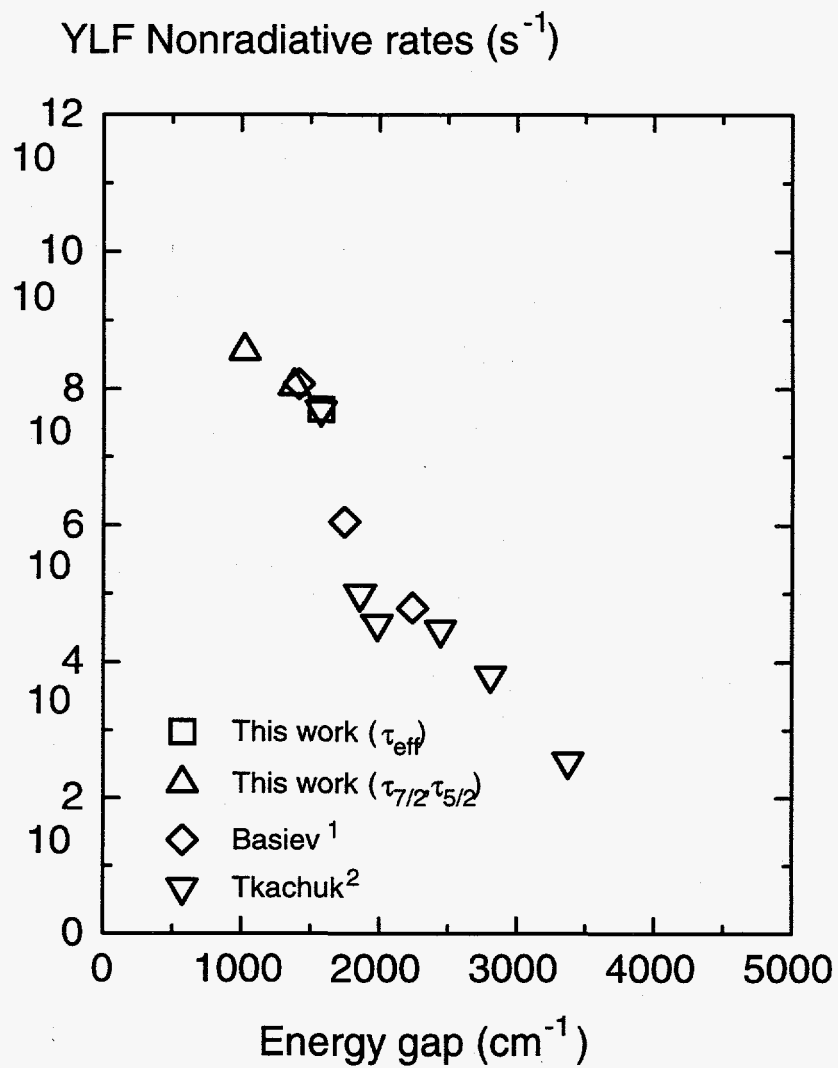
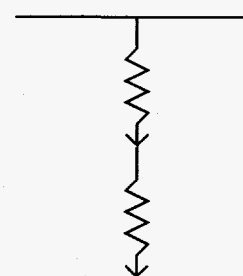
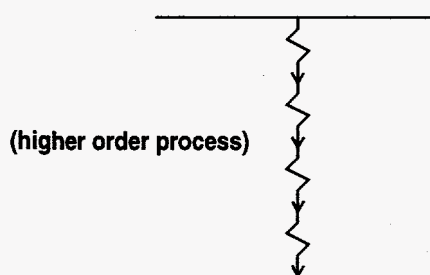


Figure 4.6 A plot of the nonradiative rate (W_{nr}) versus energy gap for Nd:YLF. The energy gap law appears to still be valid for the faster rates and smaller energy gaps.

$$W_{nr} = A \exp\left(-\kappa \frac{\Delta E_{gap}}{h\nu_{eff}}\right) \quad \tau_{nr} = 1/W_{nr}$$

Host A
 lower effective ($h\nu_{eff}$)
 phonon energies
 (e.g. fluorides)

Host B
 higher effective ($h\nu_{eff}$)
 phonon energies
 (e.g. phosphates, silicates, oxides)



W_{nr} (4-phonon)

<

W_{nr} (2-phonon)

Figure 4.7 Based on the energy gap law expression, smaller energy gaps (ΔE_{gap}) and higher effective phonon energies ($h\nu_{eff}$) lead to shorter nonradiative lifetimes (W_{nr}).

Chapter 4 References

- ¹T. T. Basiev, A. Y. Dergachev, Y. V. Orlovskii, and A. M. Prokhorov, "Multiphonon nonradiative relaxation from high-lying levels of Nd³⁺ ions in fluoride and oxide laser materials," OSA Proceedings on Advanced Solid-State Lasers **10**, 358 (1991).
- ²A. M. Tkachuk, A. V. Khilko, and M. V. Petrov, "Probabilities for nonradiative intermultiplet transitions in the holmium ion in lithium-yttrium double fluoride crystals and stimulated emission," Opt. Spectrosc. (USSR) **58** (2), 216 (1985).
- ³E. B. Sveshnikova, A. A. Stroganov, and L. N. Urusovskaya, "Mechanism of nonradiative transitions in rare-earth ions in fluorozirconate bases," Opt. Spectrosc. (USSR) **63** (5), 618 (1987).
- ⁴K. A. Gschneidner, Jr. and L. Eyring, *Handbook on the Physics and Chemistry of Rare Earths*, **5**, Chap. 46, (North-Holland, New York, 1982).
- ⁵S. A. Miller, H. E. Rast, and H. H. Caspers, "Lattice Vibrations of LiYF₄," J. Chem. Phys. **52**, 4172 (1970).
- ⁶I. Richman, "Vibronic Spectra of SrF₂:Sm²⁺ and BaF₂:Sm²⁺," Phys. Rev. **133**, A1364 (1964).
- ⁷R. P. Bauman and S. P. S. Porto, "Lattice vibrations and structure of rare-earth fluorides," Phys. Rev. **161**, 842 (1967).

Chapter 5 Comparison of the energy gap theory and energy transfer model for predicting nonradiative transition rates

5.1 Introduction

The energy gap law described in Chapter 1 and shown below in Eqn. 1, continues to be the most widely used expression for predicting the nonradiative transition rates (W_{nr}) of the rare-earth ions doped into glassy or crystalline hosts.

$$W_{nr} = A \exp(-\kappa p) \quad \text{“Energy Gap Law”} \quad (1)$$

We will briefly describe the derivation of this equation and the various assumptions involved. In the next section, we will discuss an alternative method for calculating the nonradiative rates that utilizes an energy-transfer expression that is often used to describe the transfer of energy between two impurity ions within a host medium. Here, the nonradiative transition involves the transfer of energy between the “impurity” rare-earth ion (donor) and the surrounding host (acceptor). When an exponential form of the absorption coefficient is substituted within the energy-transfer equation, we find that the expression simplifies to a form very similar to that of energy gap law in Eqn. 1. We conclude the chapter by suggesting that a correlation exists between these two descriptions by showing a nearly linear dependence of the nonradiative rate on the absorption coefficient with a log-log plot for three different Nd-doped crystalline hosts.

5.2 Derivation of energy gap law by perturbation theory

The lanthanides, also known as the inner transition or rare-earth elements, occupy atomic numbers 58 through 71 in the periodic table. A survey of laser crystals by Kaminskii¹ has shown that the trivalent state of several of the lanthanides has been incorporated into numerous (over 100) host materials thus making the RE^{3+} :crystal a popular medium for many solid-state lasers. As a result of the triple ionization, the lanthanides have an unfilled or partially filled $4f^N$ orbital, where N designates the number of electrons. Normally an unfilled outer lying orbital would cause the exact spacings of the electronic energy levels to be extremely sensitive to the host environment, however, due to the radial contraction of the $4f^N$ orbital, the electrons in the $4f^N$ orbital are

shielded by the outer closed shells of the $5s^2$ and $5p^6$ orbitals (**Figure 5.1**). Subsequently, this causes the crystal field interaction (H_{cf}) with the electrons in the $4f^N$ orbital to be relatively weak compared to the Coulomb and spin-orbit interactions (**Figure 5.2**). The resulting effect of the static crystalline field is to break the spherical symmetry surrounding the ion thus allowing a partial or full lifting of the J degeneracy, where J is the total angular momentum. Therefore, when the rare-earth ion is doped into a host, the centers of gravity of the J manifolds exhibit small changes. However, the order and separation of the crystal field splittings within a J manifold (i.e. the J_μ values) will vary from host to host. We can therefore treat the crystal field interaction as a perturbation on the rare-earth ion. The total Hamiltonian for a rare-earth ion (RE^{3+}) doped into a host medium can be written as a sum of the kinetic, electron-nuclear, Coulomb, spin-orbit, and crystal field interaction Hamiltonians as follows²:

$$H = \sum_{i=1}^N \left[\frac{p_i^2}{2m} - \frac{Ze^2}{r_i} \right] + \sum_{i < j}^N \frac{e^2}{r_{ij}} + \zeta(r_i) \vec{l}_i \cdot \vec{s}_i + H_{cf} \quad (2)$$

or rewritten as: $H = [H_{kin} + H_{el-nuc} + H_{coul} + H_{so}] + H_{cf} \quad (3)$

or simply, $H = H_{free-ion} + H_{cf} \quad (4)$

In the case of the weak field approximation, the crystal field Hamiltonian is assumed to have the smallest effect on the free ion energy level spacings:

$$H_{coul}, H_{so} > H_{cf} \quad (5)$$

Schematically this is shown in **Figure 5.2**. The wavefunctions for the free ion can be written in the intermediate coupling scheme as²:

$$|4f^N[\gamma SL]J\rangle = \sum_{\gamma SL} C(\gamma SL) |4f^N \gamma SLJ\rangle \quad (6)$$

where L and S are the quantum numbers for orbital angular momentum and spin angular momentum respectively. The intermediate coupling scheme is often used when neither the LS (Russell-Saunders) nor the jj coupling schemes are valid. In this case, the Coulomb and spin orbit interactions are simultaneously diagonalized for each value of J. And therefore strictly speaking, only J is considered to be a good quantum number; this is the reason for the square brackets around S and L. However, one will still find the energy levels designated by the nomenclature $^{2S+1}L_J$ since L and S usually dominate.

Let us first only consider the static component of the crystal field surrounding the RE^{3+} ion. The static or Stark field perturbation is denoted by V_o and can be expanded in a series of spherical harmonics of the form^{3,4}:

$$V_o = \sum_{k,q,i} B_q^k (C_q^k)_i \quad (7)$$

where the B_q^k components describe the strength of the crystal field and the C_q^k are the spherical-harmonic tensor operators. The sum over the index i occurs over the number of electrons. Once the parameters describing V_o are known, the wavefunctions and energy levels can be calculated. This usually involves an iterative process of adjusting the parameters until an adequate match to the spectroscopic data is made. The new wavefunctions of the rare-earth ion in a static field are given by:

$$|4f^N[\gamma SL]J_\mu\rangle = \sum_{\gamma SLJ_z} C(\gamma SLJ_z) |4f^N\gamma SLJ_z\rangle \quad (8)$$

where μ is the crystal field quantum number. These wavefunctions represent the electronic wavefunctions for the RE-ion in the calculation of the nonradiative transition rates. In considering the nonradiative transitions, we are only interested in the dynamic contribution of the crystal field (H_{dyn}). If we expand the crystal field Hamiltonian in a Taylor expansion about the equilibrium positions of host ions, we find that the interaction crystal field Hamiltonian can be written as a sum of static and dynamic components:

$$H_{cf} = V_o + \sum_i Q_i \cdot \nabla V_{cf} + \dots \quad (9)$$

$$= V_o + \sum_i \frac{\partial V_{cf}}{\partial Q_i} Q_i + \sum_{ij} \frac{\partial^2 V_{cf}}{\partial Q_i \partial Q_j} Q_i Q_j + \dots \quad (10)$$

$$H_{cf} = H_{static} + H_{dyn} \quad (11)$$

where $V_o = H_{static}$ is the equilibrium position of the crystal lattice and the partial derivatives of the crystal field (V_{cf}) are taken with respect to the normal mode coordinates of the lattice ions (Q_i) and evaluated at the equilibrium position. Recall that V_o was used in determining the electronic wavefunctions of the rare-earth ion in a static crystalline field. To calculate the nonradiative transition rate we employ an expression from time dependent perturbation theory known as Fermi's Golden Rule². Given the total

wavefunction (φ) for our system, and the dynamic crystal field perturbation, H_{dyn} , we can write the nonradiative transition rate (W_{nr}) as:

$$W_{\text{nr}} = \frac{2\pi}{\hbar} \left| \langle \varphi_f | H_{\text{dyn}} | \varphi_i \rangle \right|^2 \rho(E) \quad (\text{Fermi's Golden Rule}) \quad (12)$$

where φ_i and φ_f are the initial and final wavefunctions respectively and $\rho(E)$ is the density of states. As mentioned in Chapter 1, there have been many theories presented as to how one might simplify the above expression in terms of measurable or calculable parameters. However, due to uncertainties in understanding the exact nature of the ion-lattice interaction, many assumptions are required in order to simplify the expression. In this discussion we follow a simple and intuitive derivation presented by Layne⁵ to illustrate how the phenomenological form of the gap law expression is derived. A few important assumptions made in the derivation are:

- 1.) Born-Oppenheimer approximation for the lattice and ion wavefunctions allowing the total wavefunction of the system to be a product of the rare-earth electronic wavefunction and the lattice wavefunction
- 2.) Harmonic oscillator approximation in treatment of lattice vibrations and their wavefunctions
- 3.) Weak ion-lattice coupling due to shielding effects
- 4.) Neglect of detailed electron and phonon properties due to the large number of interacting phonon modes and intermediate states
- 5.) Relaxation of selection rules, since higher order multiphonon processes involve statistical averaging

We will consider additional approximations as they arise in the derivation. The total wavefunction for the ion-lattice can be written as:

$$|\varphi\rangle = |\psi_{\text{el}}\rangle |\psi_{\text{lattice}}\rangle \quad (13)$$

$$|\varphi\rangle = |\psi_{\text{el}}\rangle \prod_{\omega_i=1}^m |n_{\omega_i}\rangle \quad (14)$$

where the total wavefunction is a product of the electronic wavefunction for the ion and the lattice wavefunction. The lattice wavefunction can be written as product of harmonic oscillator wavefunctions over all possible modes, m , that can couple to the rare-earth ion.

The variable n_{ω} , corresponds to the phonon occupation number. In a crystal, since the long range ordering of the lattice is disrupted by the incorporation of the rare-earth ion, the normal modes of vibration could be those of a unit cell centered around the ion⁵. This allows us to simplify our discussion to include only the nearest neighbor vibrations which couple efficiently to the rare-earth ion. However, in a glass, the concept of a phonon is slightly different. Within a glass, there are network forming ions such as P, Si, B, Ge, which can form tetrahedral units such as PO₄. In addition, there are network modifiers such as the alkali ions, which break up the P-O-P-O bonds. In this formulation we assume that:

$$\omega_{\text{network modifiers}} < \omega_{\text{network formers}} \quad (15)$$

so that only the high energy vibrations will be considered and will usually involve the localized vibrations of the glass forming units. For example in the silicate, phosphate, borate, and ZBLAN fluoride glasses, the networking forming units are the SiO₄, PO₄, BO₄, and ZrF₄ tetrahedra. Studies have shown that in the silicate glass for instance, most of the high frequency vibrations are due to the stretching of the Si-O bond^{6,7,8,9}. Since we are only considering localized vibrations, the wavefunctions will be enumerated by frequency only and not by wave number k . So our picture can be described as either as a unit cell surrounding the rare-earth ion (crystal) or large molecule of network forming units surrounding rare-earth ion (glass). There will be many modes of lattice oscillations that can couple to the ion. However in the final expression, we will show that in most cases, only the normal mode with the highest frequency of vibration (ν_{eff}) efficiently couples to the rare-earth ion during a nonradiative transition in both glassy and crystalline host materials.

Let us first consider the one phonon transition. Later we will invoke high order perturbation theory to describe a multiphonon transition. We are interested in the transition from an initial state $|\varphi_i\rangle$ to a final state $\langle\varphi_f|$ with the emission of a single phonon. The wave function can be written as:

$$|\varphi_i\rangle = |\psi_i^{\text{el}}\rangle \prod_{\omega_k=1}^{k'=m} |n_{\omega_k}\rangle \quad (16)$$

and

$$\langle \Phi_f | = \langle \Psi_f^{el} | \langle n_{\omega_k} + 1 | \prod_{\omega_{k'} \neq k}^{k'=m} \langle n_{\omega_{k'}} | \quad (17)$$

where in the final state, one of the phonon occupation numbers has increased by one. Substituting the above wavefunctions into Eqn. 12 we find:

$$W_{nr}^1 = \frac{2\pi}{\hbar} \left| \langle \Phi_f | \sum_j \frac{\partial V_{cf}}{\partial Q_{\omega_j}} Q_{\omega_j} | \Phi_i \rangle \right|^2 \rho(E) \quad (18)$$

where we have only considered the first term in the dynamic crystal field expansion. Recall from the quantum mechanical description of a harmonic oscillator that the normal coordinate, Q_{ω} , can be written as a sum of the creation and annihilation operators:

$$Q_{\omega} = \sqrt{\frac{\hbar}{2M\omega}} (\hat{a}_{\omega}^+ + \hat{a}_{\omega}) \quad (19)$$

where

$$\hat{a}_{\omega}^+ |n_{\omega}\rangle = \sqrt{n_{\omega} + 1} |n_{\omega} + 1\rangle \quad (20)$$

and

$$\hat{a}_{\omega} |n_{\omega}\rangle = \sqrt{n_{\omega}} |n_{\omega} - 1\rangle \quad (21)$$

Therefore, Eqn. 18 becomes:

$$W_{nr}^1 = \frac{2\pi}{\hbar} \left| \langle \Psi_f^{el} | \frac{\partial V_{cf}}{\partial Q_{\omega_k}} | \Psi_i^{el} \rangle \right|^2 \frac{\hbar}{2M\omega_k} (n_{\omega_k} + 1) \delta[E_i - E_f - \hbar\omega_k] \quad (22)$$

where the density function has been replaced by the energy conserving delta function. Since the details of the electronic coupling of the rare-earth ion to the lattice is not well known, the squared matrix element cannot be directly calculated. As a result, in the final expression, the matrix element is usually left as a phenomenological parameter.

Since most nonradiative transitions involve energy separations between the initial and final state which are larger than the highest single phonon energy in the glass or crystal, we must proceed to a higher order perturbation calculation to account for the possibility of multiphonon emission. Expanding the expression for the dynamic crystal field potential we find:

$$H_{dyn} = \sum_{i=1}^m \frac{\partial V_{cf}}{\partial Q_{\omega_i}} Q_i + \sum_{i,j=1}^m \frac{\partial^2 V_{cf}}{\partial Q_{\omega_i} \partial Q_{\omega_j}} Q_{\omega_i} Q_{\omega_j} + \dots \sum_{i,j,\dots,p=1}^m \frac{\partial^p V_{cf}}{\partial Q_{\omega_i} \partial Q_{\omega_j} \dots \partial Q_{\omega_p}} Q_{\omega_i} Q_{\omega_j} \dots Q_{\omega_p} \quad (23)$$

Where the sum is over all modes of vibration that can couple to the rare-earth ion during the transition. In calculating nonradiative transition rates for higher order processes, we can use the first term in p th order perturbation or the p th order term in first order perturbation. Both arguments should lead to similar results and therefore for simplicity we chose to use the first term in the expression below which includes a sum over all the possible intermediate states φ_{s_i} ¹⁰:

$$W_{nr}^p = \frac{2\pi}{\hbar} \sum_{s_1, \dots, s_{p-1}} \frac{\left\langle \varphi_f \left| \sum_{i=1}^m \frac{\partial V_{cf}}{\partial Q_{\omega_i}} Q_{\omega_i} \right| \varphi_{s_1} \right\rangle \left\langle \varphi_{s_1} \left| \sum_{j=1}^m \frac{\partial V_{cf}}{\partial Q_{\omega_j}} Q_{\omega_j} \right| \varphi_{s_2} \right\rangle \dots \left\langle \varphi_{s_{p-1}} \left| \sum_{k=1}^m \frac{\partial V_{cf}}{\partial Q_{\omega_k}} Q_{\omega_k} \right| \varphi_i \right\rangle^2}{(E_i - E_{s_1})(E_{s_1} - E_{s_2}) \dots (E_{s_{p-1}} - E_i)} \rho(E) \quad (24)$$

The mathematical details for simplifying this expression are discussed in Ref. 5. We show the final result below:

$$W_{nr}^p = \frac{2\pi}{\hbar} \left[\frac{\hbar}{2M\omega} (n+1) \right]^p \frac{(2m)^{2p}}{4} \frac{\left\langle \psi_f^{el} \left| \overline{V}_{cf} \right| \psi_i^{el} \right\rangle^{2p}}{(\hbar\omega)^{2(p-1)}} \delta(\Delta E_{gap} - p \cdot \hbar\omega) \quad (25)$$

and

$$p = \frac{\Delta E_{gap}}{\hbar\omega} \quad (26)$$

where p is the normalized energy gap or order of the multiphonon process. The expression in the square bracket arose from the operator Q_{ω} operating on the lattice wavefunctions p times. The average matrix element $\left\langle \psi_f^{el} \left| \overline{V}_{cf} \right| \psi_i^{el} \right\rangle$ arises from assuming that the details of the ion-lattice coupling are unimportant since they become statistically averaged for a multiphonon process. The work by Kiel¹¹ cast Eqn. 25 into a simpler form by assuming that if the perturbation \overline{V}_{cf} is small, then the transition rate for a p th order process should be smaller than for a $(p-1)$ th order process. The argument is shown mathematically as follows:

$$\begin{aligned}
\frac{W_{nr}^p}{W_{nr}^{p-1}} &= \varepsilon \ll 1 \\
W_{nr}^p &= W_{nr}^{p-1} \varepsilon \\
W_{nr}^{p-1} &= W_{nr}^{p-2} \varepsilon^2 \\
&\vdots \\
W_{nr}^p &= W_{nr}^0 \varepsilon^p
\end{aligned} \tag{27}$$

where ε can be found from Eqn. 25 to be:

$$\varepsilon = \left[\frac{\hbar}{2M\omega} (n+1) \right] \cdot (2m)^2 \cdot \frac{\left| \langle \varphi_f | \bar{V}_{cf}' | \varphi_i \rangle \right|^2}{(\hbar\omega)^2} \tag{28}$$

The nonradiative rate can be rewritten as:

$$W_{nr}^p = A \varepsilon^p = A \exp(\ln \varepsilon \cdot p) = A \exp(-\kappa p) \tag{29}$$

or bringing out the temperature dependence in front we have

$$W_{nr}^p = A \cdot (n+1)^p \cdot \exp(\ln \varepsilon' \cdot p) \tag{30a}$$

$$\varepsilon' = \frac{\hbar(2m)^2}{2M\omega} \cdot \left(\frac{\left| \langle \varphi_f | \bar{V}_{cf}' | \varphi_i \rangle \right|^2}{\hbar\omega} \right) \tag{30b}$$

where the Bose-Einstein occupation number is defined as:

$$n = \frac{1}{\exp(\hbar\omega/kT) - 1} \tag{31}$$

Eqn. 29 can be recognized as the energy gap law. In arriving at this final form, we have assumed that the average matrix element $\left| \langle \varphi_f | \bar{V}_{cf}' | \varphi_i \rangle \right|^2$ is the same for: (1) a p th and a $(p-1)$ th order process, (2) for different initial and final electronic states, and (3) different temperatures. In assuming that the initial and final state are unimportant, the expression predicts that the nonradiative rates for different transitions will be similar, so long as the gap sizes are equivalent. In addition, the dependence on p implies that only the highest frequency vibrations ($\hbar\omega = \hbar\omega_{\text{eff}}$) are important. This has been shown to be generally true through temperature dependent measurements⁵ of the nonradiative rates where the data is fit to a single value of $\hbar\omega_{\text{eff}}$. Recall from **Figure 4.7** that the nonradiative transition tends

to involve high frequency phonons since the energy gap can be bridged with the smallest number of phonons and with the lowest order perturbation treatment. In **Figures 5.3 and 5.4** we plot the nonradiative rate (W_{nr}) as a function of the energy gap (ΔE_{gap}) for several data at room temperature. As is evidenced by the linear fits, the energy gap law appears to be valid for all of the materials investigated thus giving confidence to the phenomenological expression of Eqn. 29.

5.3 Derivation of energy transfer model

It is the purpose of this section to discuss an alternative method for calculating the nonradiative transition rates by employing a modified expression from energy transfer theory. We will show that the modified expression is primarily dependent on the absorption of the host material and thus allows a simple measurement of the host absorption coefficient to be used for an estimate of the nonradiative transition rates. The Foerster-Dexter^{12,13} theory for energy transfer has been successfully used to model systems in which energy is transferred from a donor impurity-ion to an acceptor impurity-ion within the same host medium. For example, in some lasers systems, two rare-earth ions are co-doped into the host. In a paper by Payne et al.^{14a} the rare-earth ions of Tm^{3+} and Ho^{3+} were co-doped into $LiYF_4$ to produce a laser in the 2.1 μm range. In this scheme, the Tm^{3+} ion is used to efficiently absorb the pump light and efficiently transfer the energy to the Ho^{3+} ion through nonradiative energy transfer. After which, the Ho^{3+} ion emits radiation at the desired wavelength. In this model, the distribution of acceptor molecules is considered to be random and the concentration is often very low. The total rate of de-excitation for the donor can be written as:

$$W_{tot}^D = W_{rad}^D + W_{nr}^{xfer} \quad (32)$$

where the first term is the radiative rate and the second term corresponds to the nonradiative rate of energy transfer between the donor and acceptor. The intensity of the luminescence of the donor can therefore be written as:

$$I^D = I_o^D \exp(-W_{tot}^D \cdot t) \quad (33)$$

In our physical model, the RE-ion is the donor and the surrounding host acts as the acceptor ions (**Figure 5.5**). The acceptor ions, for example, could be the high frequency SiO₄ network formers within the silicate glass. As mentioned earlier there has been evidence that the high frequency vibrations of the SiO₄ complexes responsible for absorbing the energy from the Nd ions⁵. From this description we find that there is a functional dependence on the distance between the donor and the acceptor, R_k. We can write the energy transfer rate as a sum of probabilities:

$$W_{nr}^{xfer} = \sum_{k=1}^{k=N_A} P(R_k) \quad (34)$$

where N_A is the number of acceptors. The intensity can now be written as:

$$I^D = I_o^D \exp\left(-W_{rad}^D + \sum_{k=1}^{k=N_A} -P(R_k)\right) \cdot t \quad (35)$$

or in product form:

$$I^D = I_o^D \exp(-W_{rad}^D \cdot t) \prod_{k=1}^{k=N_A} \exp(-P(R_k) \cdot t) \quad (36)$$

In order to calculate the energy transfer rate, we must derive a functional form for the nonradiative rate, P(R). Following the Foerster-Dexter theory, a dipole-dipole interaction Hamiltonian is used within the time-dependent perturbation expression:

$$P(R) = \frac{2\pi}{\hbar} \left| \int \Psi_F^* H_{int} \Psi_I d\tau \right|^2 \rho(E) \quad (37)$$

The dipole-dipole interaction Hamiltonian can be written in MKS units as:

$$H_{int} = \frac{1}{4\pi\epsilon_0} \frac{1}{R^3} \left[\vec{p}_1 \cdot \vec{p}_2 + 3(\vec{p}_1 \cdot \hat{R})(\vec{p}_2 \cdot \hat{R}) \right] \quad (38)$$

where R is defined as the distance between the dipoles as shown in **Figure 5.6**.

The wavefunctions of the initial and final states can be decomposed as:

$$\Psi_I = \Psi_D' \Psi_A \quad (39)$$

and
$$\Psi_F = \Psi_D \Psi_A' \quad (40)$$

where initially, the donor is in an excited state and the acceptor is in the ground state, and in the final state, the donor is in the ground state and the acceptor is in the excited state. A prime is used to designate an excited state.

After simplifying, (Ref. 12, 13, and 14b) we have:

$$P(R) = \left[\frac{R_0}{R} \right]^6 \cdot \frac{1}{\tau_{\text{rad}}} \quad (41)$$

where

$$[R_0]^6 = \left(\frac{3}{4\pi} \right) \left(\frac{\hbar c}{n} \right)^4 \int \frac{F^D(E') \sigma^A(E') dE'}{E'^4} \quad (42)$$

or

$$[R_0]^6 = \left(\frac{3c\tau_{\text{rad}}}{8\pi^4 n^2} \right) \int \sigma_{\text{em}}^D(\lambda') \sigma_{\text{abs}}^A(\lambda') d\lambda' \quad (43)$$

Equation 43 is an important simplification within the derivation. It states that the nonradiative energy transfer rate is dependent on the overlap integral of the donor emission cross section, σ_{em} and the acceptor absorption cross section, σ_{abs} . Intuitively this makes sense, since if the energy of the donor ion is not in resonance with what the acceptor ion can internally absorb, then the probability of energy transfer between the two ions will be low.

Returning to Eqn. 35, we convert the discrete sum into an integral

$$I^D = I_0^D \exp \left(-W_{\text{rad}}^D - N_A \int_V P(R) w(R) dV \right) \cdot t \quad (44)$$

where $w(R)$ is the probability distribution of the donor-acceptor distance R in the volume, V ¹⁵.

$$I^D = I_0^D \exp \left(-W_{\text{rad}}^D - N_A \int_{R_{\text{min}}}^{\infty} P(R) \frac{4\pi R^2}{V} dR \right) \cdot t \quad (45)$$

and

$$V = \frac{4}{3} \pi R^3 \quad (46)$$

Our system differs in one important way in that the concentration of the acceptors is much higher. This requires us to use a slightly different method of averaging as shown in Eqns. 44 and 45 from that normally done for low concentrations¹⁵. The low concentration model¹⁵ employs a statistically weighted average of the product form shown in Eqn. 36.

In both derivations, (this work and Ref. 15) a parameter, R_{min} , is introduced in the lower limit of the integral so that the integrand is convergent over the limits of integration. The R_{min} parameter in our model can be considered the minimum interaction

distance over which Hamiltonian still appears as a dipole-dipole interaction. Substituting the definition for $P(R)$ from Eqn. 41 into Eqn. 45 we have:

$$I^D = I_0^D \exp\left(-W_{\text{rad}}^D - N_A \int_{R_{\text{min}}}^{\infty} \left[\frac{R_0}{R}\right]^6 \frac{1}{\tau_{\text{rad}}} \frac{4\pi R^2}{V} dR\right) \cdot t \quad (47)$$

which integrates to:
$$I^D = I_0^D \exp\left(-W_{\text{rad}}^D - \frac{N_A}{V} \frac{4/3 \pi R_0}{R_{\text{min}}^3 \tau_{\text{rad}}}\right) \cdot t \quad (48)$$

Finally we have:

$$I^D = I_0^D \exp\left(-W_{\text{rad}}^D - \frac{N_A}{V} \frac{4/3 \pi}{R_{\text{min}}^3} \frac{3c}{8\pi^4 n^2} \int \sigma_{\text{em}}^D(\lambda') \sigma_{\text{abs}}^A(\lambda') d\lambda'\right) \cdot t \quad (49)$$

The acceptor concentration is defined as the number of acceptors divided by the volume

$$\rho_A = \frac{N_A}{V} \quad (50)$$

In addition, the absorption coefficient can be defined in terms of the acceptor concentration and the acceptor cross section as:

$$\alpha_{\text{abs}}^A = \rho_A \sigma_{\text{abs}}^A \quad (51)$$

The integral in Eqn. 49 now becomes:

$$I^D = I_0^D \exp\left(-W_{\text{rad}}^D - \frac{4/3 \pi}{R_{\text{min}}^3} \frac{3c}{8\pi^4 n^2} \int \sigma_{\text{ems}}^D(\lambda') \alpha_{\text{abs}}^A(\lambda') d\lambda'\right) \cdot t \quad (52)$$

or
$$I^D = I_0^D \exp\left(-W_{\text{rad}}^D - \frac{1}{V_{\text{min}}} \frac{2/3c}{(\pi n)^2} \int \sigma_{\text{ems}}^D(\lambda') \alpha_{\text{abs}}^A(\lambda') d\lambda'\right) \cdot t \quad (53)$$

where V_{min} has been described by Kaminskii¹⁶ as the smallest non absorbing volume surrounding the rare-earth ion.

Since the details of the cross sections for infrared emission are often unknown we will approximate the emission cross section with an effective cross section defined as a delta function multiplied by a slowly varying function of λ . We know from our derivation of the energy gap law and the experimental data in **Figures 5.3 and 5.4** (summarized in **Table 5.1**) that the nonradiative transition rates appear to be invariant of the particular details of the initial and final electronic states of the rare-earth ion (Some exceptions have

been noted, see Ref. 17) Continuing with this approximation, we explore the possibility of rewriting the nonradiative transition rate from Eqn. 53 as:

$$W_{nr}^{xfer} = \frac{1}{V_{min}} \frac{2/3c}{(\pi n)^2} \int \delta(\lambda - \lambda') \cdot \tilde{\chi} \cdot \alpha_{abs}^A(\lambda') d\lambda' \quad (54)$$

$$\text{with} \quad \sigma_{ems}^D(\lambda') = \delta(\lambda - \lambda') \cdot \tilde{\chi} \quad (55)$$

where $\tilde{\chi}$ is the slowly varying function of the emission wavelength in the infrared region of interest here. The nonradiative transition rate can therefore be written in terms of the host absorption coefficient α_{abs}^{host} :

$$W_{nr}^{xfer} = \frac{1}{V_{min}} \frac{2/3c}{(\pi n)^2} \cdot \tilde{\chi} \cdot \alpha_{abs}^{host}(\lambda) \quad (56)$$

In reviewing the literature, we found several experimental data that showed an exponential dependence on the logarithm of the absorption coefficient with energy of the absorption wavelength^{18,19}. In addition, we found that several of the theoretical formulas used to describe the experimental data had a similar dependence on the energy gap as that of the energy gap law^{18,19,20(a-d)}. The question underlying many of the derivations is whether to use an anharmonic approximation for the lattice wavefunctions with the linear dipole as the interaction Hamiltonian between the host and the radiation field²¹:

$$\alpha_{abs}^{host} \propto \left| \left\langle \varphi_{tot}^f | D_{lin} | \varphi_{tot}^i \right\rangle \right|^2 \rho(E) \quad (57a)$$

$$H_{tot} = H_{harm} + H_{anh} \quad (57b)$$

or to allow the dipole interaction to include the higher order nonlinear terms²²

$$\alpha_{abs}^{host} \propto \left| \left\langle \varphi_{tot}^f | D | \varphi_{tot}^i \right\rangle \right|^2 \rho(E) \quad (58a)$$

$$D = D_{lin} + D_{nonlinear} \quad (58a)$$

In all probability, the answer involves both effects of mechanical anharmonicity (H_{anh}) and electrical anharmonicity ($D_{nonlinear}$). In reviewing the literature we found a derivation which assumed the conditions of Eqns. 57 a and b¹⁹. The final expression from this work appears as:

$$\alpha_{abs}^{host} \propto B(n+1)^{p'+1} \exp(\ln \beta \cdot p') \quad \text{where } p' = \frac{\omega}{\omega_0} > 1 \quad (59)$$

where β describes the strength of the anharmonicity. It is also used in the expansion of the anharmonic crystal. The frequency ω_0 is defined as the Reststrahl frequency. In other similar derivations, ω_0 is defined as the maximum critical frequency^{20a} or characteristic longitudinal optical frequency of the material¹⁸. And therefore p' defines the p' th order of the absorption process. Using the above definition for the absorption coefficient, we can rewrite the nonradiative transition rate of Eqn. 56 as:

$$W_{nr}^{xfer} \cong \tilde{B} \cdot (n+1)^{p'+1} \exp(\ln\beta \cdot p') \quad (60a)$$

where

$$\tilde{B} = B \cdot \frac{1}{V_{min}} \frac{2/3c}{(\pi n)^2} \cdot \tilde{\chi} \quad (60b)$$

5.4 Applicability of energy transfer model for predicting nonradiative transition rates and conclusions

In comparing the final expressions from both the energy gap law and energy transfer theory, we observe some similarities between the two expressions. We summarize the results in Eqns. 61 and 62 below:

$$W_{nr}^p = A \cdot (n(\hbar\omega_{eff}) + 1)^p \cdot \exp(\ln \varepsilon' \cdot p) \quad \text{“Energy Gap Law”} \quad (61a)$$

with

$$\varepsilon' = \frac{\hbar(2m)^2}{2M\omega} \cdot \left(\frac{|\langle \phi_f | \nabla' | \phi_i \rangle|}{\hbar\omega} \right)^2 \quad (61b)$$

and

$$p = \frac{\Delta E_{gap}}{\hbar\omega_{eff}} \quad (61c)$$

$$W_{nr}^{xfer} \propto \alpha_{abs}^{host}(\lambda) \quad (62a)$$

or

$$W_{nr}^{xfer} \cong \tilde{B} \cdot (n(\hbar\omega_0) + 1)^{p'+1} \exp(\ln\beta \cdot p') \quad \text{“Energy Transfer Model”}$$

with

$$p' = \frac{\Delta E_{gap}}{\hbar\omega_0} \quad (62b)$$

We observe that the slopes of the $\log(W_{nr})$ and $\log(W_{nr}^{xfer})$ curves when plotted against the energy gap (ΔE_{gap}) both depend on the strength of the perturbation. In the case of energy transfer, $\ln\beta$ is a parameter that describes the degree of anharmonicity of the harmonic potential. In a similar fashion, the slope $\ln\varepsilon'$ of the energy gap expression is

related to the strength of the ion-lattice coupling. In both derivations, the order of the perturbation process (p and p') is important and leads to similar exponential dependencies on the energy gap (ΔE_{gap}) of the transition.

If we plot the nonradiative rate (W_{nr}) versus the absorption coefficient ($\alpha_{\text{abs}}^{\text{host}}$) on a log-log plot as shown in **Figure 5.7** we find that the data appear to follow a nearly linear relationship. Due to the lack of infrared absorption available for many of the materials we investigated, we were only able to plot data for the following crystals: Nd:YAG, Nd:YALO, and Nd:YLF. The absorption data was found from Ref. 29-31 respectively, and the nonradiative rates were taken from the plots in **Figures 5.3 and 5.4**. The best fit to the data yielded:

$$\log(W_{\text{nr}}) = 1.21 \cdot \log(\alpha_{\text{abs}}) + 7.06 \quad (63)$$

or

$$W_{\text{nr}} = 10^{7.06} \cdot \alpha_{\text{abs}}^{1.21} \quad (64)$$

where Eqns. 61 and 62 predict a $\alpha_{\text{abs}}^{1.0}$ dependence.

Due to the nearly linear dependence of the data, our initial approximation of estimating the emission cross section with an effective cross section appears to agree with the results. This small discrepancy implies that the Foerster-Dexter formalism for energy transfer may not strictly apply to our model. In addition to this work, there have been many other attempts to correlate nonradiative transitions with absorption data (For example see Refs. 24, 29, 31, and 33). The manuscript of Kaminskii et al.¹⁶ includes many references to the important early works of E. B. Sveshnikova, V. L. Ermolaev and others in correlating nonradiative transitions with inductance-resonance theory and in addition, provides a thorough review of the previous work done. In this chapter, we have attempted to bring some of the available information together in a single plot. With the availability of additional absorption data, a plot similar to **Figure 5.7** could prove useful, since the measurements of the absorption coefficient are significantly easier than nonradiative measurements. Order of magnitude estimates could then easily be made for prospective, new laser materials.

Table 5.1 A summary of the slopes and y-intercepts for the best fit through the data in Figures 5.3 and 5.4

Material	Slope 10^{-3}	y-intercept
Phosphate Glasses	-2.02	12.63
Silicate Glasses	-1.85	11.56
ZBLAN and ZBLN	-3.32	11.62
YLF	-2.76	11.26
YAG	-2.29	11.98
YALO	-2.92	12.68
GSGG and GGG	-3.12	12.74
YVO ₄	-2.41	12.65

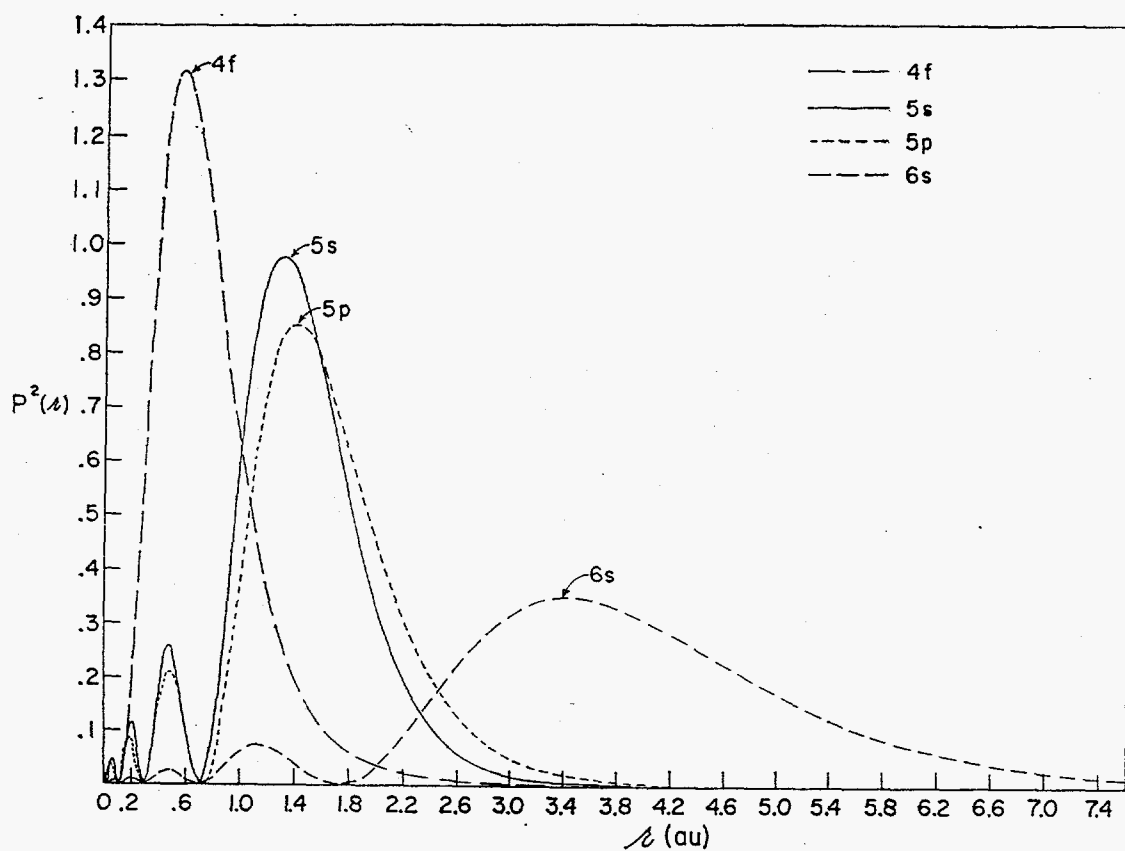


Figure 5.1 A plot of the radial orbitals for Gd^+ showing the shielding of the electrons in the $4f^N$ orbital by the closed shell $5s^2$ and $5p^6$ orbitals (From Ref. 32).

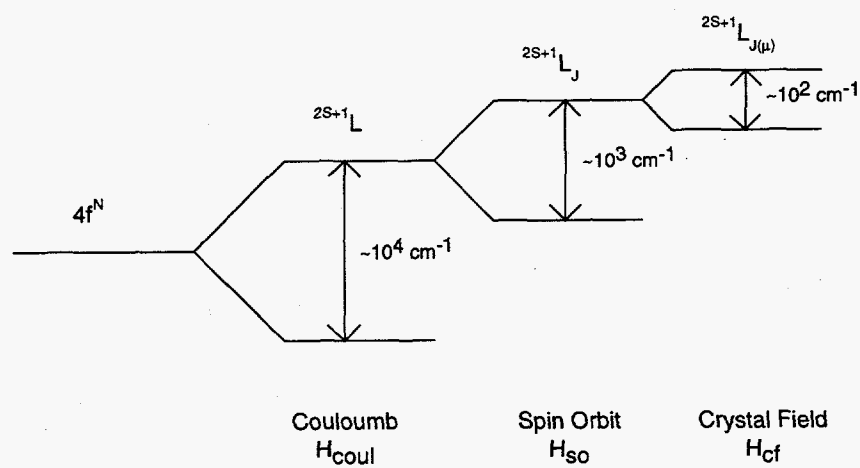


Figure 5.2 Due to the outer orbital shielding, the crystal field surrounding the rare-earth ion can be treated as a perturbation on the free ion states in calculating the new wavefunctions and energy levels.

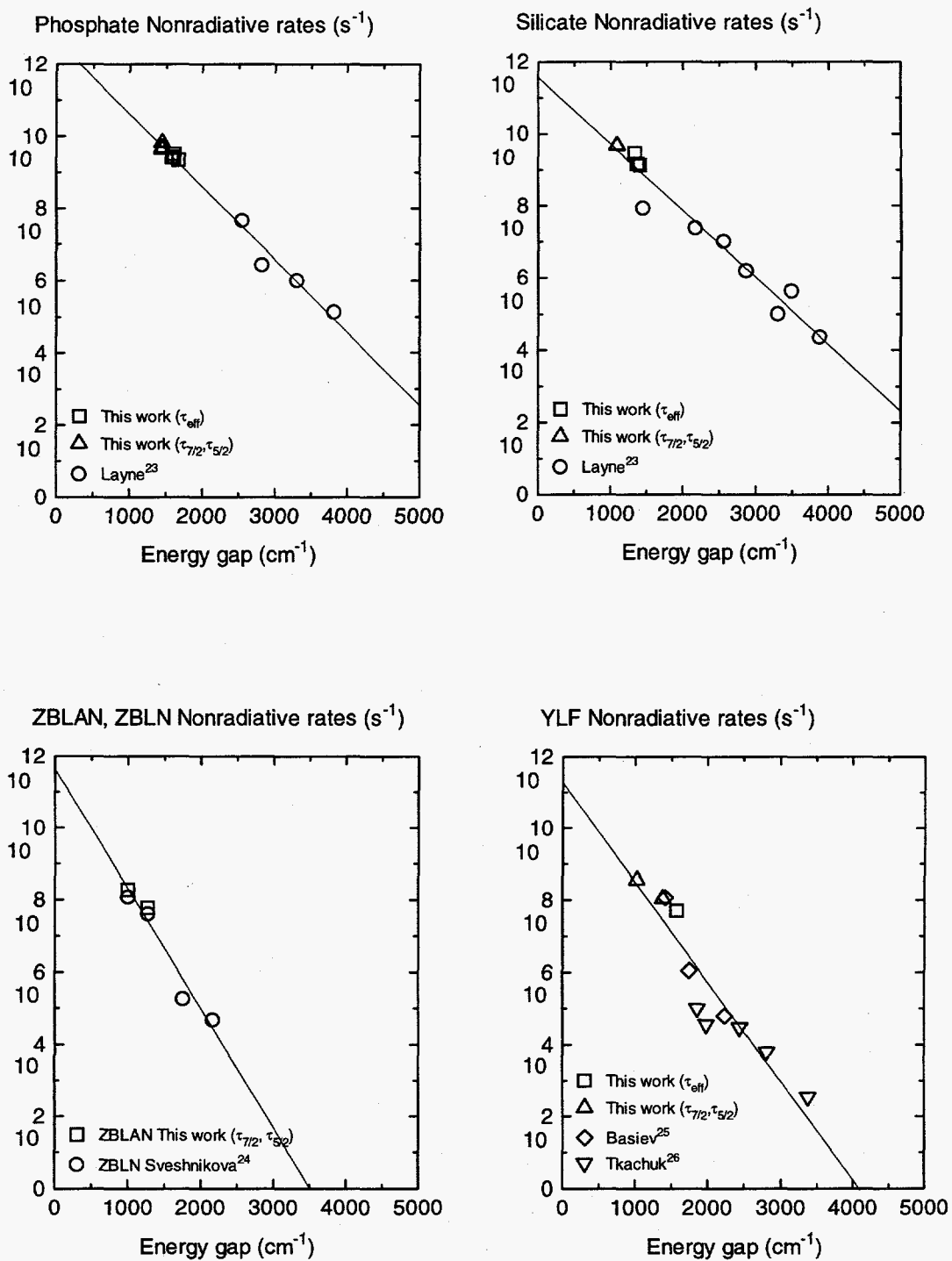


Figure 5.3 A plot of the nonradiative rate versus energy gap for the phosphate, silicate, and fluorides glasses and a fluoride crystal at room temperature. The best fit through the data is shown by the solid line.

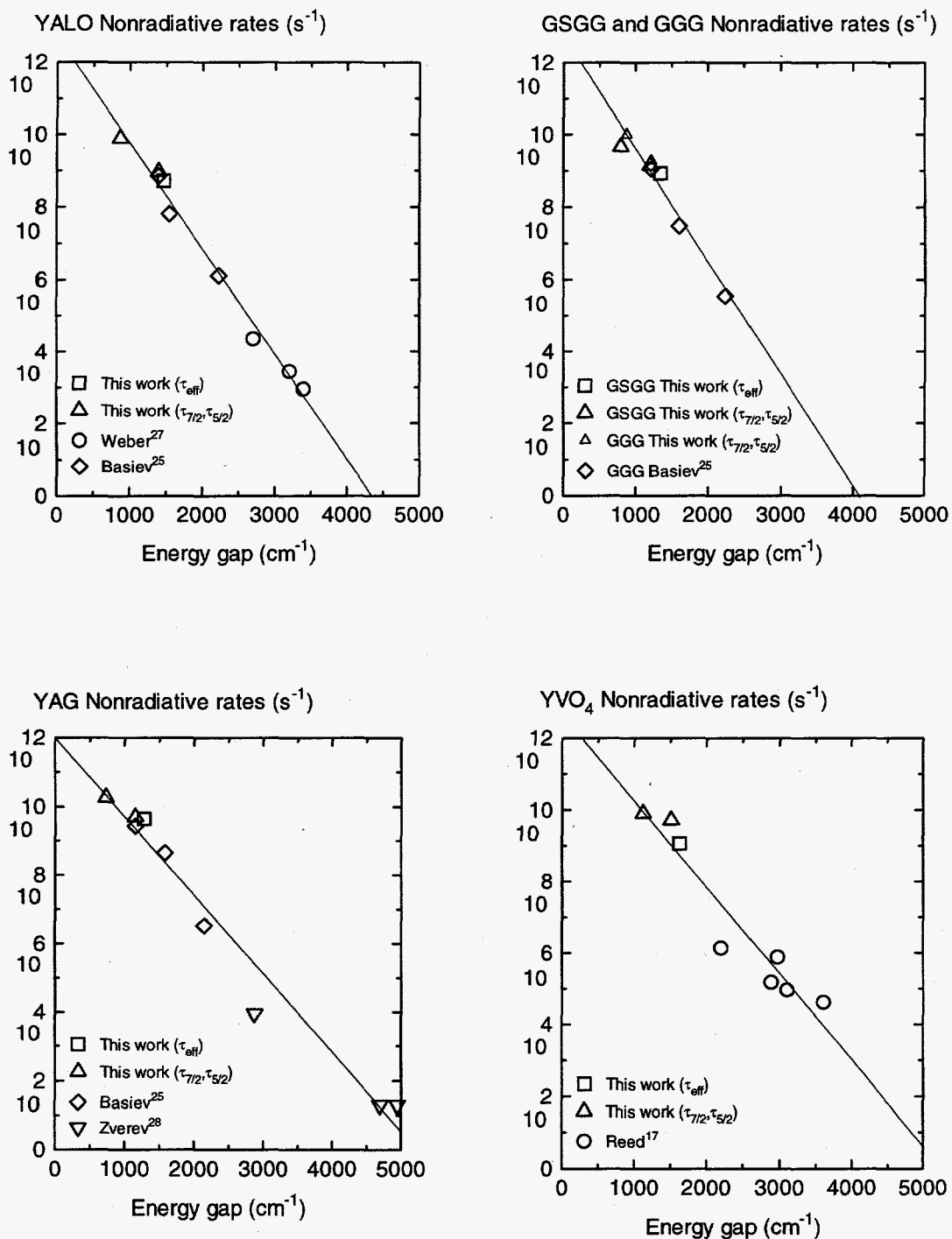


Figure 5.4 A plot of the nonradiative rate versus energy gap for three oxide crystals and a vanadate crystal at room temperature. The best fit through the data is shown by the solid line.

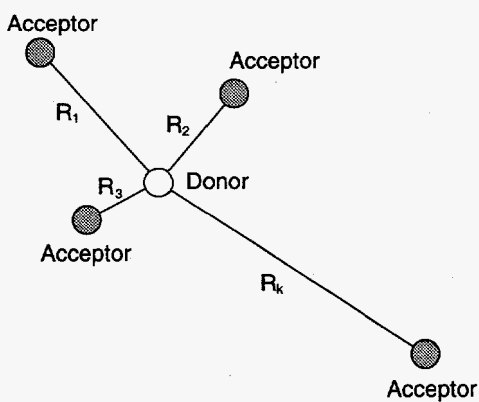


Figure 5.5 In our model, the rare-earth ion is considered to be the donor and the surrounding unit cell in the crystalline lattice or network forming ions in a glass are considered to be the acceptors.

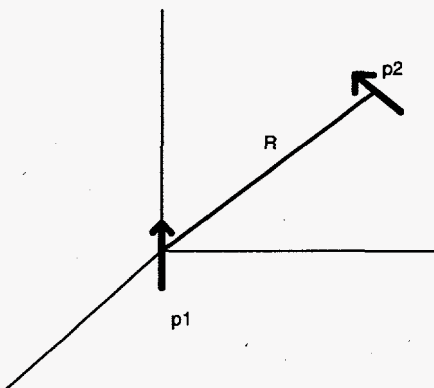


Figure 5.6 In a dipole-dipole interaction, the interaction distance is defined to be R .

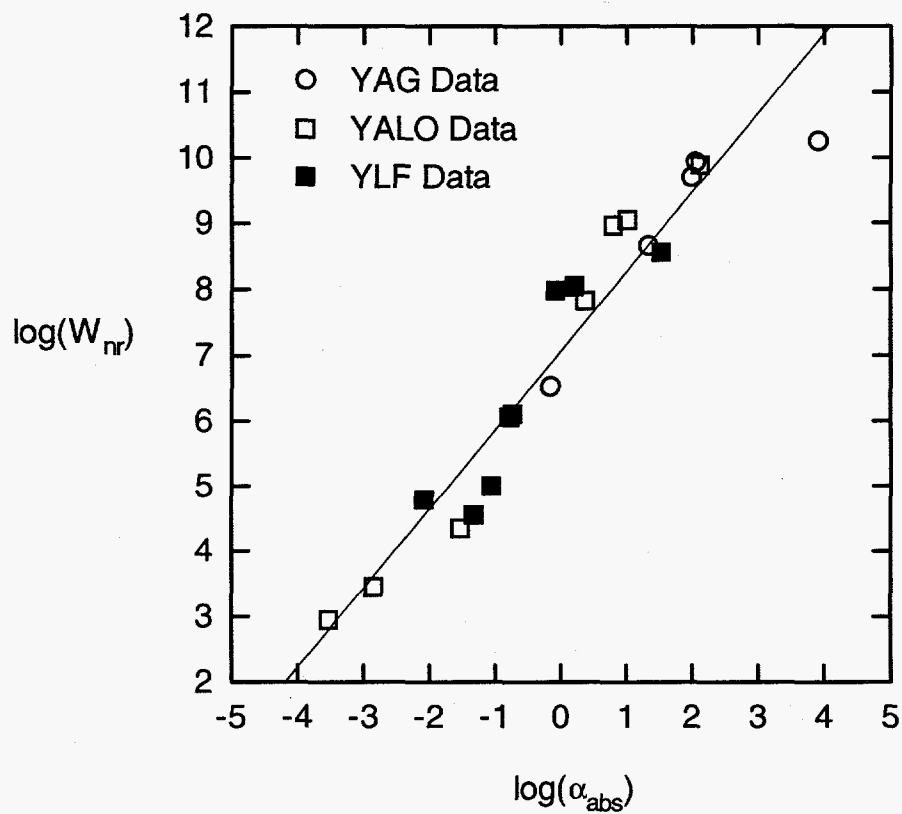


Figure 5.7 A logarithmic plot of the nonradiative transition rate (W_{nr}) versus host absorption coefficient (α_{abs})

Chapter 5 References

- ¹A. A. Kaminskii, *Laser Crystals, Their Physics and Properties*, Springer-Verlag, (1990).
- ²M. Weissbluth, *Atoms and Molecules*, Academic Press, (1978).
- ³B. R. Judd, "Optical absorption intensities of rare-earth ions," *Phys. Rev* **127**, 750 (1962).
- ⁴G. S. Ofelt, "Intensities of crystal spectra of rare-earth ions," *J. of Chem. Phys.* **37**, 511 (1962).
- ⁵C. B. Layne, "Multiphonon relaxation and excitation transfer in rare-earth doped glasses," Ph.D. thesis, University of California, Davis (1975).
- ⁶(a)R. J. Bell and P. Dean, "Properties of vitreous silica: analysis of random network models," *Nature* **212**, 1354 (1966).
- (b)R. J. Bell, N. F. Bird, and P. Dean, , "The vibrational spectra of vitreous silica, germania, and beryllium fluoride," *J. Phys. C.* **1**, 299 (1968).
- ⁷J. Bock and G. J. Su, "Interpretation of the infrared spectra of fused silica," *J. Am. Ceram. Soc.* **53**, 69 (1970).
- ⁸N. F. Borrelli and G. J. Su, "An interpretation of the infra-red spectra of vitreous boron oxide," *Phys. Chem. Glasses* **4**, 206 (1963).
- ⁹J. B. Bates, "Dynamics of β -quartz structures of vitreous SiO_2 and BeF_2 ," *J. Chem. Phys.* **56**, 1910 (1972).
- ¹⁰W. Heitler, *The Quantum Theory of Radiation*, Clarendon Press, (1954).
- ¹¹A. Kiel, "The interaction of paramagnetic ions with lattice vibrations," Ph.D. thesis Johns Hopkins University, Baltimore MD. (1962).
- ¹²T. Foerster, *Z. Naturforsch.* **49**, 321 (1949).
- ¹³D. L. Dexter, "A theory of sensitized luminescence in solids," *J. Chem. Phys.* **21**, 836 (1953).
- ¹⁴a)S. A. Payne, L. K. Smith, W. L. Kway, J. B. Tassano, and W. F. Krupke, "The mechanism of $\text{Tm} \rightarrow \text{Ho}$ energy transfer in LiYF_4 ," *J. Phys. Condens. Matter* **4**, 8525 (1992).
- b)S. A. Payne and L. L. Chase, " $\text{Sm}^{2+} \rightarrow \text{Nd}^{3+}$ energy transfer in CaF_2 ," *J. Opt. Soc. Am. B* **3**, 1181 (1986).
- ¹⁵M. Inokuti and F. Hirayama, "Influence of energy transfer by the exchange mechanism on donor luminescence," *J. Chem. Phys.* **43**, 1978 (1965).
- ¹⁶A. A. Kaminskii et al., *Physics and Spectroscopy of Laser Crystals*, Izdatelstvo, "Nauka" (1986).
- ¹⁷E. D. Reed Jr., and H. W. Moos, "Multiphonon relaxation of excited states of rare-earth ions in YVO_4 , YAsO_4 , and YPO_4 ," *Phys. Rev. B* **8**, 980 (1973).
- ¹⁸T. F. Deutch, "Absorption coefficient of infrared laser window materials," *J. Phys. Chem. Solids* **34**, 2091 (1973).
- ¹⁹T. C. McGill, R. W. Hellwarth, M. Mangir, and H. V. Winston, "Infrared absorption in ionic insulators due to multiphonon processes," *J. Phys. Chem. Solids* **34**, 2105 (1973).
- ²⁰a)M. Sparks and L. J. Sham, "Exponential frequency dependence of multiphonon-summation infrared absorption," *Solid State Comm.* **11**, 1451 (1972).

- b) D. L. Mills and A. A. Maradudin, "Theory of infrared absorption by crystals in the high-frequency wing of their fundamental lattice absorption," *Phys. Rev. B* **8**, 1617 (1973).
- c) L. J. Sham and M. Sparks, "Explicit exponential frequency dependence of multiphonon infrared absorption," *Phys. Rev. B* **9**, 827 (1974).
- d) L. L. Boyer, J. A. Harrington, M. Hass, and H. B. Rosenstock, "Multiphonon absorption in ionic crystals," *Phys. Rev. B* **11**, 1665 (1975).
- ²¹B. Bendow, S. Ying, and S. P. Yukon, "Theory of multiphonon absorption due to anharmonicity in crystals," *Phys. Rev. B* **8**, 1679 (1973).
- ²²B. Bendow, S. P. Yukon, and S. Ying, "Theory of multiphonon absorption due to nonlinear electric moments in crystals," *Phys. Rev. B* **10**, 2286 (1974).
- ²³C. B. Layne, W. H. Lowdermilk, and M. J. Weber, "Multiphonon relaxation of rare-earth ions in oxide glasses," *Phys. Rev. B* **16**, 10 (1977).
- ²⁴E. B. Sveshnikova, A. A. Stroganov, and L. N. Urusovskaya, "Mechanism of nonradiative transitions in rare-earth ions in fluorozirconate bases," *Opt. Spectrosc. (USSR)* **63**, 618 (1987).
- ²⁵T. T. Basiev, A. Y. Dergachev, Y. V. Orlovskii, and A. M. Prokhorov, "Multiphonon nonradiative relaxation from high-lying levels of Nd³⁺ ions in fluoride and oxide laser materials," *OSA Proceedings on Advanced Solid-State Lasers* **10**, 358 (1991).
- ²⁶A. M. Tkachuk, A. V. Khilko, and M. V. Petrov, *Opt. Spectrosc. (USSR)*, "Probabilities for nonradiative intermultiplet transitions in the holmium ion in lithium-yttrium double fluoride crystals and stimulated emission," **58**, 216 (1985).
- ²⁷M. J. Weber, "Multiphonon relaxation of rare-earth ions in yttrium orthoaluminate," *Phys. Rev. B* **8**, 54 (1973).
- ²⁸G. M. Zverev, G. Ya. Kolodnyi, and A. M. Onishchenko, "Nonradiative transitions between levels of trivalent rare-earth ions in yttrium-aluminum garnet crystals," *Sov. Phys. - JETP* **33**, 497 (1971).
- ²⁹V. P. Gaponstev, M. R. Sirtlanov, A. K. Gromov, A. A. Isineev, "New data on nonradiative relaxation of impurity center excitations in laser materials," *Proceedings of the International Conference on Lasers '81* 763 (STS Press, McLean, 1981).
- ³⁰G. A. Slack, D. W. Oliver, R. M. Chrenko, and S. Roberts, "Optical absorption of Y₃A₁₅O₁₂ from 10 to 55,000 cm⁻¹ wave numbers," *Phys. Rev.* **177**, 1308 (1969).
- ³¹E. B. Sveshnikova, A. A. Stroganov, and N. T. Timofeev, "Role of quasilocalizable vibrations in the deactivation of rare-earth ions in fluoride bases," *Opt. Spectros. (USSR)* **64** (1), 43 (1988).
- ³²A. J. Freeman and R. E. Watson, "Theoretical investigation of some magnetic and spectroscopic properties of rare-earth ions," *Phys. Rev.* **127**, 2058 (1962).
- ³³V. Gapontsev and M. Sirtlanov, "Progress in understanding of mechanisms of RE³⁺-excited states nonradiative relaxation in crystals," *J. of Lumin.* **31&32**, 201 (1984).

Chapter 6

Pulse length and terminal level lifetime dependence of energy extraction for a Nd-doped phosphate amplifier glass

6.1 Introduction and motivation

The efficiency at which energy is extracted from a solid state laser medium will depend in part on the relative magnitude of the extraction pulse length with respect to the terminal level lifetime. Depending on the laser host material, the neodymium terminal level lifetime can vary from picoseconds to microseconds, thus influencing whether a laser will operate as a three- or four-level system. The neodymium-doped phosphate glass, LG-750 (a laser glass made by Schott and currently used in the Nova Laser Facility at Lawrence Livermore National Laboratory), operates on the basis of the ${}^4F_{3/2} \rightarrow {}^4I_{11/2}$ transition, as shown in **Figure 6.1**. During the amplification of a 1.053 μm pulse, a fraction of the inverted neodymium ion population is transferred from the ${}^4F_{3/2}$ metastable level into the ${}^4I_{11/2}$ level, which lies approximately 1500 cm^{-1} above the ground state. In this system the terminal level lifetime ($\tau_{11/2}$) is the decay time for neodymium ions in the ${}^4I_{11/2}$ level to drain into the ${}^4I_{9/2}$ ground level. If the temporal length of the extracting pulse is much longer than the terminal level lifetime ($\tau_p \gg \tau_{11/2}$) then the lower level population will quickly return to the ground state during the passage of the pulse and four-level operation will be obtained. However, for the condition of $\tau_p \ll \tau_{11/2}$, the lower level will become bottlenecked and the Nd ion population will remain in the lower level during the passage of the pulse resulting in effective three-level operation with reduced gain.

There have been several experimental and theoretical attempts to quantify the terminal level lifetime for neodymium-doped glasses and crystals: energy extraction, gain recovery, pump-probe (Chap. 2), and indirect emission (Chap. 3) for example. In principle, all of these methods should yield a similar value for the terminal level lifetime. The effort to find agreement among the various lifetime measurements is worthwhile, because the terminal level lifetime is an important parameter in the design of solid state laser systems for situations when its value becomes comparable to the laser pulse width

($\tau_{11/2} \approx \tau_p$). In this case the laser will operate as a transient quasi-three-level system and the coupled population and transport equations must be numerically integrated in order to calculate the output energy and extraction efficiency of a laser system. The numerical integration is necessary, because there is no known analytic solution to the coupled equations governing pulse amplification which explicitly includes the effects of both τ_p and $\tau_{11/2}$ in the intermediate regime.

The importance of the terminal level lifetime is evidenced by the reduction of extraction efficiency when the terminal level is fully bottlenecked. To show this, we first write the extraction efficiency in terms of the input fluence (F_{in}), output fluence (F_{out}), stored energy per unit volume (E_{stored}), and the length of the gain medium (ℓ):

$$\eta_{extr} = \frac{F_{out} - F_{in}}{\ell E_{stored}} \quad (1)$$

The stored energy density can also be described in terms of the small signal gain coefficient (g_0), the saturation fluence (F_{sat}), and a parameter γ which accounts for the upper and lower level degeneracies:

$$E_{stored} = \gamma g_0 F_{sat} \quad (2)$$

For the condition, $F_{in}/F_{sat} \gg 1$, (see Eqn. 6) we can write the output fluence in a lossless amplifier as:

$$F_{out} \cong F_{in} + F_{sat} g_0 \ell \quad (3)$$

with the saturation fluence defined as:

$$F_{sat} = \frac{h\nu/\sigma_{em}}{\gamma} \quad (4)$$

where σ_{em} is the emission cross section. We then find the limiting extraction efficiency to be:

$$\eta_{extr}(F_{in}/F_{sat} \gg 1) \cong 1/\gamma \quad (5)$$

where in the simple case of non-degenerate upper and lower laser levels, γ varies between the values of 1 and 2, representing either ideal four-level or three-level operation, respectively. In this work, we use an effective degeneracy ratio of 0.35 for Nd-doped phosphate glass. This value arises from the average of two calculations. The first is a straightforward calculation of $g_2/g_1 = (2J'+1)/(2J+1) = 1/3$ where J' and J are the total

angular momentum of the upper and lower Nd levels respectively. This value would prevail at high temperatures, where all the sublevels are equally populated. The second calculation¹ includes the thermally weighted distribution of population within the J levels and yields 0.37. If we use this effective degeneracy ratio for the upper (${}^4F_{3/2}$) and lower (${}^4I_{11/2}$) laser levels for neodymium-doped phosphate glass, LG-750, we find that the extraction efficiency can be reduced by as much as 26% in the fully bottlenecked condition.

In this chapter we formulate a modified saturation fluence, F'_{sat} , and energy extraction solution, F'_{out} , which include the effects of the pulse width and the terminal level lifetime. In Sections 6.2-6.5 we discuss our numerical modeling and present a modified saturation fluence and the conditions under which it can be used. In Section 6.6 we substitute the modified saturation fluence into the well known Frantz and Nodvik² solution for energy extraction and model the extraction data previously taken by Yarema and Milam³. Our model shows that the change in extraction efficiency between the 1 and 20 ns pulses for LG-750 laser glass can be accounted for by including the effects of the pulse width and the terminal level lifetime. In Section 6.7 we compare the terminal level lifetime determined from the extraction data with the lifetimes measured from two other experiments: a pump-probe measurement and an indirect emission measurement. We find that the values of the terminal level lifetime determined from these three separate and independent measurements are in agreement. We summarize our results and conclude that the terminal level lifetime of LG-750 is 253 ps with an RMS error of ± 50 ps.

6.2 Numerical model

The amplification of a laser pulse passing through a gain medium can be modeled by the Frantz and Nodvik² solution to the coupled rate and energy transport equations. The solutions are valid for either infinitely fast or slow terminal level lifetimes ($\tau_{11/2}$) compared with the temporal length of the pulse (τ_p) and can be used for a homogeneous and lossless medium and when the population changes are mainly due to stimulated emission and absorption processes. The Frantz-Nodvik solution which calculates the

fluence out of a gain medium given the input fluence (F_{in}), saturation fluence (F_{sat}), small signal gain (G_o), and length (ℓ) of the gain medium can be written as²:

$$F_{out} = F_{sat} \ln[1 + G_o (\exp(F_{in}/F_{sat}) - 1)] \quad (6)$$

with $G_o = \exp(g_o \ell) \quad (7)$

and $F_{sat} = \frac{h\nu/\sigma_{em}}{\gamma} \quad (8)$

where $\gamma = 1 + \frac{f_1}{f_2} \approx 1 + \frac{g_2}{g_1}$ for $\tau_p/\tau_{11/2} \ll 1$, $(9a)$

and $\gamma = 1$ for $\tau_p/\tau_{11/2} \gg 1$ $(9b)$

Here, f_1 and f_2 are the fractional populations in the lower and upper laser levels, respectively. We approximate the ratio f_1/f_2 as 0.35 given earlier for the $4F_{3/2}$ and $4I_{11/2}$ states of Nd.

In this paper, we find an empirical solution of the saturation fluence F'_{sat} similar in form to Eqn. 8, which explicitly includes the pulse length and nonradiative decay into the lower level and works in the intermediate regime ($\tau_p \sim \tau_{11/2}$). The solution is useful for calculating extraction efficiencies without having to numerically integrate the coupled equations. In forming a solution we required that it converge to the analytic Frantz-Nodvik solutions for $\tau_p/\tau_{11/2} \ll 1$ (three-level) and $\tau_p/\tau_{11/2} \gg 1$ (four-level). In reviewing Eqns. 6-9, we observe that the parameter γ changes its value in going from a three to four-level operation. Therefore, γ is changed from a constant to a variable which has an explicit functional dependence on $R = \tau_p/\tau_{11/2}$, the ratio of pulse length to terminal level lifetime:

$$\gamma(R) = 1 + \frac{g_2}{g_1} \cdot B(R) \quad (10)$$

The function $B(R)$ is to be determined with the aforementioned constraint that:

$$B(R) = 0 \text{ for } R \ll 1, \quad (11a)$$

and $B(R) = 1 \text{ for } R \gg 1 \quad (11b)$

We can now define the modified saturation fluence to be:

$$F'_{sat} = \frac{h\nu/\sigma_{em}}{\gamma(R)} \quad (12)$$

This method will give different $\gamma(R)$ curves for different pulse shapes. We give results here for near-square pulses.

6.3 Numerical computation

The steps involved in finding the functional form of $B(R)$ are: (1) Transform the coupled rate and transport equations which include the terminal level lifetime ($\tau_{11/2}$) to a coordinate system that moves within the frame of the pulse; (2) Simplify the equations by integrating over the spatial dimension so that only a set of coupled ordinary differential equations in time remain; (3) Integrate the coupled equations for a range of R values; (4) Substitute the modified saturation fluence defined in Eqn. 12 into the Frantz-Nodvik solution (Eqn. 6) and fit each of the empirical output-versus-input fluence solutions to the exact numerical solutions found in step 3 and determine $B(R)$; (5) Find an analytic form for $B(R)$; (6) Determine the range of input parameters over which the modified saturation fluence F'_{sat} can be used.

We begin by assuming that the upper laser level has a population $N_2(0)$ created by a previous pumping process when the input pulse arrives. The coupled rate and energy transport equations for a lossless system can be written as:

$$\frac{\partial N_2(t)}{\partial t} = -\frac{I(z,t)}{h\nu} [\sigma_{\text{em}} N_2(t) - \sigma_{\text{abs}} N_1(t)] \quad (13a)$$

$$\frac{\partial N_1(t)}{\partial t} = \frac{I(z,t)}{h\nu} [\sigma_{\text{em}} N_2(t) - \sigma_{\text{abs}} N_1(t)] - \frac{N_1(t)}{\tau_{11/2}} \quad (13b)$$

$$\frac{\partial I(z,t)}{\partial z} + \frac{n}{c} \frac{\partial I(z,t)}{\partial t} = I(z,t) [\sigma_{\text{em}} N_2(t) - \sigma_{\text{abs}} N_1(t)] \quad (13c)$$

where $N_2(t)$ and $N_1(t)$ represent the upper (${}^4F_{3/2}$) and lower (${}^4I_{11/2}$) level populations, σ_{em} is the single ion stimulated emission cross section for the ${}^4F_{3/2} \rightarrow {}^4I_{11/2}$ transition, and σ_{abs} is the single ion absorption cross section for the ${}^4I_{11/2} \rightarrow {}^4F_{3/2}$ transition. The intensity of the laser pulse is denoted by $I(z,t)$. In a glass, σ_{em} , σ_{abs} , and $\tau_{11/2}$ are supposed to be site averaged or ensemble values.

The equations can be transformed to a moving coordinate system that travels at the velocity of the pulse by making the following transformation of variables: $T = t - zn/c$

and $Z = z$. We also define $\beta = N_2\sigma_{em}$, to be the gain coefficient of the upper level ions and $\alpha = N_1\sigma_{abs}$, to be the loss coefficient of the lower level ions. The ratio of degeneracies is defined to be the constant $K = g_2/g_1 = \sigma_{abs}/\sigma_{ems}$. The result is:

$$\frac{\partial\beta}{\partial T} = -\frac{I}{hv/\sigma_{em}}[\beta - \alpha] \quad (14a)$$

$$\frac{\partial\alpha}{\partial T} = \frac{IK}{hv/\sigma_{em}}[\beta - \alpha] - \frac{\alpha}{\tau_{11/2}} \quad (14b)$$

$$\frac{\partial I}{\partial Z} = I[\beta - \alpha] \quad (14c)$$

These equations can be further simplified by observing that integration over the spatial dimension in Eqns. 14a, b, and c is possible, leaving a set of ordinary differential equations in time to be solved⁴. The quantities $U(t)$ and $L(t)$ are first introduced:

$$U(t) = \int_0^{\ell} \beta(z, T) dz \quad (15a)$$

and

$$L(t) = \int_0^{\ell} \alpha(z, T) dz \quad (15b)$$

Integrating the right hand side of Eqn. 14c along the length of the amplifier we find:

$$\int_{I_{in}}^{I_{out}} \frac{dI}{I} = \int_0^{\ell} (\beta - \alpha) dz = U(t) - L(t) \quad (16)$$

Completing the integration on the left side we find that the output intensity can be written in terms of the $U(t)$ and $L(t)$ equations:

$$I_{out} = I_{in} e^{U-L} = I_{in} e^g \quad (17)$$

Integrating the equation for β along the z axis of the amplifier we have:

$$\frac{dU}{dt} = -\frac{1}{hv/\sigma_{em}} \int I_{out} [\beta - \alpha] dz \quad (18a)$$

Then substituting in Eqn. 17 we obtain:

$$\frac{dU}{dt} = -\frac{I_{in}}{hv/\sigma_{em}} \int e^{U-L} [\beta - \alpha] dz, \quad (18b)$$

and therefore

$$\frac{dU}{dt} = -\frac{I_{in}}{hv/\sigma_{em}} \int e^g dg \quad (18c)$$

Finally we find:

$$\frac{dU}{dt} = -\frac{I_{in}}{hv/\sigma_{em}}(e^g - 1) \quad (18d)$$

Following a similar procedure for the α equation we find:

$$\frac{dL}{dt} = \frac{I_{in}K}{hv/\sigma_{em}}(e^g - 1) - \frac{L}{\tau_{11/2}} \quad (19)$$

The problem now reduces to solving the following set of coupled differential equations:

$$\frac{dU}{dt} = -\frac{I_{in}(e^{(U-L)} - 1)}{hv/\sigma_{em}} \quad (20)$$

$$\frac{dL}{dt} = \frac{I_{in}K(e^{(U-L)} - 1)}{hv/\sigma_{em}} - \frac{L}{\tau_{11/2}} \quad (21)$$

$$\frac{dF_{out}}{dt} = I_{out} = I_{in} e^{U-L} \quad (22)$$

where the known initial conditions $U(0)$, $L(0)$, and $I_{in}(t)$ are used to integrate the equations (20-22) forward in time. Finally the integrated output intensity yields the output fluence:

$$F_{out}(\text{numerical}) = \int_0^{\infty} I_{out}(t) dt = \int_0^{\infty} I_{in}(t) e^{U-L} dt \quad (23)$$

Where $F_{out}(\text{numerical})$ is the exact solution to the lossless coupled rate and energy transport equations which include the terminal level lifetime ($\tau_{11/2}$).

6.4 Formulation of empirical model

The goal of this section is to derive an empirical solution for the output fluence having the form:

$$F_{out}(\text{empirical}) = F'_{sat} \ln[1 + G_o(\exp(F_{in}/F'_{sat}) - 1)] \quad (24)$$

which closely approximates the exact numerical solution described above. To do this we define a modified saturation fluence as follows:

$$F'_{\text{sat}} = \frac{hv/\sigma_{\text{em}}}{\left[1 + \frac{g_2}{g_1} \cdot B(R)\right]} \quad (25)$$

In other words, the problem reduces to determining the appropriate form of $B(R)$. The numerical solutions of Eqn. 23 for square pulses with $R = 0.01, 2,$ and 100 are plotted in **Figure 6.2**. For each numerical solution shown, a best fit of the empirical solution (Eqn. 24) was found by adjusting the value of $B(R)$ to minimize the χ^2 fitting error. The empirical solutions are also shown in **Figure 6.2** along with the corresponding $B(R)$ and χ^2 values where we define:

$$\chi^2 = \sqrt{\sum_{i=1}^{N=100} \left[F_{\text{out}}^{\text{num}}(i) - F_{\text{out}}^{\text{emp}}(i) \right]^2 \frac{1}{N-1}} \quad (26)$$

In **Figure 6.2**, only three different values of $B(R)$ were determined. In order to find a functional form for $B(R)$ additional values were needed. In **Figure 6.3**, over 1000 fits are shown to produce a nearly continuous curve for $B(R)$. As required, $B(R)$ converges to the asymptotes of 1 and 0 for $\tau_p/\tau_{11/2} \ll 1$ and $\tau_p/\tau_{11/2} \gg 1$, respectively, as required by Eqns. 11a and b.

We found that three exponentials (**Figures 6.4 a and b**) are needed to accurately describe the $B(R)$ curve. The exponential sum is written as:

$$B(R) = a_1 \exp(-R/b_1) + a_2 \exp(-R/b_2) + a_3 \exp(-R/b_3) \quad (27)$$

where the coefficients are:

$$a_1 = 0.59735, a_2 = 0.34025, \text{ and } a_3 = 0.0605 \quad (28a)$$

$$b_1 = 1.29348, b_2 = 4.14937, \text{ and } b_3 = 30.38384 \quad (28b)$$

To match the experimental data³ the above equation for $B(R)$ was evaluated for the following input parameter values:

$$g_2/g_1 = 0.35, \quad (29a)$$

$$G_0 = 6.9, \quad (29b)$$

$$I_{\text{in}}(t) = I_0 \exp(-t/w)^{30} \quad (29c)$$

where $I_{in}(t)$ is a square pulse approximated by a super-Gaussian of power 30. In addition, the range of input fluences over which the fits to the numerical solution were made were less than three and a half times the four-level saturation fluence or:

$$F_{in}/(hv/\sigma_{em}) < 3.5 \quad (29d)$$

and was selected in order to emphasize the range of input fluences commonly used in actual extraction experiments and normal laser operation. If we substitute the above definition for $B(R)$ into the modified saturation fluence, F'_{sat} , we have an empirical expression for the saturation fluence which can be used to calculate the output energy for any ratio of the square pulse length to the terminal level lifetime with an error of less than 1.5%. The expression for F'_{sat} will be used to determine the terminal level lifetime from the Yarema and Milam extraction data (discussed in Section 6.6). Accordingly, our choices for the value of the parameters (g_2/g_1 , G_o , and $I_{in}(t)$) and therefore $B(R)$ are specific to this problem. In the following section we discuss how $B(R)$ and the empirical solution changes when these parameters are varied.

Before proceeding however, we would like to mention that in a recent publication by Beach et al.⁵ an approximate form for the extraction efficiency is derived that includes the ratio of the pulse width to the terminal level lifetime and is shown to be:

$$\eta_{extr} = \frac{1}{1 + \frac{f_1}{f_2} \cdot B(R)'} \quad (30)$$

and

$$B(R)' = \frac{1 - \exp(-R)}{R} \quad (31)$$

where the parameter $B(R)'$ is equivalent to our fitting parameter $B(R)$ and f_1/f_2 are the fractional populations in the lower and upper manifolds, respectively. This form was found by assuming a low probability for re-absorption of the ${}^4I_{11/2}$ population into the ${}^4F_{3/2}$ level. The uncoupled differential equation for N_1 then becomes:

$$\frac{dN_1(t)}{dt} = P - \frac{N_1(t)}{\tau_{11/2}} \quad (32)$$

where the filling rate, P , is approximately equal to the number of neodymium ions brought down to the terminal level from the upper level N_2 in a time τ_p , where τ_p is the square pulse width:

$$P \approx \Delta N_2 / \tau_p \quad (33)$$

The solution for N_1 is:

$$N_{1f} = \Delta N_2 \cdot \left[\frac{1 - \exp(-R)}{R} \right] = \Delta N_2 \cdot B(R)' \quad (34)$$

where we have assumed the initial population, N_{1i} , to be virtually zero. The solution for N_1 (Eqn. 34) is then substituted into the definition of the extraction efficiency to obtain Eqn. 30.

We found that $B(R) = B(R)'$ proved to only be accurate for input fluences which are less than the saturation fluence of the medium ($F_{in} < hv/\sigma_{em}$). We have nonetheless found that an adequate fit to $B(R)$ can be achieved over a larger F_{in} range if a phenomenological parameter is introduced by taking $B(R)'$ to the 1.13 power (i.e. $[B(R)']^{1.13}$). This new form of $B(R)'$ can be substituted into Eqn. 24 and 25 to determine the output energy with an error of less than 1.5% for the input parameters in Eqns. 29a-b.

6.5 Applicability of model to variations in the input parameters (g_2/g_1 , G_0 , and $I_{in}(t)$)

If a different ratio of degeneracies, $K' = g_2'/g_1'$, is required then γ can be redefined as:

$$\gamma = 1 + K' \cdot B(R) \quad (35)$$

where $B(R)$ is still defined by Eqn. 27. We find that the use of a single equation for $B(R)$ for the values of K' in the range of 0.01 to 0.5 will result in an error of less than 2% in the calculation of the output fluence.

The $B(R)$ curves for the gains (G_0) of 2, 6.9 and 20 were calculated. The similarity in the $B(R)$ curves reveals that the modified saturation fluence, F'_{sat} , will only slightly depend on the value of G_0 . The use of a single equation (Eqn. 27) for the values of G_0 in the range of 2 to 20 will result in an error of less than 2% in the calculation of the output fluence.

We investigated the pulse shape dependence of $B(R)$ for four different cases. In **Figure 6.5** the pulse shapes for the Gaussian and 4th, 6th, and 30th power super-Gaussian are plotted. We choose to approximate the shape of a square pulse by the 30th power

super-Gaussian. The equation for $B(R)$ (Eqn. 27) is valid for a square pulse shape with the pulse width defined as: $\tau_p = 2w$. However, when experimental conditions require analysis of a super-Gaussian of a lower power, we found that an alternative definition of the pulse width allows us to use a single definition of $B(R)$ for all super-Gaussian input pulse shapes with powers between 2 and 28. The use of $B(R)$ with the pulse width defined as the full width at 0.24 of the maximum results in less than a 1.5% error in the calculated output fluence. The new pulse width, τ'_p , is defined as:

$$\tau'_p = 2w_{.24} = 2w \cdot 1.55^{(1/p)} \quad (36)$$

and p is the power of the super-Gaussian.

An error of less than 3% in the output fluence calculation will occur if all of the above parameters (g_2/g_1 , G_o , and $I_{in}(t)$) are simultaneously varied. Obviously, if a more accurate fluence solution is required or if temporal details are needed, then the differential equations can be solved exactly. However, our empirical solution is convenient for a reasonable and quick calculation of the performance of a laser material when the terminal level lifetime must be considered.

6.6 Determination of $\tau_{11/2}$ from numerical modeling of gain saturation data

In 1982, a series of experiments were conducted by Yarema and Milam³ to measure the gain and saturation fluence of several neodymium-doped phosphate laser glasses. In particular, these measurements included data for the phosphate glass LG-750. The neodymium energy level diagram for this experiment was previously shown in **Figure 6.1**. The experimental arrangement for measuring the relative energy of the main laser beam entering and exiting a test amplifier is shown in **Figure 6.6a**. Calorimeters were placed in the path of both input and output diagnostic beams. A 5 mm diameter aperture was placed in the center of each diagnostic beam and the spatially averaged fluence was calculated as the ratio of the energy transmitted through the aperture to the area of the aperture. The diagnostic beam fluences were related to the main laser beam fluences through Fresnel coefficients of the bare beam splitters. The source laser provided fluences up to 3 J/cm² for 1 and 20 ns square pulse durations. In **Figure 6.6b** the fluence-out versus fluence-in data points for two different pulse lengths are shown for LG-750.

The numerical solution (shown as the overlaid solid curve) was found by allowing the terminal level lifetime to vary within the modified Frantz-Nodvik solution for energy extraction (Eqn. 24). A least squares fitting routine varied the $\tau_{11/2}$ lifetime until the χ^2 fitting error was minimized. The best fit to the extraction data yielded a lifetime of $\tau_{11/2} = 280$ ps with an uncertainty of ± 100 ps.

The single ion cross section σ_{em} used within the equations of Section 6.3, assumes a homogeneous distribution of sites surrounding the Nd ions. However, it is well known that in glassy materials such as LG-750, the actual site to site differences can lead to hole burning. A rigorous model for describing energy extraction in an inhomogeneous medium like LG-750, might include a line shape function for the emission cross section. However, we have found that a very simple model, one that just assumes two kinds of ion sites exist (with cross sections σ_1 and σ_2), is sufficiently accurate to model the extraction data for LG-750. This model has been discussed in detail in a previous publication and its derivation will not be repeated here⁶. However, we mention that the modified Frantz-Nodvik solution (Eqn. 24) is still used. In brief, the gain medium is partitioned into N slices. The initial pass through the first slice is with the cross section #1 (σ_1) substituted into Eqn. 24. The second pass through the first slice is with cross section #2 (σ_2) substituted into Eqn. 24. The process is repeated for all N slices. The results (discussed in the previous paragraph) of $\tau_{11/2} = 280$ ps were obtained with this method.

6.7 Comparison of $\tau_{11/2}$ values obtained from time resolved experiments

A reproduction of the data taken (open circles) employing the pump-probe experiment previously described in Chapter 2 is shown in **Figure 6.7** for LG-750. The numerical model (solid curve) of the data includes information about the ${}^4I_{13/2} \rightarrow {}^4I_{11/2}$ and ${}^4I_{11/2} \rightarrow {}^4I_{9/2}$ nonradiative transitions. Recall that a lower bound was calculated by correcting the effective lifetime for the 200 cm^{-1} smaller gap in the ${}^4I_{11/2} \rightarrow {}^4I_{9/2}$ transition. The terminal level lifetime evaluated with this assumption was found to be 250 ps with an error of ± 100 ps; a value very close to that derived from the analysis of the energy extraction data in **Figure 6.6b**.

In Chapter 3 we described a time-correlated single photon counting method to measure the nonradiative lifetimes for the ${}^4G_{7/2} \rightarrow {}^4G_{5/2}, {}^2G_{7/2}$ nonradiative transition in LG-750. In **Figure 6.8** we reproduce the 600 nm emission data (open circles) for LG-750 where the kinetic numerical modeling is shown as the overlaid solid curve. Recall from the introduction that the ${}^4G_{7/2} \rightarrow {}^4G_{5/2}, {}^2G_{7/2}$ energy gap is nearly the same as the ${}^4I_{11/2} \rightarrow {}^4I_{9/2}$ gap, and is therefore expected to experience a similar relaxation time^{7,8}. The ${}^4I_{11/2} \rightarrow {}^4I_{9/2}$ nonradiative lifetime inferred from our kinetic analysis is $\tau_{11/2} \equiv \tau_{7/2} = 228 \text{ ps} \pm 50 \text{ ps}$ on the basis of the ${}^4G_{7/2} \rightarrow {}^4G_{5/2}, {}^2G_{7/2}$ relaxation time. In comparing these values with the terminal level lifetime from the gain saturation data it was found that each of the three independent experiments yielded very similar results. The average value of the terminal level lifetime of LG-750 at room temperature is found to be 253 ps with a RMS error of $\pm 50 \text{ ps}$.

6.8 Conclusion

We have modified the definition of the saturation fluence to include the extracting pulse width and the terminal level lifetime. The modified saturation fluence was substituted within the Frantz and Nodvik analytic solution and used to model extraction data previously taken by Yarema and Milam. The use of Eqn. 24 (with the input parameters and restrictions described Eqns. 29 a-d) allows determination of the output fluence to within 1.5% of the exact numerically computed value. Errors of less than 3% are incurred if the input parameters are varied as discussed in Section 6.5.

In addition we have deduced the terminal level lifetime of the neodymium-doped phosphate glass, LG-750, from three independent measurements. The results show remarkable agreement and suggest that the indirect method for determining the terminal level lifetime can be employed with an uncertainty of less than a factor of 2. The average lifetime of LG-750 for all three experiments yields 253 ps with a RMS error of $\pm 50 \text{ ps}$.

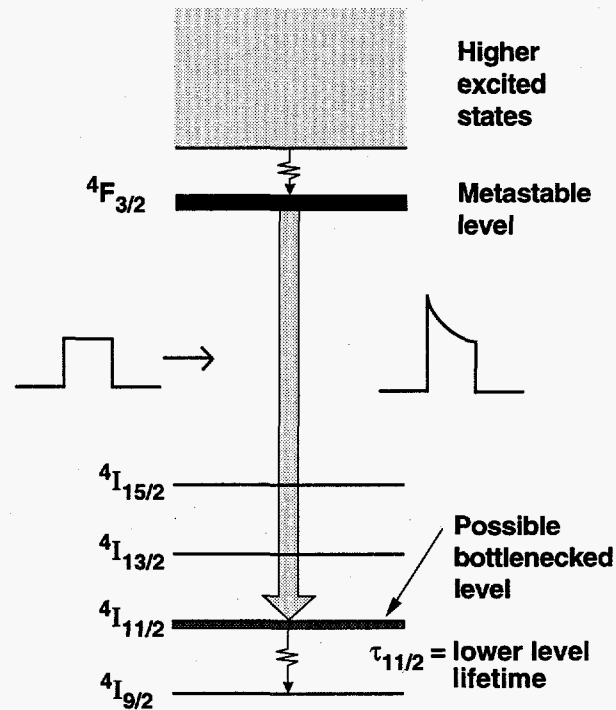


Figure 6.1 Energy level diagram showing the 1 μm transition in Nd-doped phosphate glass where the terminal level lifetime is defined as the time for the neodymium population to decay from the $4I_{11/2}$ state to the $4I_{9/2}$ ground state. When an extracting pulse is passed through an amplifier medium its output can be dependent on the terminal level lifetime. Through numerical modeling of the extracted energy, $\tau_{11/2}$ can be determined.

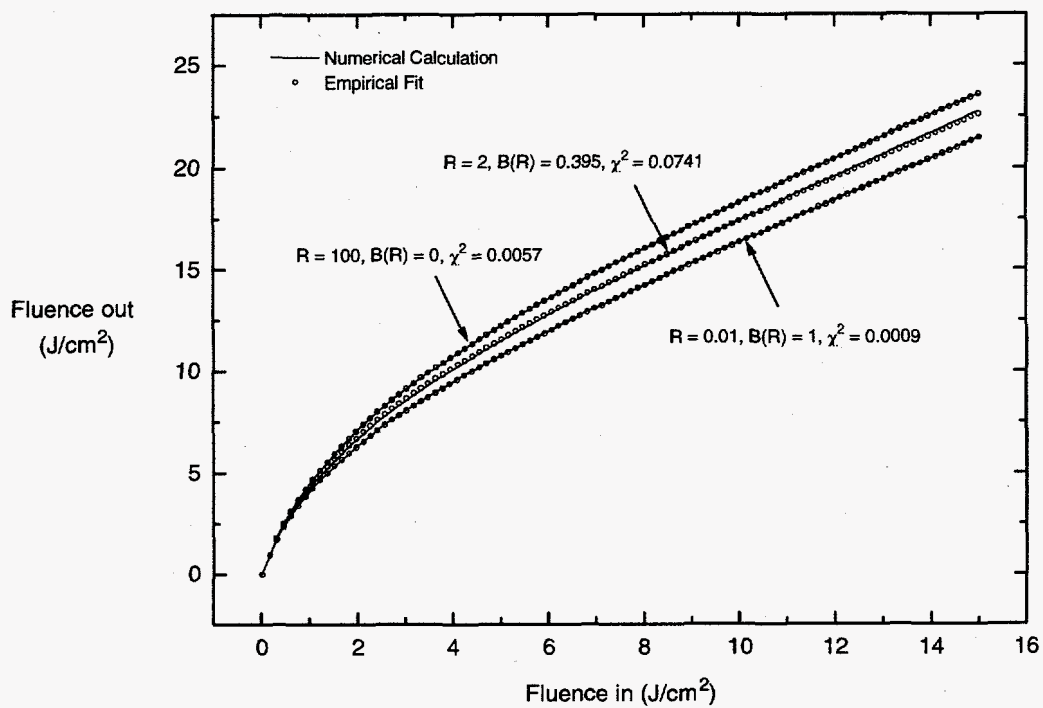


Figure 6.2 In the numerical calculations (solid lines) for the fluence out of an amplifier are shown for three different values of R , where R is defined as the ratio of the extracting pulse width to the terminal level lifetime. The empirical solutions are also shown (open circles) along with the corresponding values of $B(R)$ and χ^2 .

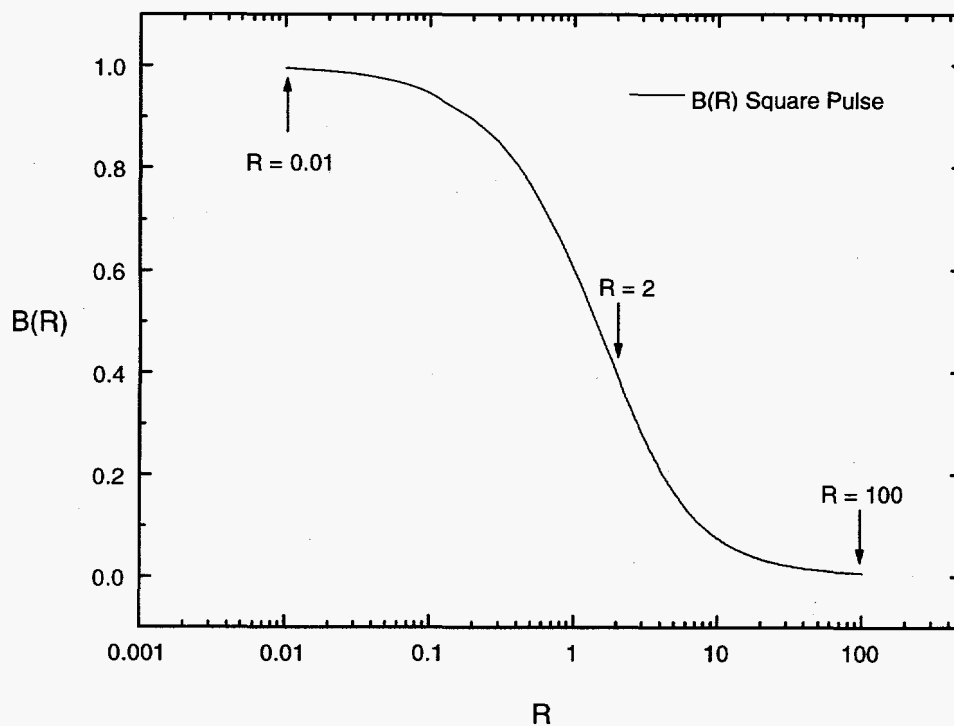
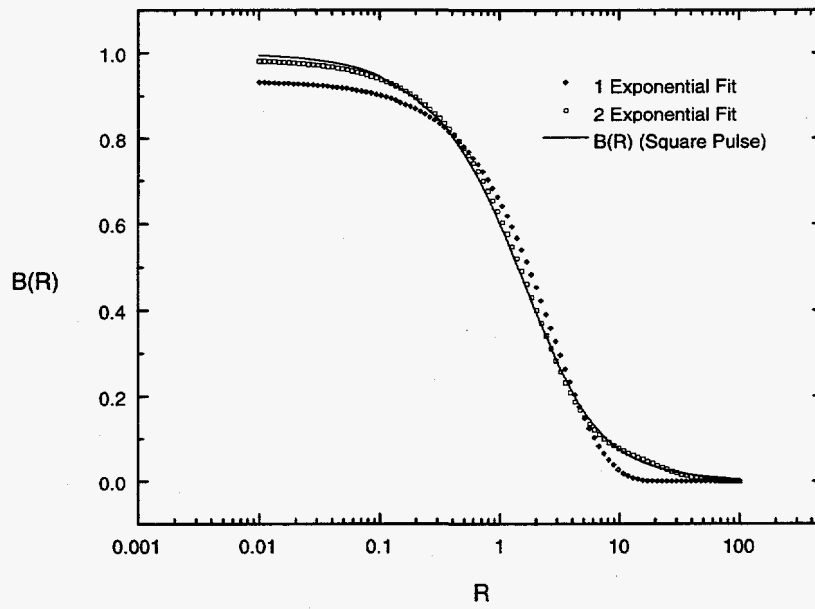
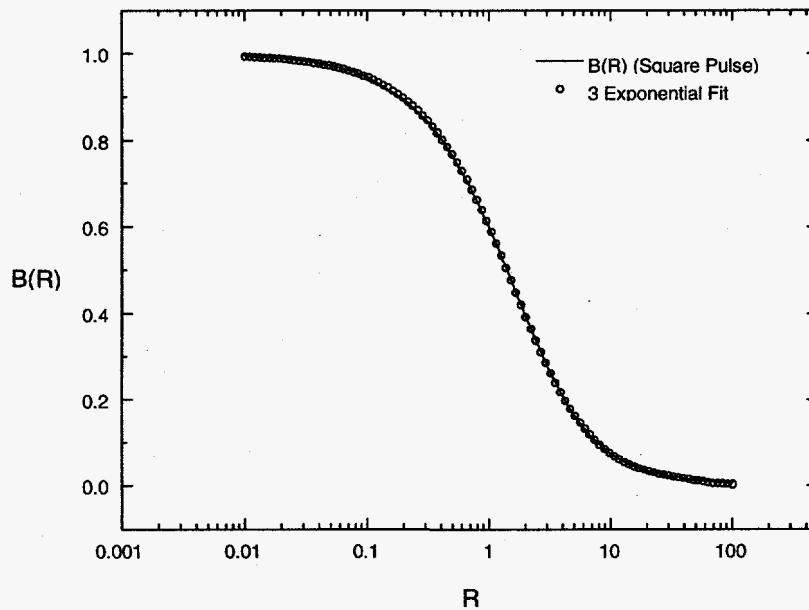


Figure 6.3 Over 1000 best fits of the empirical solution (Eqn. 24) to the exact numerical solution (Eqn. 23) were made in order to form a nearly continuous curve of $B(R)$ values (solid line). The $B(R)$ curve shown is for a square input pulse shape.



(a)



(b)

Figure 6.4 (a) A sum of one and two exponential functions is shown. However, a sum of three exponentials (b) best describes the $B(R)$ curve.

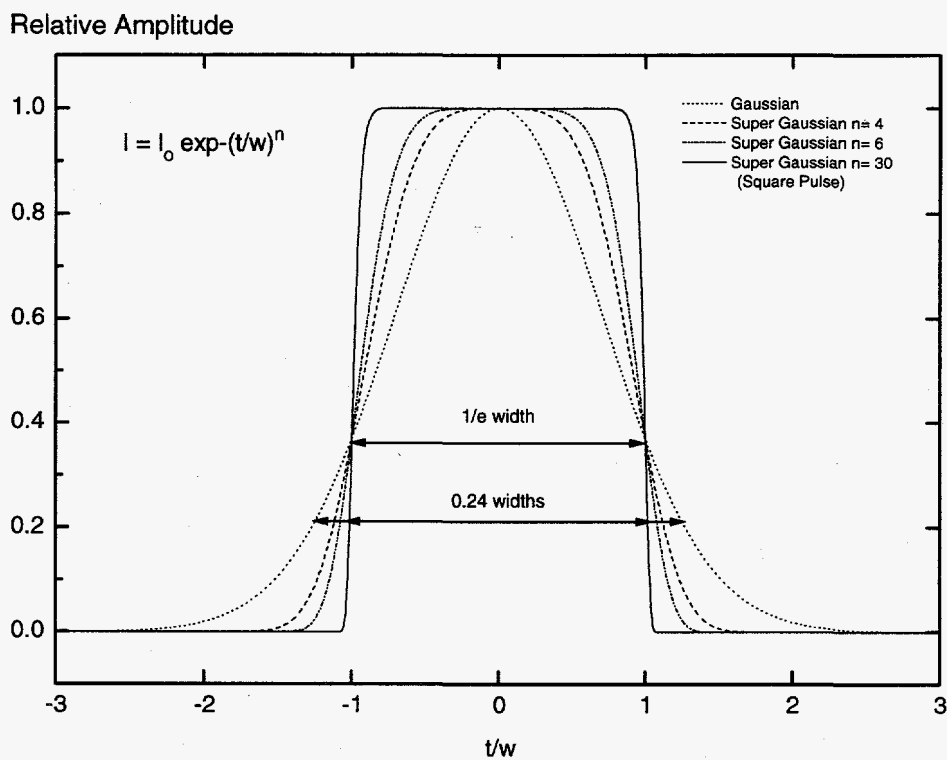
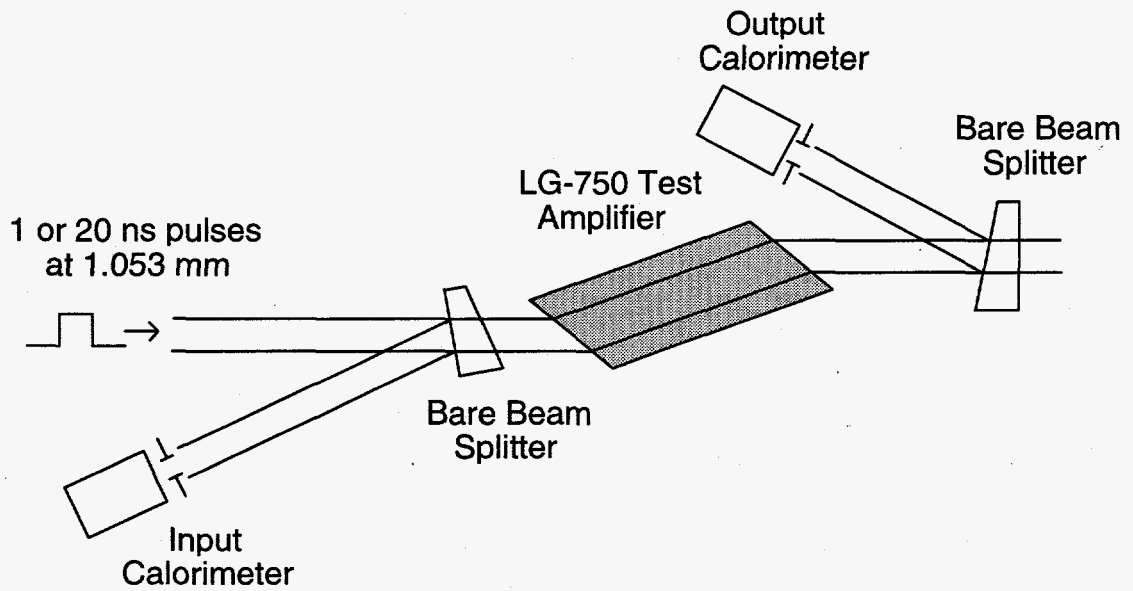
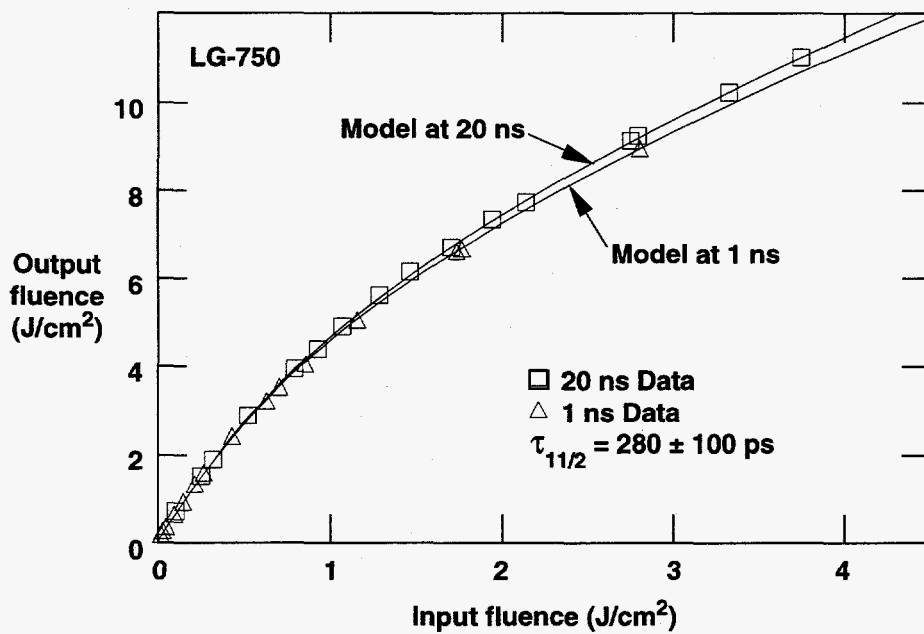


Figure 6.5 Four super-Gaussian input pulse shapes ($n = 2, 4, 6,$ and 30) are plotted. If the pulse width is defined as the full width at 0.24 of the peak amplitude (τ_p'), then a single $B(R)$ curve (corresponding to $n=30$, square pulse) can be used for essentially all Gaussian input pulse shapes.



(a)



(b)

Figure 6.6 (a) the experimental scheme³, and (b) data and model from the energy extraction experiment. Analysis of the data yields $\tau_{11/2} = 280 \text{ ps} \pm 100 \text{ ps}$.

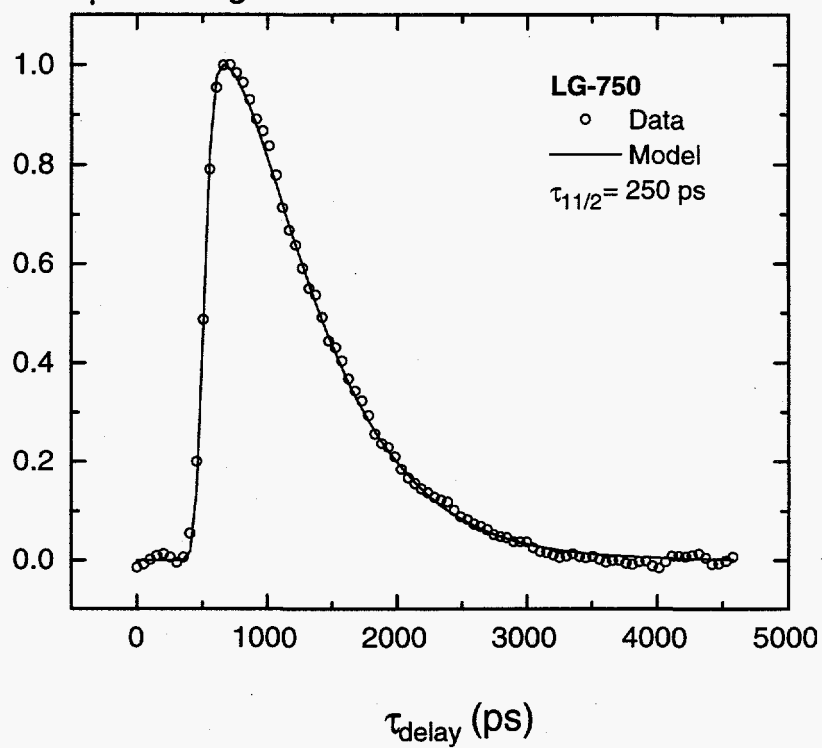
0.88 μm Integrated Emission

Figure 6.7 Analysis of the data from the pump-probe experiment for LG-750 yields $\tau_{1/2} = 250$ ps \pm 100 ps.

Emission at ~600 nm

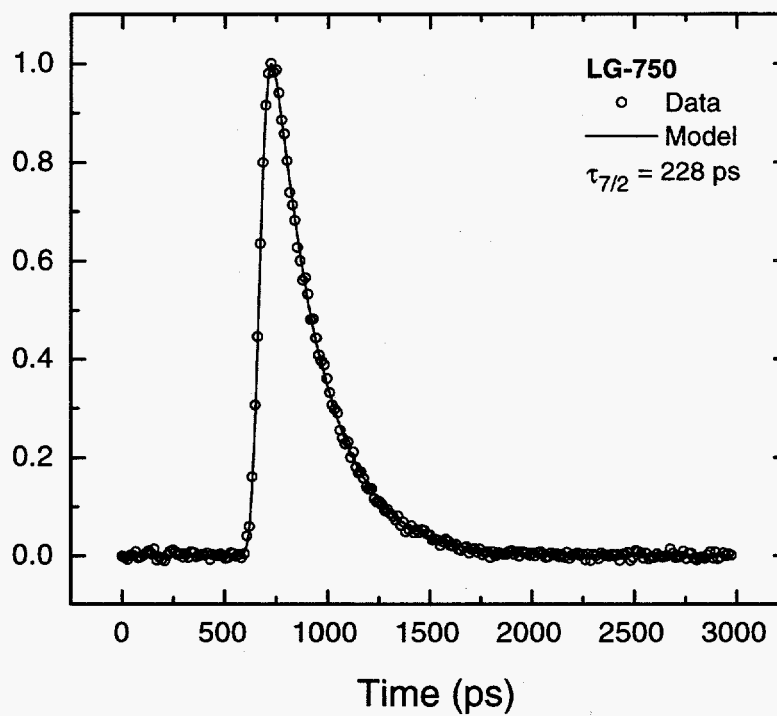


Figure 6.8 Analysis of the data from the photon counting experiment for LG-750 yields $\tau_{11/2} \cong \tau_{7/2} = 228$ ps \pm 50 ps.

Chapter 6 References

- ¹W. F. Krupke, Laser Program, Lawrence Livermore National Laboratory, Livermore, CA 94550 (personal communication, 1994).
- ²L. M. Frantz and J. S. Nodvik, "Theory of pulse propagation in a laser amplifier," *J. Appl. Phys.* **34**, 2346 (1963).
- ³S. M. Yarema and D. Milam, "Gain saturation in phosphate laser glasses," *IEEE J. Quantum Electron.* **QE-18**, 1941 (1982).
- ⁴J. B. Trenholme and E. J. Goodwin, "Numerical modeling of gain recovery," Laser Program Annual Report, Lawrence Livermore National Laboratory, Livermore, CA., Vol. **2**, 236 (1977).
- ⁵R. Beach, P. Reichert, W. Bennett, B. Freitas, S. Mitchell, A. Velsko, J. Davin, and R. Solarz, "Scalable diode-end-pumping technology applied to a 100-mJ Q-switched Nd³⁺:YLF laser oscillator," *Opt. Lett.* **18**, 1326(1993).
- ⁶W. E. Martin, D. Milam, and J. B. Trenholme, "Gain saturation properties of laser materials," Laser Program Annual Report, Lawrence Livermore National Laboratory, Livermore, CA., Vol. **2**, 160(1979).
- ⁷L. A. Riseberg and H. W. Moos, "Multiphonon orbit-lattice relaxation of excited states of rare-earth ions in crystals," *Phys. Rev.* **174**, 429 (1968).
- ⁸C. B. Layne, W. H. Lowdermilk, and M. J. Weber, "Multiphonon relaxation of rare-earth ions in oxide glasses," *Phys. Rev. B* **16**, 10 (1977).

Summary

We have measured the terminal level lifetime ($\tau_{11/2}$) for the 1 μm neodymium transition in several laser media using a novel pump (2.41 μm) and probe (1.06 μm) technique. This method allows us to directly populate the $^4I_{13/2}$ level and subsequently monitor the terminal level $^4I_{11/2}$ population as a function of time by observing the change in integrated fluorescence of the 0.88 μm emission for each time delay between the pump and probe pulses. We developed a computer model to analyze the data and determined the upper and lower limits for the $\tau_{11/2}$ lifetime. The results for some of the materials investigated are: 115-225 ps for Nd:Y₃Al₅O₁₂, 250-450 ps for Nd:LG-750 (phosphate glass), 535-740 ps for Nd:LG-660 (silicate glass), 896-1900 ps for Nd:YAlO₃, and 10.5-20 ns for Nd:LiYF₄. In addition, we found the lifetimes to be independent of the neodymium doping concentration for the phosphate and silicate glasses investigated.

We investigated an alternative experimental method for inferring the value of the terminal lifetime. In this method, we employed a time-correlated photon counting scheme to measure the $\tau_{7/2}$ lifetime for the $^4G_{7/2} \rightarrow ^4G_{5/2}, ^2G_{7/2}$ transition in 30 different Nd-doped glasses and crystals. A comparison of $\tau_{11/2}$ lifetime measured from the direct pump-probe method and the $\tau_{7/2}$ lifetime from the photon-counting method, indicates that the value of the terminal lifetime can be predicted to within a factor of two for most Nd-doped materials. This comparison is useful, since the indirect method provides the simplest technique for determining the $\tau_{11/2}$ lifetime. Recall that the comparisons between the $\tau_{11/2}$ and $\tau_{7/2}$ lifetimes can be made on the basis of the energy gap law which postulates that the nonradiative lifetimes of two different electronic transitions should have the same measured value provided the energy gaps are also similar. These experiments also suggest the validity of the energy gap law, and therefore indicate that the "lower limit" from the pump probe data is likely to be more closely aligned with the actual $^4I_{11/2}$ lifetime.

In addition, we measured the temperature dependence of the $\tau_{7/2}$ lifetime of two glasses: LG-750 and LG-812. As expected, we found that for the phosphate glass, LG-750, the $\tau_{7/2}$ lifetime did not significantly change as the temperature was lowered to

18.3 K. This is because order of the process or the number of phonons necessary to bridge the energy gap was close to unity thereby making the nonradiative rate only weakly dependent on the temperature. The fluorophosphate glass however, exhibited an unexpected result when the temperature was lowered to 18.3 K. We found that the lifetime of the decay shortened from >1 ns to 230 ps, a value similar to that of the phosphate glass, LG-750. This observation could indicate that phosphate complexes in LG-812 are primarily responsible for the transfer of energy from the Nd ion to the surrounding host when the temperature is substantially decreased.

The validity of the energy gap law has been tested in several materials for nonradiative transitions with energy gaps that are greater than 1500 cm^{-1} . Using the measured $\tau_{5/2}$ lifetime data from this work, we were able to plot the nonradiative rate as a function of the energy gap for several Nd-doped crystals (YAG, YALO, YLF, YVO_4 , and GGG-GSGG) and three glasses (phosphate, silicate and fluoride). We found that an exponential dependence of the nonradiative rate with the energy gap is still obeyed. Although the energy gap law is a useful expression for predicting nonradiative rates, we have investigated an alternative method based on energy transfer theory that incorporates the measured absorption coefficient of the material. Using this technique we investigated two oxide crystals: YAG, YALO, and a fluoride crystal, YLF, and found that the logarithm of the nonradiative rate followed a nearly linear dependence with the logarithm of the absorption coefficient.

Based on the importance of the terminal level lifetime and its use in many laser physics models, we have formulated an empirical expression for the saturation fluence in neodymium-doped phosphate amplifier glass that explicitly depends upon the ratio of the pulsewidth to the terminal level lifetime. The empirical saturation fluence, when substituted within the Frantz and Nodvik solution for energy extraction, can be used to accurately model the energy extracted from Nd:phosphate glass amplifiers. If the input parameters (gain, upper and lower laser level degeneracies and input pulse shape) are varied within the ranges discussed, then the output energy of an amplifier medium can be calculated with an error of less than 3%. In the second part of the paper, we compare experimental gain saturation data using phosphate laser glass (Schott glass, LG-750) with

our empirical solution and determine the terminal level lifetime from a best fit to the data. We compare this value with the results from two previously discussed independent experiments: a pump-probe measurement and a less direct emission measurement. It was found that all three experiments yielded similar results. The terminal level lifetime of LG-750 at room temperature is found to be 253 ps with a RMS error of ± 50 ps.

Accurate measurements of the terminal level lifetime as well as other nonradiative lifetimes continue to be an interesting topic in many physics articles. In this work, we have attempted to introduce a novel and yet direct experimental approach as well as validate the use of simpler method. New experimental techniques continue to give insight as to whether existing theoretical models for predicting nonradiative relaxations rates are accurate and useful. Studies which provide an increased understanding of the mechanisms involving multiphonon emission are a challenging theoretical topic. Following the work of others, we have shown data which suggests that a correlation may exist between the theories of multiphonon theory and infrared absorption theory. This opens up many possibilities for deducing the nonradiative relaxations rates from host absorption data. Further work in this area is encouraged since experimentally simple techniques which allow for order of magnitude estimates are valuable and useful.